

AlGaN/GaN Characterization and Associated Processing and Packaging Technologies

BY

RYAN R. AHERN

B.S. University of Illinois at Urbana-Champaign, 1998

M.S. University of Illinois at Chicago, 2008

THESIS

Submitted as partial fulfillment of the requirements
for the degree of Doctor of Philosophy in Electrical and Computer Engineering
in the Graduate College of the
University of Illinois at Chicago, 2011

Chicago, Illinois

Defense Committee:

Mitra Dutta, Chair and Advisor

Michael Strosio

Vitali Metlushko

Siddhartha Ghosh

Nachappa Gopalsami, Argonne National Laboratory

This thesis is dedicated to my wife, Gina, who supported me through it all, and my daughter, Rhianna, who has waited her whole life for me to finish.

ACKNOWLEDGEMENTS

There are a number of people that I would like to thank for providing me the support and guidance necessary to complete my studies. I am indebted to my advisor Dr. Mitra Dutta for providing me the numerous opportunities and guidance necessary to complete my studies. I was indeed fortunate to have her as an advisor. I would like to thank Dr. Siddhartha Ghosh for not only being on my committee, but also teaching me a lot about the optoelectronics industry. I thank Dr. Michael Stroschio and Dr. Vitali Metlushko for being on my committee and also helping to shape my education through coursework and discussions. And finally, I thank the administrative personnel of the Electrical Engineering College and the Graduate College, who, through the course of my disjointed graduate career, showed great patience and understanding in my sometimes non-standard progression.

Outside of the university I am especially indebted to Dr. Michael Wraback at the Army Research Lab in MD. He provided me the opportunity to perform much of the research that appears here and, even after leaving, continued to provide me with the necessary samples to continue research. I would also like to thank Dr. Nachappa Gopalami from Argonne National Laboratory for providing me a location to perform new research while I recovered from wounds in Afghanistan. He showed me a whole new area of research and opportunity. Finally, I would like to thank everyone at Videojet Technologies for their support in my graduate studies.

RRA

TABLE OF CONTENTS

<u>CHAPTER</u>		<u>PAGE</u>
I.	Introduction	1
	1.1 III-Nitrides and Processing Technologies	1
	1.2 Organization of Chapters	4
II.	Raman Spectroscopy of the III-Nitrides	6
	2.1 Introduction	6
	2.2 Basic Phonon Properties	7
	2.3 Phonon Momentum and Inelastic Scattering	17
	2.4 General Raman Scattering	21
	2.5 Raman Scattering in the III-Nitrides	30
	2.6 Determination of Bandgap	36
	2.7 Experimental Setup and Results.....	38
	2.7.1 Introduction	38
	2.7.2 Experimental Setup	38
	2.7.3 Experimental Results and Discussion	42
	2.8 Conclusion	58
III.	Inductively Coupled Plasma Etching of the III-Nitrides	59
	3.1 Introduction	59
	3.2 Background	60
	3.3 ICP Etching of III-Nitrides in Detail	65
	3.3.1 Physical Plasma Parameters	65
	3.3.2 Chemical Etching Considerations	69
	3.4 Experimental Procedures	73
	3.4.1 General Procedures	73
	3.4.2 Experimental Results	77
	3.5 Conclusion	93
IV.	Effective Bonding of Laser Diodes to Heatsinks	94
	4.1 Introduction	94
	4.2 Background	95
	4.3 Bonding Dynamics	98
	4.3.1 Au-In Bonding	98
	4.3.2 Au-Sn Bonding	102
	4.4 Experimental Procedures and Results	105
	4.4.1 Introduction	106
	4.4.2 Evaporation and Bonding of In, Sn and Au.....	106
	4.4.3 Experimental Results	110

TABLE OF CONTENTS (Continued)

<u>CHAPTER</u>	<u>PAGE</u>
4.5 Conclusion	124
V. Characterization of the III-Nitrides by Spectroscopic Ellipsometry.....	125
5.1 Introduction	125
5.2 Background	126
5.3 Experimental Setup and Results	134
5.3.1 Introduction	134
5.3.2 Experimental Setup	135
5.3.3 Experimental Results	136
5.4 Conclusion	140
Appendices	141
Appendix A	142
Appendix B	148
Appendix C	157
Cited Literature	169
Vita	177

LIST OF TABLES

<u>TABLE</u>		<u>PAGE</u>
2.1	PORTO'S REPRESENTATION OF ALLOWED INCIDENCE AND POLARIZATION FOR THE OPTIC ACTIVE PHONONS IN WURTZITE CRYSTALS SUCH AS GAN.....	35
2.2	ACCEPTED VALUES OF PHONONS IN III-NITRIDES.....	45
2.3	MEASURED VALUES FOR THE A ₁ (LO) PHONON.....	49
3.1	SETTINGS FOR ETCH RECIPE III-V	75
3.2	SETTINGS FOR ETCH RECIPE III-V MODIFIED TO INCLUDE BCL ₃	85
3.3	SETTINGS FOR ETCH RECIPE III-V RIE 100W	87
3.4	SETTINGS FOR OPTIMIZED ETCH RECIPE	89
4.1	PROPERTIES OF HARD AND SOFT SOLDER ALLOYS...	96
4.2	ELECTRICAL CONDUCTIVITY OF SAMPLE HARD AND SOFT SOLDER	97
4.3	COMMON INVARIANT REACTIONS IN BINARY PHASE SYSTEMS	99
4.4	BOND TESTING RESULTS	114
5.1	EXAMPLES OF MODEL APPLICATIONS FOR SPECIFIC MATERIALS	131

LIST OF FIGURES

<u>FIGURE</u>		<u>PAGE</u>
2.1	Relative longitudinal displacement of atom position.....	8
2.2	Transverse displacement of atom position.....	9
2.3	Dispersion Relationship for phonons in a crystal with a monoatomic basis.....	12
2.4	Dispersion relation for linear diatomic basis showing critical points	14
2.5	Diatomic displacements in a linear array. M1 and M2 are the masses of the different atoms. U and v are the relative displacements for M1 and M2 respectively.....	15
2.6	Example of phonon dispersion curves for Ge	19
2.7	Raman scattering of a photon with either emission (Stokes) or absorption (anti- Stokes) of a phonon	20
2.8	Raman active tensors for scattering in a wurtzite crystal	28
2.9	Raman tensors for the forbidden scattering by polar phonons in wurtzite crystals	29
2.10	Hexagonal unit cells of GaN in the wurtzite $P6_3mc$ configuration. Gallium atoms are represented by white circles and nitrogen atoms are represented by black circles	31
2.11	Schematic representation of the phonon dispersions of the wurtzite crystal as determined by folding of the Brillouin zone. Zinc-blende crystal direction is $[111]$ while wurtzite is $[0001]$	32
2.12	Optical phonon modes of the wurtzite GaN crystal demonstrating the different atomic motions involved in the separate phonon dispersions	34

LIST OF FIGURES (Continued)

<u>FIGURE</u>		<u>PAGE</u>
2.13	Spectra of Various Samples	44
2.14	Raman Spectra of N824 run at 514nm.....	46
2.15	$A_1(\text{LO})$ Phonon wavenumber vs. Al%	48
2.16	Raman Spectra of several unknown materials.....	51
2.17	Raman Spectra of sample N666 showing $E_2\text{H}$ and $A_1(\text{LO})$ phonons	51
2.18	Raman Spectra of AlGa _N layer samples according to Al%	53
2.19	Two mode behavior of $E_2\text{H}$ phonon in AlGa _N	55
2.20	Sample N919 Raman spectra for different wavelengths	57
3.1	General ICP reactor	64
3.2	AlGa _N /Ga _N QW structure on Al ₂ O ₃	76
3.3	Incorrect processing of N325	78
3.4	Second run of material showing offset of mask and material effects	79
3.5	Etch after addition of BCl ₃	87

LIST OF FIGURES (Continued)

<u>FIGURE</u>		<u>PAGE</u>
3.6	Image showing the quality of sidewall from the final etch process	91
3.7	SEM Image showing the uniformity and anisotropic etch of the mesa structures using the optimized etch process	92
3.8	Commercial version of the same device types	92
4.1	Au-In Phase Diagram	100
4.2	AuSn Phase Diagram	104
4.3	SEM Image of Failed Bond on device #10	116
4.4	Change in Quantum Efficiency for Laser Diodes	118
4.5	Decrease in Threshold Current for Laser Diodes	119
4.6	SEM Image of Failed Device #41	120
4.7	Theoretical Increase in Quantum Efficiency by Utilizing New Bonding Process	122
4.8	Theoretical Decrease in Threshold Current	123
5.1	Flowchart for Spectroscopic Ellipsometry	129
5.2	Simple model for determination of $Al_xGa_{1-x}N$ optical constants	132
5.3	More complex model employing interfacial mixing layers	133
5.4	Refractive Index for Varying Al% in AlGa _N from the IR to UV	137

LIST OF FIGURES (Continued)

<u>FIGURE</u>		<u>PAGE</u>
5.5	Plot of Change in Dielectric Constant per percent Al	139
B.1	MSM fingers on top of AlGaIn layer.....	151
B.2	MSM Design	152
B.3	Laser Diode Mask	154
C.1	Heatsink and diode holder for bonding process.....	157

SUMMARY

A study of various characterization and processing technologies required to fabricate Ultra Violet laser diodes was carried out. There are numerous characterization techniques that need to be utilized to determine device parameters. There are also numerous processing steps that need to be optimized in order to effectively implement the design. A sampling of the variety of processing and characterization techniques used in the development of these laser diodes have been chosen in this investigation. We present two studies on the characterization of AlGaN, and related materials, by both Raman Scattering Spectroscopy and Variable Angle Spectroscopic Ellipsometry. These analysis give us data on the percentage of Aluminum in the sample, which is vital to the determination of emission wavelength, and also the refractive indices of the material, which is crucial to the design and modeling of the devices. We also present two studies on processing technologies crucial to the production of laser diodes, Inductively Coupled Plasma Etching and eutectic bonding of laser diodes. Plasma etching is a vital process step as rough, isotropic etching will prevent the devices from functioning. Proper bonding of the laser diode is crucial to the long term operation of optoelectronic devices. As a final note, we present some background material on the design considerations for laser diodes in the appendices.

Raman Scattering Spectroscopy was successfully employed to develop an empirical formula to allow us to determine the percentage of Al present in a sample layer, and to allow us to characterize an unknown material. We developed a simple process to determine the Al% based on both the $A_1(\text{LO})$ phonon and the $E_2\text{H}$ (high) phonon shifts. Successful use of Variable Angle Spectroscopic Ellipsometry allowed us to develop refractive index dispersion relations and to also determine Al%.

SUMMARY (Continued)

Optimization of the Inductively Coupled Plasma etching parameters allowed us to reliably etch the AlGaIn materials resulting in a mesas and vias that were of sufficient surface roughness and anisotropy to properly function as a laser diode. When compared to commercially produced diodes, our process resulted in better sidewall smoothness while maintaining proper anisotropy. Our optimization of the Au-Sn bonding process for laser diodes resulted in an increase in quantum efficiency of the devices by 13% while reducing their threshold current by 8%.

CHAPTER I

INTRODUCTION

1.1 III-Nitrides and Processing Technologies

The group of devices typically referred to as III-V Nitride laser diodes, form a very important class of optoelectronic devices. Their unique composition and associated difficulty in fabrication have limited their utility until recently, but they have a promising future. Since they can operate in the blue to ultraviolet regions of the spectrum they have a host of promising applications. In the defense related applications, such as remote sensing and detection of chemical and biological elements, an ultraviolet laser diode would enable handheld scanning and detection of chemical and biological hazards. The high intensity UV light can be used by municipal water authorities to both purify water and detect chemical and biological contaminants in reservoirs and water treatment plants. Also, of great commercial importance, these devices allow for a much higher data storage density than the older IR and Red diode laser based optical storage solutions. All of these factors combine to make these devices important to the future economic growth and security of the United States.

The III-V Nitride material systems were initially investigated in the 1950's and 60's. At the time, the materials were of poor quality and were not deemed to be very useful as Silicon was fast becoming the material of the future. III-Nitride research was minimal until the late 1980's when the area of crystalline growth was greatly improved through the MOCVD growth technologies and later MBE.

These growth processes allowed for the control at the nanometer scale that was necessary for good quality crystal growth. The advent of MBE further allowed the process control necessary to grow high quality heterointerfaces.

While many groups worked on this material system, most of the work was on material characterization and bulk crystal growth. There were not many device-oriented research activities being performed. Some of the first successful attempts at growing the material were performed by the team of H. Amano and I Akasaki at Nagoya University. They reported good quality films grown using MOVPE as early as 1986 [1]. While the material growth was coming along there still was a lack of practical devices. One of the first people to work on devices in this area was Shuji Nakamura then at Nichia Chemical Industries Ltd. He successfully fabricated and blue green LED using an InGaN/AlGaN double heterostructure in 1994 [1]. Then in 1996 his group was successful in producing the first Blue laser diode. Much work followed this initial success, with development of ternary and quaternary nitrides to address new wavelengths and process problems. However, most of the work was empirical in nature as the research groups lacked the necessary material parameters for device design. For instance, as recently as 2003, the values given for electron mobility in AlGaN vary by as much as 2 orders of magnitude. Much of this is due to the varying growth conditions yielding different polarity materials. (i.e.MOCVD vs. MBE yields Ga or N interfaces.) Many groups have worked on getting these values and today many of the necessary values are available in the published literature [66,74,78]. There still remains the issue that the growth conditions are highly variable and many groups have no choice to re-characterize the material prior to device fabrication. Hopefully, with the advancement of low defect generating growth processes such as lateral epitaxial overgrowth (LEO), we will have defect density below $10^7/\text{cm}^2$ using growth conditions suitable for production environments.

Practical device fabrication requires a whole host of varied characterization and process steps. While optimization and process controls over the growth process will result in material having the expected thicknesses and concentrations, there is still a need for continuous monitoring of not only the material characteristics during growth, but also after every process step to ensure the resultant device will function as planned. Proper processing optimization is also crucial as it answers the question about whether or not the theoretical device can be manufactured when factoring in processing complexity and time. While laboratory based devices are interesting, practical devices are required to advance the technology.

While a number of varied characterization and processing techniques were studied during my time as a graduate student, I choose to present just a sampling of them here. I felt that a presentation of practical techniques directly applicable to both the laboratory and industry would be more useful than an in depth analysis of a specific material characteristic. I would have liked to have performed more material growth activities, however the opportunity didn't present itself. Most likely I will pursue that avenue in my post graduate studies.

1.2 Organization of Chapters

I have presented the chapters in no particular order as each one is a standalone treatment of the topic. I thought it was important that, given the nature of the topics and my intent, one could simply grab the relevant chapter and take it to the lab. Chapter 2 is our Raman Scattering Spectroscopy and it begins with a rather lengthy discussion on the basics of phonons and their associated effects. I thought it was important to go in depth on the topic of phonons since they are of prime importance to the behavior of the III-Nitrides. Older III-V based optoelectronics did not have as much of a discussion or understanding of the contribution from the phonons so it was frequently overlooked in those treatments. I found that covering this topic first helped to lay the groundwork for better understanding of the Raman Scattering effect and its use as both a characterization tool as well as the understanding phonon effects in nitride optoelectronic devices. I then present the experimental results and discussion of the meaning of the spectra, and the practical application of this technique to the user. Chapter 3 is an analysis of the Inductively Coupled Plasma etch process starting again with a background on the techniques for control, the chemical processes and the settings used in a base process, followed by our experimental result and successes in developing our process. Chapter 4 is a discussion on the important process of bonding laser diodes to heatsinks in order to provide long term operation. Not as much time on the background of this topic is spent as it requires a good deal of discussion on the topic of chemical potential energies and other topics not relevant to the engineer processing optoelectronic devices. We do cover the basic metallurgical considerations and the successes achieved in applying that to laser diode bonding. Chapter 5 covers the topic of determination of optical constants using Spectroscopic Ellipsometry. We begin, as in previous chapters, with a discussion of the theory of spectroscopic ellipsometry.

We follow with a presentation of the basic technique and as it applies to different material systems. Then we present our experimental determination of refractive index and how it varies with Al%. And, as a final point, we cover some basic processing steps such as photolithography and sample preparation for the processing in the body of the thesis. We also cover the basic design considerations for laser diodes and the test apparatus we fabricated in our investigations. The treatment of these topics isn't as comprehensive as the chapter material, so they weren't included as a chapter in the main body of the thesis.

CHAPTER II

RAMAN SPECTROSCOPY OF THE III-NITRIDES

2.1 Introduction

Raman spectroscopy has transitioned from its roots as a researcher based technology utilizing sunlight, colored filters and the naked eye to become one of the standard optical characterization techniques used today. In the early days, availability of sources and detectors really limited the utility of this technique and it remained on the fringe of science until the 1960s when double spectrometers and lasers became available. While the introduction of laser sources and spectrometers really helped the technology mature, it wasn't until the introduction of CCD arrays that it became available to everyone. Today, Raman spectroscopy has a number of key attributes that make it important. For instance, it is in principle non-destructive, (As long as the samples you are scanning won't be damaged by the probe beam,) does not require any special sample preparation such as polishing, thinning or mounting, and it is contactless. Furthermore, when a standard Raman setup is used with a laser and a microscope objective, we can achieve a probe spot size on the order of 1 μm . giving us great flexibility when probing micron scale samples. There are a number of choices when selecting excitation sources for Raman Spectroscopy. Generally most Near Infra-Red (NIR), visible and Ultra-Violet (UV) lasers can be used depending on the configuration and the material being analyzed. These selection rules will be addressed later.

Raman Spectroscopy is particularly useful for gathering information on the crystalline properties of materials as well. Some of the features that can be determined from the spectra gathered include bond strengths from the phonon frequency, lattice strain from the phonon

frequency shift, structural disorder from linewidth broadening, [3] and alloy composition. These are just some of the important material properties that we can determine using Raman Spectroscopy. However, before we get into the III-Nitride specific material properties that we typically determine, it would do well to cover the basic physical properties that produce the unique Raman spectra for different materials. We then transition to the physics of Raman scattering and the necessary modifications to analyze the III-Nitride materials we are interested in.

2.2 Basic Phonon Properties

The quantized vibrational particle in semiconductor physics is known as the phonon. These elastic waves resulting from relative displacement of atoms in a crystalline plane behave in many ways just as any other wave phenomenon. In semiconductors, they can have anywhere from a minimal to a significant impact on device performance depending on the crystal we are dealing with. In Raman Spectroscopy, they serve as the primary vehicle for detecting the Raman effect as it relies on an incident photon inelastically scattering off the lattice producing a phonon and radiating a photon at a new frequency in a process known as Stokes shift. But first, we will cover basic phonon physics.

The basic premise of the phonon begins with the idea of displacement from a lattice point. We take as a starting point, a material whose primitive basis consists of two atoms. This will closely approximate the III-Nitride phonon structure. The frequency we are interested in is the change in relative displacement of adjacent atoms.

For a single type of atom in a crystal basis the longitudinal and transverse waves look appear as in Figure 2.1 and figure 2.2. Relative displacements from the steady state position of the atoms are represented by U_s , U_{s+1} and U_{s-1} .

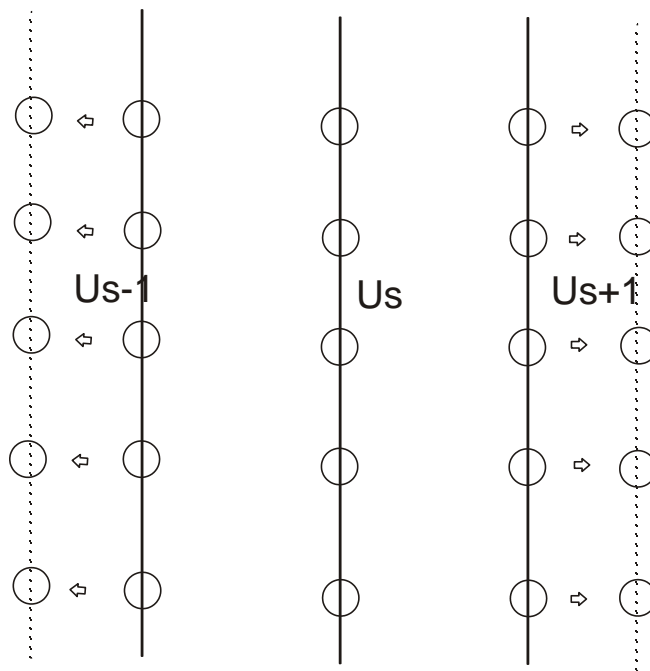


Figure 2.1 Relative longitudinal displacement of atom position.

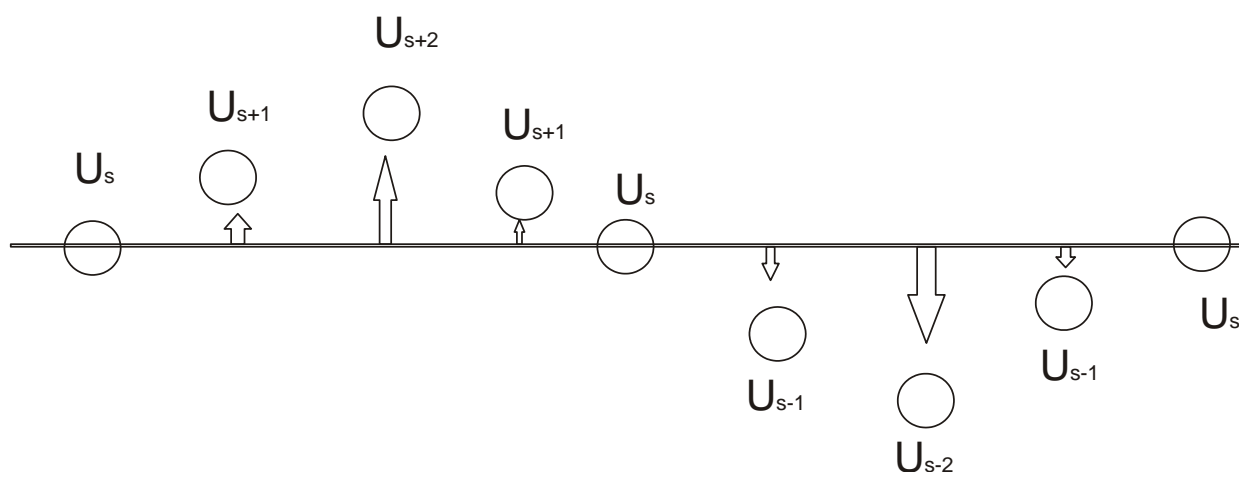


Figure 2.2 Transverse displacement of atom position.

An assumption is made that the force on the crystal planes resulting from the displacement is proportional to the relative displacement ($U_s - U_{s\pm i}$) where $i=1,2,3\dots$

This allows us to represent the force by:

$$F_s = C(U_{s+1} - U_s) + C(U_{s-1} - U_s), \quad (1)$$

This is a representation of linear displacement in the form of Hooke's law [4]. Where C represents the force constant for the atoms of the plane. We then take the equation of motion of the plane of atoms as:

$$M \frac{d^2 u}{dt^2} = C(U_{s+1} + U_{s-1} - 2U_s) \quad (2)$$

Where M is the mass of the atom. If we then assume that we can use the time dependence of $\exp(-i\omega t)$ as for a standard wave, then we can represent the equation of motion as a time dependant relation:

$$-M\omega^2 u_s = C(u_{s+1} + u_{s-1} - 2u_s), \quad (3)$$

Which has solutions of the form:

$$u_{s\pm 1} = u \exp(isKa) \exp(\pm iKa), \quad (4)$$

Where a is the spacing between planes and K is the wavevector [4]. By rearranging the equations and taking $K=\pi/a$ at the boundaries of the first Brillouin zone we end up with the dispersion relationship graphed in Fig 2.3:

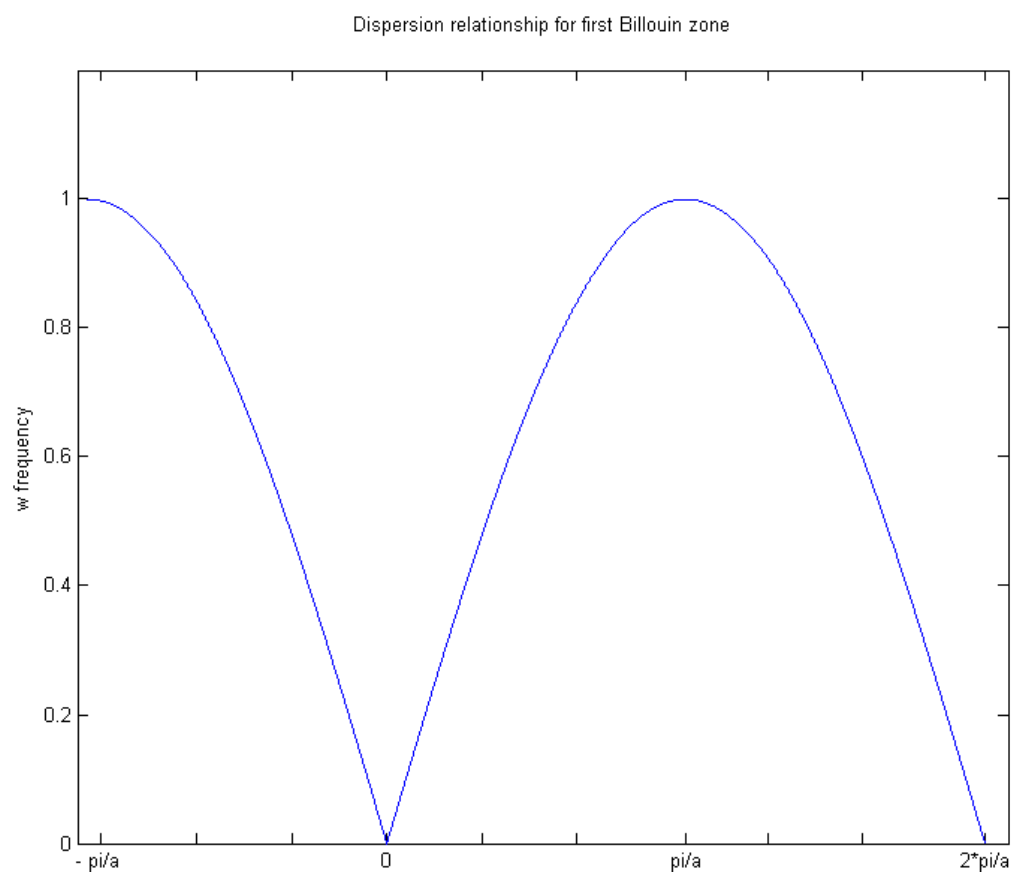


Figure 2.3 Dispersion Relationship for phonons in a crystal with a monoatomic basis.

$$\omega = \left(\frac{4C}{M}\right)^{1/2} \left| \sin \frac{1}{2} a \right|, \quad (5)$$

It can be seen from Fig 2-3 that there is no need to extend the elastic wave definition to a value greater than the first Brillouin zone as the values simply repeat. Additionally, with waves with the dependence of eq. 5 we can see that the values for Ka only have to range from $-\pi$ to $+\pi$ to cover the range of all possible values. Additionally, at the boundaries of the first Brillouin zone the solution for eq.5 does not represent a travelling wave but a standing wave instead. This differs from electromagnetic wave due to a simple reason.

Electromagnetic waves exist and have meaning in between crystal planes and atomic positions. Phonons on the other hand have no physical meaning between crystal planes as they are defined as relative displacement of those waves [5].

Phonon dispersion relations for two dissimilar atoms per primitive basis have a more complex structure. For instance, when dealing with a simple linear lattice where the masses of the atoms alternate, we end up with a separate polarization mode per direction of propagation dependant on which atom we are dealing with. This gives us longitudinal and transverse acoustic and optical branches separated by a forbidden frequency range as seen in Fig 2.4. If we analyze the movements of the individual atoms in a simple linear model such as Fig 2.5 we can see that, if either the masses are different or the force constants between the different atoms are different, then we will have a different equation of motion describing this system. If we make the simplified assumption that each plane only interacts with its immediate neighbor, then we can represent the particle equations of motion as:

$$M_1 \frac{d^2 u_s}{dt^2} = C(v_s + v_{s-1} - 2u_s); \quad (6)$$

And

$$M_2 \frac{d^2 v_s}{dt^2} = C(u_{s+1} + u_s - 2v_s); \quad (7)$$

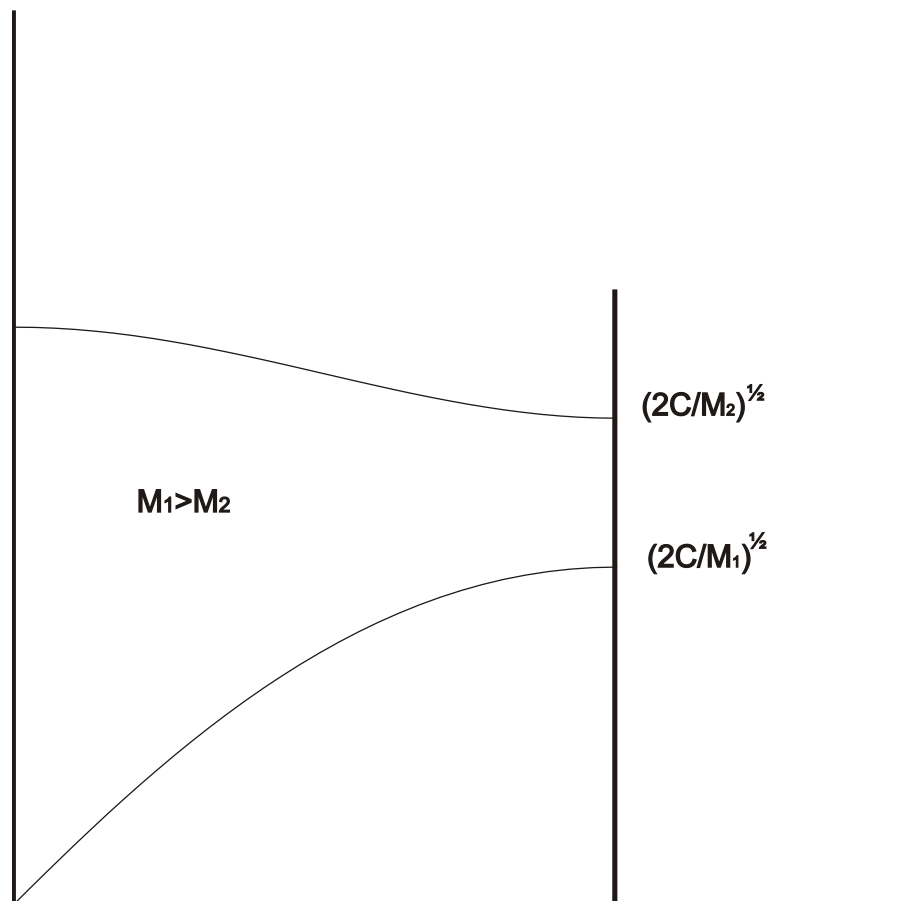


Fig. 2.4 Dispersion relation for linear diatomic basis showing critical points.

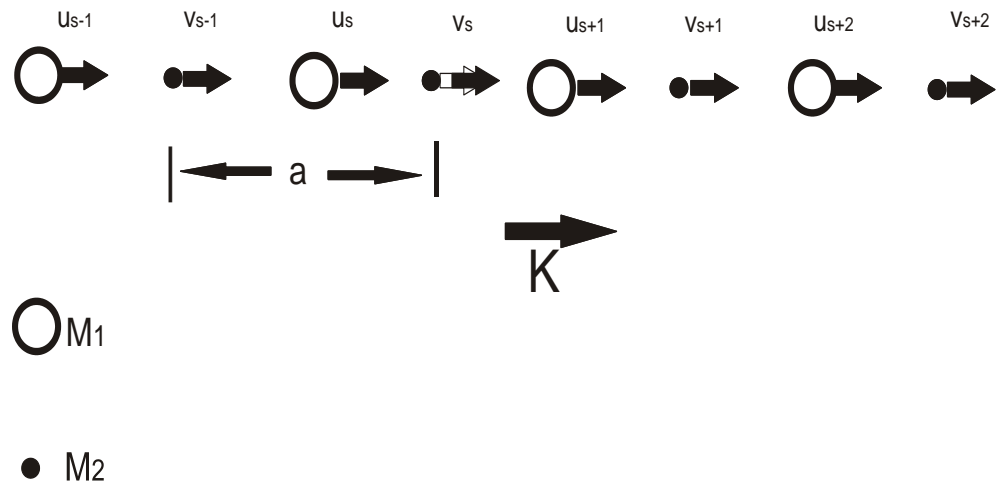


Figure 2.5 Diatomic displacements in a linear array. M_1 and M_2 are the masses of the different atoms. U and v are the relative displacements for M_1 and M_2 respectively.

Which we can get by modifying Eq. 2. We now have to rewrite Eq. 4 to account for two different time dependant solutions to the equations of motion, one for each particle.

Assuming we can get a solution in the form of a travelling wave, with a separate one for each plane, we have Eq. 4 now appearing as:

$$u_s = u \exp(isKa) \exp(-i\omega t); \quad (8)$$

$$v_s = v \exp(isKa) \exp(-i\omega t); \quad (9)$$

Upon substitution into Eq. 6 and Eq. 7 we realize a system of homogeneous equations that can be solved exactly. We however only need to observe the behavior at the boundaries of the first Brillouin zone. Using a common approximation used throughout physics that the displacement is small.. I.e, small Ka, we get solutions along two branches as seen in Fig 2.4. The higher frequency branch will be called the Optical branch, the lower, acoustic branch.

$$\omega^2 \cong 2C \left(\frac{1}{M_1} + \frac{1}{M_2} \right) \quad \text{Optical Branch}; \quad (10)$$

$$\omega^2 \cong \frac{\frac{1}{2}C}{M_1+M_2} K^2 a^2 \quad \text{Acoustic Branch}. \quad (11)$$

These equations have the following solutions at the boundaries of the First Brillouin zone:

$$\omega(K = 0); \quad 0, \left[2C \left(\frac{1}{M_1} + \frac{1}{M_2} \right) \right]^{1/2}; \quad (12)$$

and,

$$\omega(K=\pi/a); \quad \left(\frac{2C^{1/2}}{M_2} \right), \left(\frac{2C^{1/2}}{M_1} \right). \quad (13)$$

Because of the manner in which we define the equations of motion as dependant on the displacement of the adjacent similar planes and not the dissimilar plane, we will have a difference in the relative displacement of the atoms when we use atoms with two dissimilar mass or force constants. On substitution we find the relative displacements for the branches at the $K=0$ wavelength are:

$$\frac{u}{v} = -\frac{M_2}{M_1} \quad \text{Optical Branch;} \quad (14)$$

And

$$u = v \quad \text{Acoustic Branch} \quad (15)$$

Which makes perfect sense when you regard the transverse wave propagates with the successive atoms displacing the opposite direction while the acoustic wave propagates with the displacement in the same direction, albeit with a different magnitude.

2.3 Phonon Momentum and Inelastic Scattering

A final topic in the area of phonon behavior, and one of prime importance, governs the phonon momentum and inelastic scattering from the phonon. In looking at the definition of a phonon as a quantized energy of lattice vibration as defined by relative displacements from steady state positions, we realize that the phonon cannot carry physical momentum in the usual sense. Phonons momentum is sometimes referred to as crystal momentum and is equal to $\hbar K$. If we first examine the wavevector selection rule:

$$\mathbf{k}' = \mathbf{k} + \mathbf{G} \quad (16)$$

Where \mathbf{G} is a random vector in the reciprocal lattice, and the relation is governed by conservation of momentum. In order to represent inelastic scattering we take a look at the wavevector relation when a particle with a random wavevector impinges on a crystal:

$$\mathbf{k} + \mathbf{G} = \mathbf{k}' \pm \mathbf{K}, \quad (17)$$

Which is also represented graphically in Fig 2.7. If we were to take the above relation to determine the energy of the photon created or destroyed we would start with the kinetic energy of the incident particle, $\hbar^2 k^2 / 2M_e$, then measure the energy of the scattered particle, $\hbar^2 k'^2 / 2M_e$, to get the energy of the resultant phonon:

$$\frac{\hbar^2 k'^2}{2M} = \frac{\hbar^2 k^2}{2M} \mp \hbar\omega, \quad (18)$$

Where $\pm\hbar\omega$ is the energy of the phonon that is created (+) or destroyed (-). A good representation of the dispersion curves for Ge appears in Fig 2.6 [6]. This graph represents the information presented in this section.

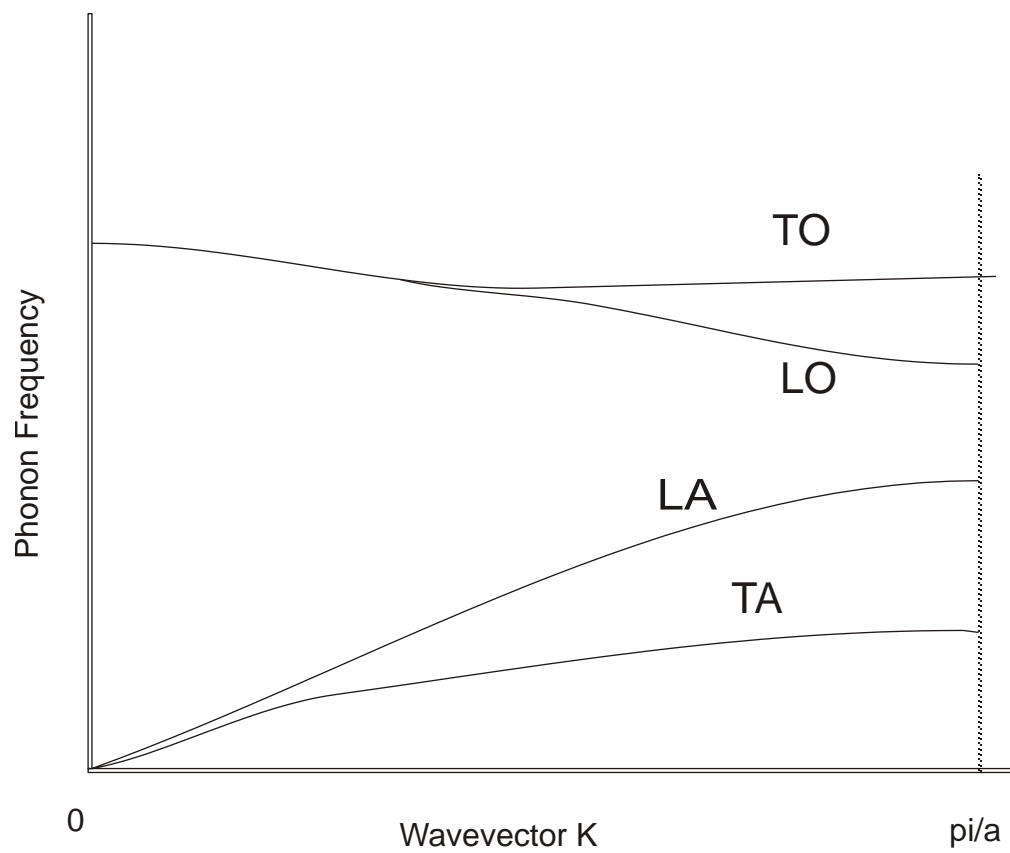
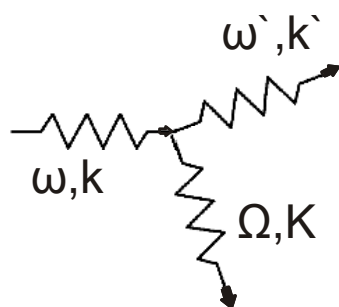
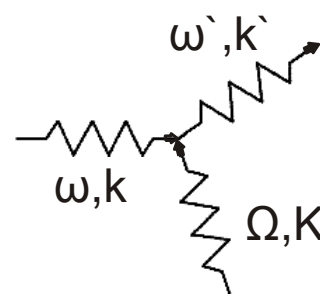


Figure 2.6 Example of phonon dispersion curves for Ge.



Stokes



Anti-Stokes

Figure 2.7 Raman scattering of a photon with either emission (Stokes) or absorption (anti-Stokes) of a phonon.

2.4 Raman Scattering in the III-Nitrides

The process of Raman scattering in its purest form relies on the absorption and emission of a photon with a phonon or magnon either created or destroyed in the process. It is the inelastic process that we can see in Figure 2.7. The selection rules governing the effect are:

$$\omega = \omega' \pm \Omega; \quad (19) \quad \text{and} \quad k = k' \pm K \quad (20)$$

Where ω and k refer to the incident photon, ω' and k' refer to the scattered photon and Ω , K refer to the phonon that is either created or destroyed. It should be noted that this is a first order effect description. It is possible to have a second or higher order effect where you have two and three phonons created. For this level of analysis, you would simply sketch in the additional phonons and account for a new ω' and k' for the inelastically scattered photon. Of prime importance to Raman scattering is the polarizability of the crystal or the production of an electric dipole moment in the crystal. In this case we can examine the electric dipole moment of the atom:

$$\rho = \alpha E_{\text{Local}} \quad (21)$$

Where E_{Local} is the macroscopic E-Field plus the polar phonon contribution. Recall that the time dependant vibrational mode of the lattice can be defined as:

$$u(t) = u_0 \cos \Omega t \quad (22)$$

We are interested in seeing the strain dependence of the polarizability which is $\left(\frac{\partial\alpha}{\partial u}\right)$.

One can expand the strain dependence in a power series for the phonon amplitude u :

$$\alpha = \alpha_0 + \alpha_1 u + \alpha_2 u^2 + \dots \quad (23)$$

If we then express the incident electromagnetic field as:

$$E(t) = E_0 \cos \omega t \quad (24)$$

We then put these into Eq. 21, then use the α_1 term (First order Raman) to get the following:

$$\alpha_1 E_0 u_0 \cos \omega t \cos \Omega t = \frac{1}{2} \alpha_1 E_0 u_0 [\cos(\omega + \Omega)t + \cos(\omega - \Omega)t]; \quad (25)$$

Upon inspection we see that there are two photons that can be emitted in this process. Each process is accompanied by the emission (Stokes) or absorption (Anti-Stokes) of a phonon. Additionally, it is clear that the strain dependence, or polarizability with respect to normal coordinate $\left(\frac{\partial\alpha}{\partial u}\right)$, must not equal zero for the particular vibration to be Raman active.

Classically there should be no difference between the rate at which the Stokes and Anti-Stokes transitions occur. Experimentally we see that the Stokes transition is favored over the anti-stokes transition. The reasons for this can be explained in with quantum mechanical treatment. We start by treating the phonon vibrations as a harmonic oscillator and get the eigenvalue solutions. We can then compare the two intensities of transition based on phonon population by the following for the stokes transition:

$$I(\omega - \Omega) \propto |\langle n_K + 1 | u | n_K \rangle|^2 \propto n_K; \quad (26)$$

Where n_K is the population of the initial phonon mode and n_{K+1} the population in the first order mode. For the anti-Stokes shift the transition intensity varies as:

$$I(\omega - \Omega) \propto |\langle n_K - 1 | u | n_K \rangle|^2 \propto n_K; \quad (27)$$

When we compare the relative intensities we see that:

$$\frac{I(\omega+\Omega)}{I(\omega-\Omega)} = \frac{\langle n_K \rangle}{\langle n_K \rangle + 1} = \exp\left(\frac{-\hbar\Omega}{k_B T}\right); \quad (28)$$

Which will always be less than one. Additionally, this relation shows that the anti-stokes transition rate will trend to zero as the temperature decreases due to the reduction in thermal population of the phonons needed for the transition. This is in good agreement with experimental data by T.R. Hart et al. [7].

On a macroscopic level, we can solve for the phonon vibrations by using Maxwell's equations and solutions for the driven oscillator problem. Loudon developed a model for optical phonons in cubic, biaxial and uniaxial crystals based on these solutions [8]. It is this modulation that results in the macroscopic scattering detected through Raman Spectroscopy. The theory outlined so far provides a solution to the two atom per basis cubic lattice. However, more importantly, it applies to crystals with more than two atoms in the unit cell but still having only one infrared active vibration such as CaF_2 . It does not however cover the uniaxial or biaxial crystal lattice found in many samples of interest. We will cover the model for the uniaxial crystal as the biaxial crystal solution can be gotten from the same process but with an additional degree of freedom.

In Loudon's model, the uniaxial crystal has two separate dielectric constants in its dielectric tensor. One constant assumes the material is equivalent in the (100) and the (010)

directions and differs only in the (0001) direction. Loudon had the following dielectric tensor:

$$\varepsilon(\omega) = \begin{pmatrix} \varepsilon_{\perp}(\omega) & 0 & 0 \\ 0 & \varepsilon_{\perp}(\omega) & 0 \\ 0 & 0 & \varepsilon_z(\omega) \end{pmatrix}, \quad (28)$$

With the constants defined as:

$$\varepsilon_{\perp}(\omega) = \varepsilon_{\perp}^{\infty} \frac{\omega^2 - \omega_{\perp L}^2}{\omega^2 - \omega_{\perp}^2}, \quad (29) \quad \varepsilon_z(\omega) = \varepsilon_z^{\infty} \frac{\omega^2 - \omega_{zL}^2}{\omega^2 - \omega_z^2}; \quad (30)$$

where ω_{zL} , ω_z , $\omega_{\perp L}$ and ω_{\perp} are the characteristic frequencies of the $A_1(\text{LO})$, $A_1(\text{TO})$, $E_1(\text{LO})$ and $E_1(\text{TO})$ phonons respectively. The above consideration deals with propagation normal to the c-axis and is for what can be called the ordinary phonon. However, due to the anisotropy present in the uniaxial crystal we have to account for an angular dependence relation for the long wavelength phonons with what are termed the extraordinary phonon. This extraordinary phonon exhibits an angular dispersion on top of the dispersion relations covered so far when there is an angular difference between the wavevector and the c-axis. According to Loudon's work [8], for the case of weak anisotropy, as we change the angle from 0 degrees to 90 degrees, the upper branch of the extraordinary phonons will change from longitudinal to transverse polarization and the lower branch of the extraordinary phonons will change from transverse to longitudinal polarization. For instance, the $A_1(\text{LO})$ phonon will exhibit $E_1(\text{LO})$ phonon behavior as we go from 0 degrees to 90 degrees.

Approximate solutions across the range of angular deviations will have a mix of Quasi-LO and TO behaviors, and for the uniaxial crystals we have:

$$\omega_{TO}^2 = \omega_{E1(TO)}^2 \cos^2 \theta + \omega_{A1(TO)}^2 \sin^2 \theta ; \quad (31)$$

$$\omega_{LO}^2 = \omega_{A1(LO)}^2 \cos^2 \theta + \omega_{E1(LO)}^2 \sin^2 \theta ; \quad (32)$$

Experimentally this has been confirmed for both the LO and TO branches in the III-Nitrides by Bergman et al. [9], and D. Alexson [10].

On the macroscopic level much of the scattering originates from the modulation of the atomic displacements and the associated electric fields both of which have been covered previously. We cannot use the macroscopic approach to sufficiently explain everything. We need to expand upon a microscopic explanation for Raman scattering.

As before with the macroscopic Raman scattering explanation, Raman scattering can only occur for a certain types of symmetry. We build on the discussions previously and examine how we can define the microscopic behavior. We take another look at the steps in the Raman scattering process as pictured in Fig 2.7. First an incident photon is absorbed by the lattice creating a virtual electronic state where an electron hole pair is created. Next an optical phonon is created by the electron-phonon interaction. This phonon creates an electronic virtual state that eventually creates a scattered phonon. As mentioned before, to accurately describe the scattering intensities/ rate we need to employ a quantum mechanical calculation. For the process described we can use the following scattering rate [8]:

$$\frac{1}{\tau} = \frac{2\pi}{\hbar} \sum_{k_s} \left| \sum_{a,b} \frac{\langle n_i-1; n_i+1; 0 | H_I | a \rangle \langle a | H_I | b \rangle \langle b | H_I | n_i, 0; n_o, 0 \rangle}{(\omega_a - \omega_i)(\omega_b - \omega_i)} \right|^2 \times \delta(\omega_i - \omega_o - \omega_s) ; \quad (33)$$

Where $1/\tau$ is the scattering rate, n_i , 0 and n_0 are the numbers of incident photons, scattered photons and optic phonons present in the initial state, a and b are the transient electronic states, $\omega_{i,o,s}$ are the frequency of the incident and scattered photons, and optic phonons. H_I are the matrix elements that account for the electron-phonon interaction and the electron-radiation interaction. There are two matrix elements for the electron-radiation interaction and one for the electron-phonon interaction. And for the electron-radiation interaction portion of H_I we can represent by $H_{eR} = \vec{E} \cdot \vec{x}$ however it is easier to use the vector potential method as the long wavelength field extend throughout the crystal making E field calculations more difficult. This is the vector potential where A is the vector potential and p is the crystal momentum: $H_{eR} = \vec{A} \cdot \vec{p}$.

A final interesting point to note with the above relation is we see that since the overlap integrals are large near electronic transition points we can realize an increased Raman scattering rate if we select appropriate excitation wavelengths. This is referred to as resonant Raman scattering and is a useful tool for detecting weak interactions.

When dealing with first order phonons, or long wavelength phonons, transitions are deemed to be at or near to the $k=0$ point in the Brillouin zone. These phonons correspond generally to different symmetries of vibration of the atoms in the unit cell and are characterized by the representations of the space group of the crystal lattice. This representation is appropriate for the Raman active phonons that are not also infra-red active. A number of authors have developed tables defining both Raman tensors that are allowed by simple deformation scattering, typically referred to as, “allowed,” and the polarization

dependant Fröhlich, or “forbidden,” scattering tensors. We are interested primarily in the wurtzite crystalline structure as this is the most appropriate form for our overall analysis of III-Nitride compounds. This structure includes GaN and related III-Nitrides that we are interested in. As a subset of the hexagonal crystal group, the wurtzite crystal exhibits the C_{6v} crystal point group. Figure 2.8 shows the allowed Raman tensors for the wurtzite structure. Figure 2.9 shows the forbidden tensors for the wurtzite crystal structure [13]. Taking notation from Herzberg [11], and Wilson et al [12], we have irreducible representations A_1 , B_1 , B_2 , E_1 , E_2 , which are followed by a direction or polarization in parenthesis for phonons which are both infra-red and Raman active vibrations.

$$\begin{pmatrix} a & 0 & 0 \\ 0 & a & 0 \\ 0 & 0 & b \end{pmatrix}$$

$A_1(z)$

$$\begin{pmatrix} 0 & 0 & 0 \\ 0 & 0 & c \\ 0 & c & 0 \end{pmatrix}$$

$E_1(y)$

$$\begin{pmatrix} 0 & 0 & -c \\ 0 & 0 & 0 \\ -c & 0 & 0 \end{pmatrix}$$

$E_1(-x)$

$$\begin{pmatrix} 0 & d & 0 \\ d & 0 & 0 \\ 0 & 0 & 0 \end{pmatrix}$$

E_2

$$\begin{pmatrix} d & 0 & 0 \\ 0 & -d & 0 \\ 0 & 0 & 0 \end{pmatrix}$$

E_2

Figure 2.8 Raman active tensors for scattering in a wurtzite crystal

For Phonon wavevector k parallel to the x - y plane

$$\begin{pmatrix} 0 & 0 & e' \\ 0 & 0 & 0 \\ e' & 0 & 0 \end{pmatrix}$$

$A_1(z)$

$$\begin{pmatrix} a' & 0 & 0 \\ 0 & a' & 0 \\ 0 & 0 & b' \end{pmatrix}$$

$E_1(x)$

$$\begin{pmatrix} 0 & d' & 0 \\ d' & 0 & 0 \\ 0 & 0 & 0 \end{pmatrix}$$

$E_1(y)$

For Phonon wavevector k parallel to the z -direction

$$\begin{pmatrix} h' & 0 & 0 \\ 0 & h' & 0 \\ 0 & 0 & g' \end{pmatrix}$$

$A_1(z)$

$$\begin{pmatrix} 0 & 0 & f' \\ 0 & 0 & 0 \\ f' & 0 & 0 \end{pmatrix}$$

$E_1(x)$

$$\begin{pmatrix} 0 & 0 & 0 \\ f' & 0 & g' \\ 0 & g' & 0 \end{pmatrix}$$

$E_1(y)$

Figure 2.9 Raman tensors for the forbidden scattering by polar phonons in wurtzite crystals.

2.5 Raman Scattering in the III-Nitrides

We have shown the basic theory developed to treat Raman scattering from the cubic to the hexagonal crystal lattices. We are however, mainly interested in the AlGaN/GaN crystals as these are the basis for the devices investigated in this thesis. We have already begun the description of the wurtzite crystal structure forbidden and allowed transitions, now we will expand this explanation to cover the transitions specific to the AlGaN/GaN material systems.

AlGaN/ GaN and related III-Nitrides can crystallize in two structurally different manners. They are hexagonal (2H-) in wurtzite, which we have already studied, belonging to the $C_{6v}^4(P6_3mc)$ crystal group, or the cubic in zinc-blende (3C) structure which belongs to the T_d^2 space group. In the case of the GaN crystal, both configurations feature Ga atoms surrounded by different atoms in a tetrahedral structure, however for the wurtzite structure, the primitive basis consists of two GaN pairs of atoms where in the zinc-blende structure has only one pair of atoms. This results in a stacking order difference between the two which leaves us with differing nearest neighbor distances. You can see the configuration of the unit cell for GaN in Figure 2.10. The wurtzite structure therefore has a unit cell length twice that of the zinc-blende which allows us to represent the phonon dispersion curve of the wurtzite crystal of GaN by simply folding the dispersion curve at the midpoint of the first Brillouin zone (A). This maps the phonons at the L point in the cubic lattice into the Γ point of the wurtzite crystal as seen in Figure 2.11.

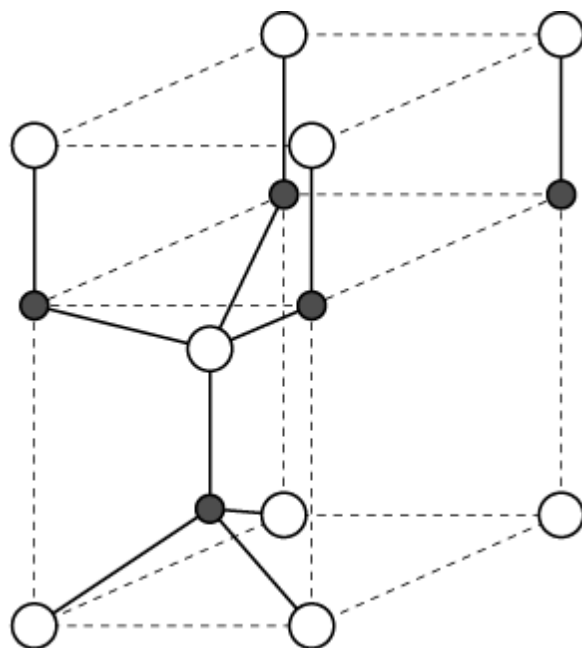


Figure 2.10 Hexagonal unit cells of GaN in the wurtzite $P6_3mc$ configuration. Gallium atoms are represented by white circles and nitrogen atoms are represented by black circles.

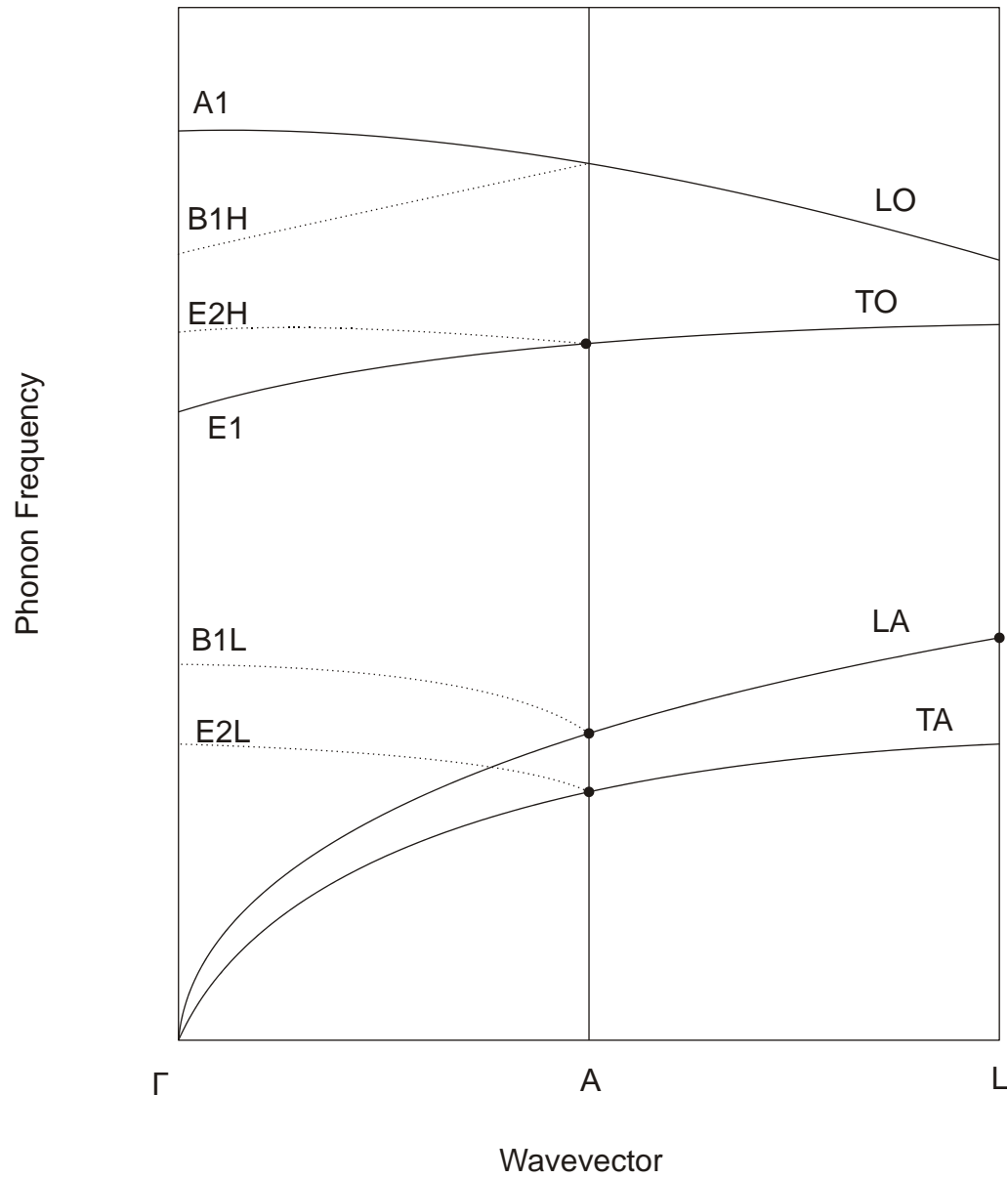


Figure 2.11 Schematic representation of the phonon dispersions of the wurtzite crystal as determined by folding of the Brillouin zone. Zinc-blende crystal direction is [111] while wurtzite is [0001].

From this folding we can see the four zinc-blende phonon dispersion curves turns into eight sets of phonon dispersion curves at the Γ -point ($k=0$) of the wurtzite crystal.

Additionally, due to the macroscopic fields present in wurtzite structures, we have additional splitting on the TO and LO modes splitting into the $A_1(\text{TO})$, $E_2(\text{TO})$, $A_1(\text{LO})$ and $E_1(\text{LO})$ dispersions. Group theory predicts that for the wurtzite crystal structure there will be eight sets of phonon modes at the $k=0$ point of the crystal. They are:

$$\Gamma = 2A_1 + 2E_1 + 2B_1 + 2E_2 . \quad (34)$$

And of these there will be an acoustic A_1 and E_1 and six optic modes, A_1 , E_1 , $2B_1$ and $2E_2$ with a high frequency and low frequency E_2 . The atomic motions involved in these different dispersions are seen in Figure 2.12 [14]. The A_1 and E_1 modes are both Raman and Infra-red active and the E_2 modes are only Raman active. Traditionally the two B_1 modes have been regarded as both Raman and IR inactive (silent) however their values have been determined by using x-ray backscattering [15].

If we inspect the Raman tensors for allowed scattering in Fig. 2.8 and 2.9, we can determine which phonon modes will be detected for various scattering geometries. Table 2-1 shows the scattering configurations for the modes in a wurtzite crystal. We represent the scattering geometries using Porto's notation. In this manner the values outside the parenthesis represent the incident and scattered light directions and the values inside the parenthesis represent the polarization of the incident and scattered light.

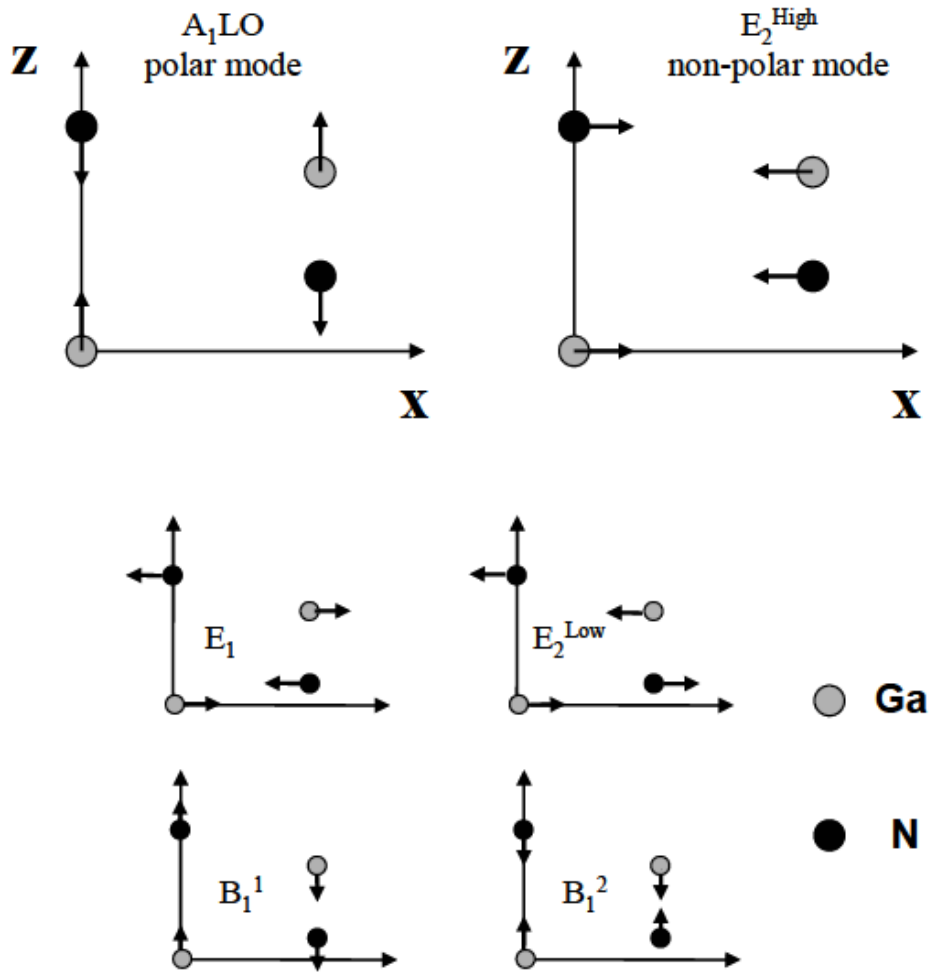


Figure 2.12 Optical phonon modes of the wurtzite GaN crystal demonstrating the different atomic motions involved in the separate phonon dispersions.

Mode		Allowed Configurations		
$A_1(\text{TO})$	$x(y,y)-x$	$x(z,z)-x$		
$A_1(\text{LO})$	$z(x,x)-z$			
$E_1(\text{TO})$	$x(y,z)-x$	$x(y,z)y$		
$E_1(\text{LO})$	$x(y,z)y$			
E_2	$z(y,y)-z$	$z(x,y)-z$	$x(y,y)-x$	$x(y,y)z$

Table 2-1. Porto's representation of allowed incidence and polarization for the optic active phonons in wurtzite crystals such as GaN.

In Porto's notation, all values are read from left to right. The values outside of the parenthesis represent the direction of the incident and scattered light. The values inside the parenthesis represent the polarization of the incident and scattered light respectively. For example, we can see that the $A_1(\text{LO})$ phonon can be scattered by the $z(x,x)$ - z configuration. This represents scattering of an incident beam traveling in the z -direction, also referred to as the c -axis or (0001) direction, polarized in the x -direction. The scattered beam then travels in the $-z$ direction with x -polarization. This representation is a handy tool to use when deciding how to set up the geometry of an experimental measurement of Raman scattering.

From this we can see that there are only a few allowed configurations to pick up specific phonon modes. We are interested in mainly the $A_1(\text{LO})$ and the $E_{2\text{H}}$ modes for our experiments. You can see that both of these can be detected using light incident along the c -axis of the material with polarizations in the x and y directions. We will use unpolarized light to get around the polarization issue.

2.6 Determination of Bandgap

The compositional results from many of the processing steps are reported in a variety of different values. Wavenumber (cm^{-1}), Wavelength (nm), Photon energy (eV), Frequency (Hz), are all numbers that can be used to represent the individual particles and waves we are interested in. Each one makes sense in its respective arena. It does cause a minor issue for us as we need a way to consistently represent the characteristics of the materials we are testing.

The most important value we are looking for is the Al% as this is what we are attempting to determine. Unfortunately, we are typically given the bandgap in eV for the materials since they are determined using PL. We do however have a simple relation that is fairly accurate. From Coli et al. [62], we have a simple relation that has proven to be very useful for determining either the bandgap emission that we can expect from a given percent Al or, by solving the equation for Al%, we can get the Al% for a given bandgap.

Starting with the accepted manner to represent $\text{Al}_x\text{Ga}_{1-x}\text{N}$, where x is the decimal value of Al in the alloy we have the following:

$$E_{g(\text{AlGaN})} = E_{g(\text{GaN})} * (1-x) + E_{g(\text{AlN})} * x - b * (1-x) * x \quad (35)$$

Where $E_{g(\text{AlGaN})}$ is the bandgap for the alloy, $E_{g(\text{GaN})}$ and $E_{g(\text{AlN})}$ are the bandgaps for AlN and GaN respectively, b is a bowing parameter determined by experimentation and x is the decimal value of Al in the AlGaN. These values were determined to be [62]:

$$E_{g(\text{GaN})} = 3.504 \text{ eV}$$

$$E_{g(\text{AlN})} = 6.285 \text{ eV}$$

$$b = 0.6 \text{ eV}$$

Lastly, another useful calculation for switching back and forth between values is the relation between eV and nm which is:

$$\text{Wavelength (nm)} = \frac{1240 \text{ nm}}{1 \text{ eV}} \quad (36)$$

2.7 EXPERIMENTAL SETUP AND RESULTS

2.7.1 INTRODUCTION

Raman Scattering Spectroscopy is a powerful tool for determining a multitude of parameters on nearly any material. We can determine growth parameters such as internal strain [54], grading composition, lattice mismatch, and many others too numerous to list. However we are primarily interested in using Raman Spectroscopy to help us determine the percent composition of the material we are using for devices. Current techniques such as are frequently destructive or complicated and aren't necessarily more accurate than Raman Spectroscopy in terms of determining percentage of Al in AlGaIn. This is the reason we chose to utilize Raman Spectroscopy in our testing. We will begin by describing the experimental setup followed by our results and interpretations.

2.7.2- Experimental Setup

We used two separate Raman setups for our analysis, however, for these results, we will be using the Renishaw inVia Raman microscope at the Center for Nanoscale Materials at Argonne National Laboratory. The Renishaw is a confocal microscope coupled with a full Raman spectrometer. The system uses an external laser source, directed through beam shaping optics, and slits to focus through the microscope objective onto the sample. The Raman scattered photons are then collected by the microscope objective and directed to one of three gratings, 1200lines/mm, 1800 lines/mm or 2400 lines/mm, to deflect them onto the cooled CCD detector. This grating deflects the photons a separate amount for each frequency

and the CCD detects each different wavenumber photon at a different position on the array. The detector reads the intensity of incident radiation for each frequency. In this manner the inVia is able to plot the intensity at each separate wavenumber to give us the Raman spectra. The inVia also features a computer controlled stage and variable microscope objectives so we can automatically map the Raman spectra at a grid of points. The spot size of these points is controlled by changing the objective from 10X-100X which gives the system a possible lateral resolution of under 1 micron. Since it is confocal, the system can restrict the sampling to a very small volume by using apertures and the software. The system uses a common beam path for all of the lasers so the optics and microscope objective need to be changed to the UV compatible ones. Control over the system is done through the WiRE™ software provided by Renishaw and run on the desktop workstation next to the system. The system requires minimal setup and, apart from choosing the proper laser to use and possible optics swap, effectively requires one to place the sample on the holder, bring the material into focus and close the door for operation.

We are fortunate to have a variety of samples available for characterization. Most of the samples were provided by Dr. Michael Wraback's group at the Army Research Laboratory in Adelphi, MD. The samples were primarily fabricated using Plasma Assisted Molecular Beam Epitaxy (PAMBE) [57,58,59], with some of the double and single heterostructure,(DH SH,) devices requiring Molecular Beam Organometallic Vapor Deposition (MOCVD,) and Hydride Vapor Phase Epitaxial,(HVPE,) growth to fabricate the device layers. The various sample characteristics are:

N349D- This is a double heterostructure LED growth consisting of a p-doped AlGaIn layer 25nm thick on top of the DH AlGaIn/GaN QWs on top of another AlGaIn layer

N356D- This is a single heterostructure LED otherwise similar to N349D.

N180- This is a layer of AlGaIn of unknown Al% and thickness on top of a 25nm layer on top of a c-plane Al₂O₃ substrate.

N586- 692nm thick 34% Al PAMBE grown AlGaIn layer on top of a 25nm AlN buffer on a c-plane Al₂O₃ substrate.

N666- 640nm thick 43% Al PAMBE grown AlGaIn layer on top of a 25nm AlN buffer on a c-plane Al₂O₃ substrate.

N822- 640nm thick AlGaIn layer on top of 25nm AlN buffer on a c-plane Al₂O₃ substrate.

The bandedge for this material is measured at 4.6eV.

N824-- 640nm thick AlGaIn layer on top of 25nm AlN buffer on a c-plane Al₂O₃ substrate.

The bandedge for this material is measured at 4.58eV.

N864- Greater than 70% Al AlGaIn layer grown directly on 600μm thick AlN substrate.

N919- 800nm thick NCI-AlGaIn [57] layer on top of 100nm thick AlGaIn barrier on 350nm thick AlN buffer on c-plane Al₂O₃ substrate.

SVT-113- 400nm thick GaN layer on top of AlGaIn/GaN Superlattice on top of GaN. PL shows exciton peak at 3.472 eV

SVT-114- 300nm thick AlGa_N layer of unknown Al% on top of thick Ga_N layer on Si. PL for this sample shows near band edge emission at 3.65 eV.

SVT-115 SVT-116 Possibly Ga_N layer of unknown thickness and composition on unknown substrate.

These Raman scans and subsequent data analysis will not only be able to determine the shift of the E_2 and $A_1(\text{LO})$ phonon peaks for a given Al% in AlGa_N layers but will also enable us to get an estimate for the strain in the material layers and provide evidence for compositional variations in the various layers. This will give a wealth of information that will be vital to device design and processing.

Finally, as Smekal initially showed in the theoretical work on Raman Scattering [60], and Raman experimentally proved, any wavelength light source can induce Raman scattering. However, some wavelengths are far better than others at getting strong signals from a particular sample. We have shown the origin of this effect in Eq. 33 where we saw the reaction rate, and inversely the signal intensity, varies according to the wave function overlaps, incident and scattered photon states and the virtual electronic states. In practice, this effect is noticeable when using various wavelength probe beams. For instance, we found that the 632nm laser, while of sufficient energy to Raman scatter, lacked the signal to noise ratio to provide usable data. Also, from Eq. 33, we can see that different phonons branches will exhibit varying signal intensities according to the probe beam used. If we are able to use a beam close to the resonance peaks of the virtual states for a given phonon branch, we will have greatly increased intensity known as Resonant Raman Spectroscopy.

And finally, if we use a probe beam with a wavelength shorter than the band gap of the material we can realize PL from the sample, this however tends to swamp the Raman signal so it will not work for this analysis.

The Renishaw inVia system can automatically change the laser source used for probing. This allowed us to easily check each sample with a variety of wavelength laser and find the one that showed the best Raman signal. For the most part, this was the 514nm laser, but for some samples the 325nm laser was better. We will cover those results next.

2.7.3 Experimental Results and Discussion

We see the Raman spectra of a variety of our samples pictured in Fig. 2.13. It can be seen that there are a variety of effects we have captured on the various samples. Some related to the varying percentage of Al in the AlGa_N material and some due to structural effects.

It makes the most sense to at this point break out experimental discussion into two separate parts, the first, on the stated goal of successfully determining the Al% in a given AlGa_N layer, and the second on the physical effects we can characterize by reviewing the Raman spectra. To these ends, we will need to segregate the sample data collected into a group of simple AlGa_N layers which will yield the Al% curves, and into the samples with heterostructures and nanoscale features, which will yield data on compositional inhomogeneities, strain, and interfacial effects caused by dimensional confinement and other effects.

If we recall the discussion on wurtzite materials when there are two dissimilar atoms in the primitive basis we can realize either a monotonic or discontinuous increase in the phonon wavenumber as we change the percent of constituent atoms in the crystal. This is directly tied to the polar or non-polar trait of the individual polarizations. For instance, with AlGa_N, as we go from pure GaN to pure AlN the phonons will change from GaN-like to AlN-like for the polar modes and will discontinuously change from GaN values to AlN values for the non-polar phonon modes.. So we can take the values of the AlN and GaN phonons as the limiting factors on the values we should see. Table 2.2 lists phonon wavenumbers [3]:

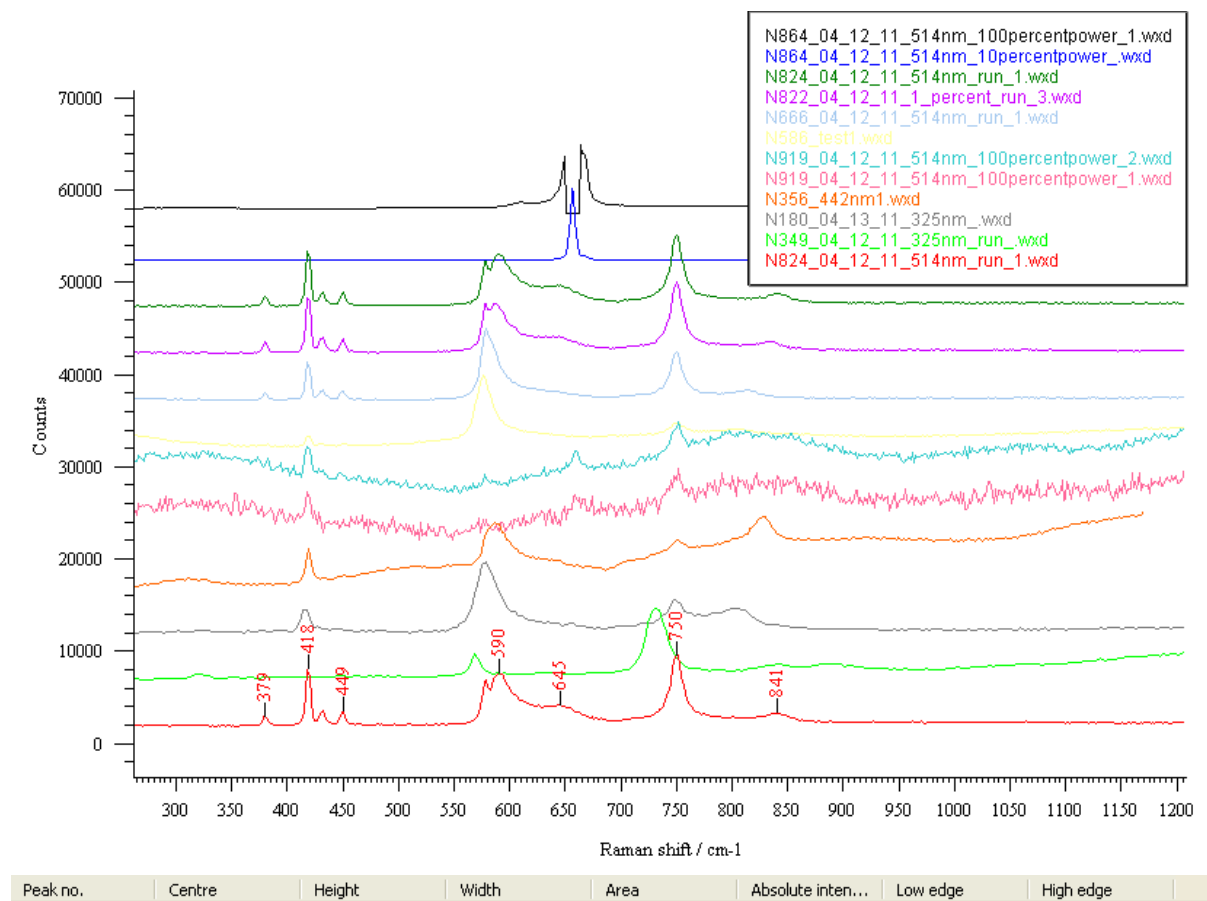


Figure 2.13 Spectra of Various Samples

Phonon	AlN (cm ⁻¹)	GaN (cm ⁻¹)
E ₂ Low	248.6	144.0
A ₁ (TO)	611.0	531.8
E ₁ (TO)	670.8	558.8
E ₂ High	657.4	567.6
A ₁ (LO)	890.0	734.0
E ₁ (LO)	912.0	741.0

Table 2.2: Accepted values of phonons in III-Nitrides.

The configuration we are using is straight backscattering (z(x,x)-z in Porto's notation,) so we should only be able to detect the E₂High and A₁(LO) phonons. Other classically forbidden modes show up in the spectra due to practical physical effect but it is these two that we will use to track the Al% in our materials.

We take a closer look at some of these scans to identify these phonons in the spectra.

For instance, take a closer look at the Raman spectra of N824:

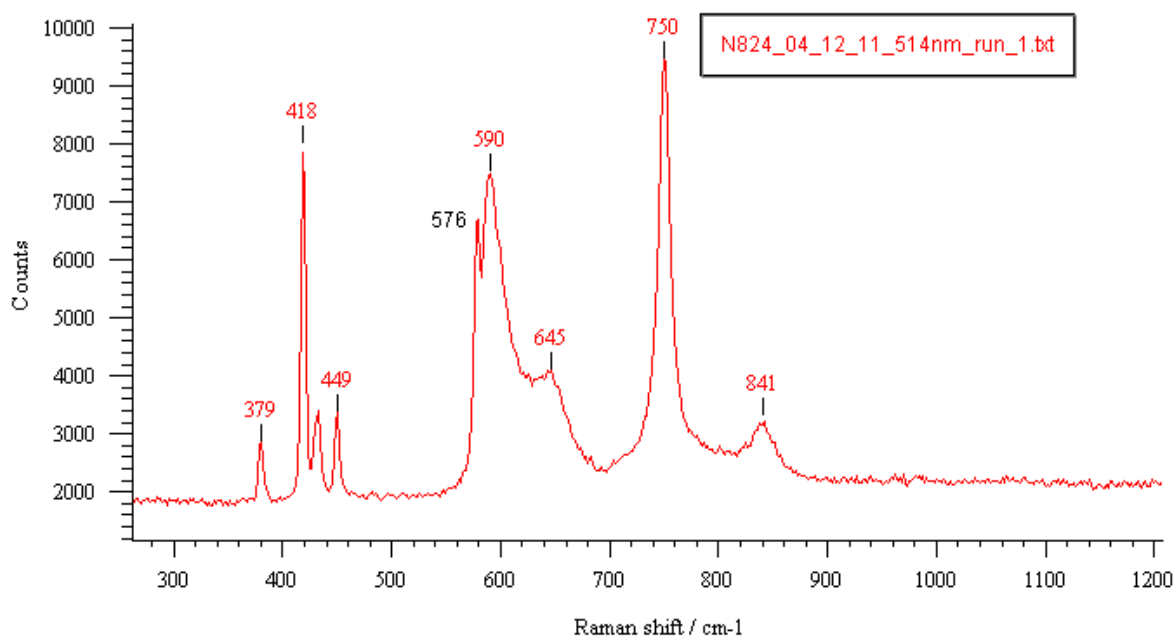


Figure 2.14 Raman Spectra of N824 run at 514nm.

We see most features in this spectrum that are seen in the group of samples we are studying for Al% determination. The peaks from 418-449 cm^{-1} and 750 cm^{-1} are peaks from the Al_2O_3 substrate. This leaves us with important features at 576, 590, 645 and 841 cm^{-1} . We recall that in the backscattering configuration, (z(x,x)-z,) there are only two possible scattering modes visible, the $A_1(\text{LO})$ and $E_{2\text{High}}$ phonons. From our scan there appears to be little doubt that the peak at 841 cm^{-1} is the $A_1(\text{LO})$ phonon. In fact, as was determined by other groups [3,9,10,14,63], the $A_1(\text{LO})$ monotonically increases in wavenumber from the value of GaN at 734.0 cm^{-1} up to the AlN value of 890.0 cm^{-1} . V. Yu. Davydov et al. assigned the following relation to their data:

$$A_1(\text{LO}) = 734 + 153*x - b*x(1-x) \text{ cm}^{-1} \quad (37)$$

Where, as in Eq. 36, x is the decimal value of Al in the AlGaN and b is bowing parameter which equals -75 cm^{-1} . We then compiled a table of the average $A_1(\text{LO})$ phonon wavenumber across all of our AlGaN layer samples and show it in Table 2-3. Upon fitting the data we derived the following relation from the average values of the $A_1(\text{LO})$ phonons:

$$A_1(\text{LO}) = 740 + 154*x - b*x(1-x) \text{ cm}^{-1} \quad (38)$$

With a bowing parameter of -36 cm^{-1} . This is in good agreement with the experimental data from [63] with minor exceptions. Our bowing parameter is lower and, after fitting, our 0% Al and 100% Al points are higher than other groups. We believe that this may have to do with strain shifting the phonons to higher energy points and to a higher free carrier density, but will address that in the succeeding section. We show the plot of Eq. 38 in Figure 2.15.

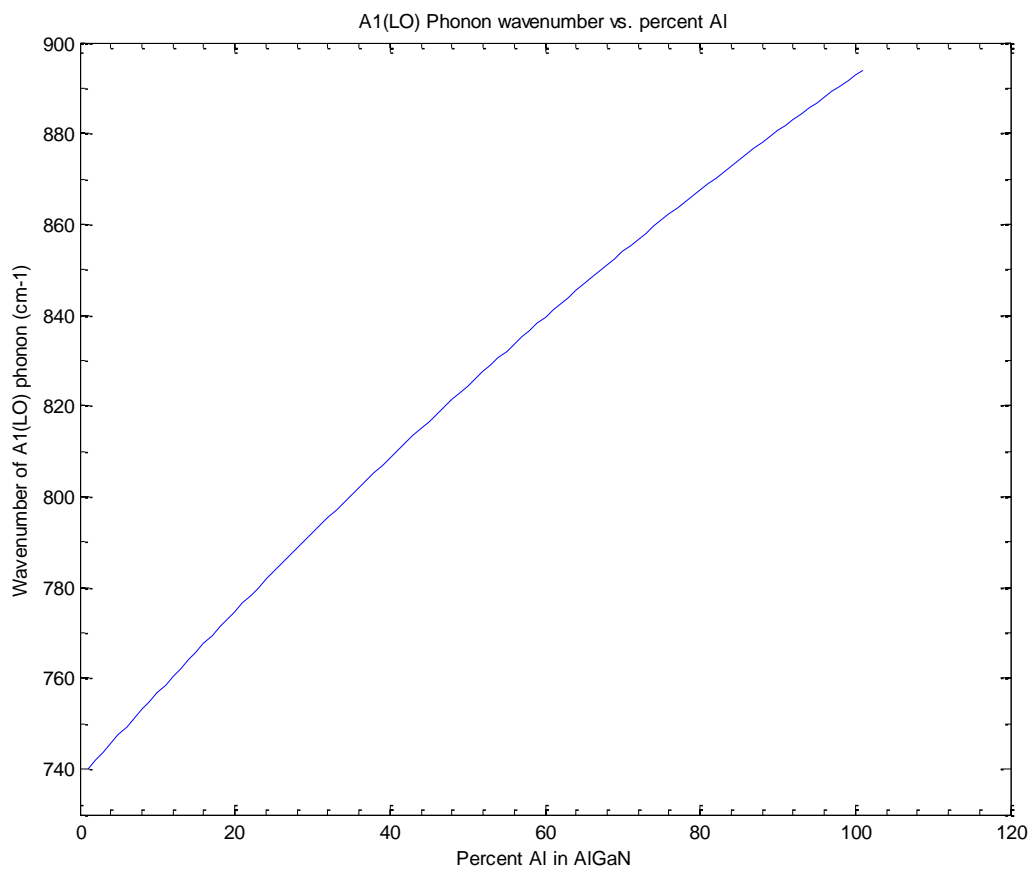


Figure 2.15 A₁(LO) Phonon wavenumber vs. Al%

A1%	A ₁ (LO) Wavenumber (cm ⁻¹)
0	724.0
35	802.0
45	817.5
63	836.0
65	841.0
96	888.0
100	890.0

Table 2.3 Measured values for the A₁(LO) phonon

We now attempt to utilize this method to determine the percent Al in an unknown sample. For instance, in our case we knew only minimal information about the composition of some of the samples we were provided, N180 and SVT114. For N180, all we know is that it is a thick AlGa_N layer on a AlN buffer grown on Al₂O₃. For SVT114 all we know is that it is a layer of AlGa_N of unknown percentage grown on GaN. If we look closer at the Raman spectra for these two samples, N180 in Figure 2.13 and SVT-114 in Figure 2.16 we see that both exhibit the characteristic shift in E₂H phonon peak from the AlGa_N around 575 cm⁻¹ telling us that they both have AlGa_N. Furthermore, they both have the characteristic sapphire peaks at ~416, 447, 750 cm⁻¹ telling us they are grown on Al₂O₃. For sample SVT114, the A₁(LO) phonon is buried in the Al₂O₃ peak. We can only estimate that the sample consists of approximately 4-5% Al. We happen to have PL data that confirms the sample is 5% Al, but even if we didn't, we know about a great deal of the sample composition from this value. Additionally, we will show how we can also use the E₂H phonon to determine percent Al in the following section. Sample N180 has an easily detected A₁(LO) peak that is centered at 805 cm⁻¹. This allows us to use Eq. 38 to determine that the Al% in this sample is 37%. Similar results are easily gotten with nearly any sample we choose. We now move on to an alternate method of scanning which illustrates other capabilities of Raman Spectroscopy, and material specific characteristics of AlGa_N, two mode behavior of the E₂H phonon.

We take a look at the spectrum of sample N666 in Figure 2.17:

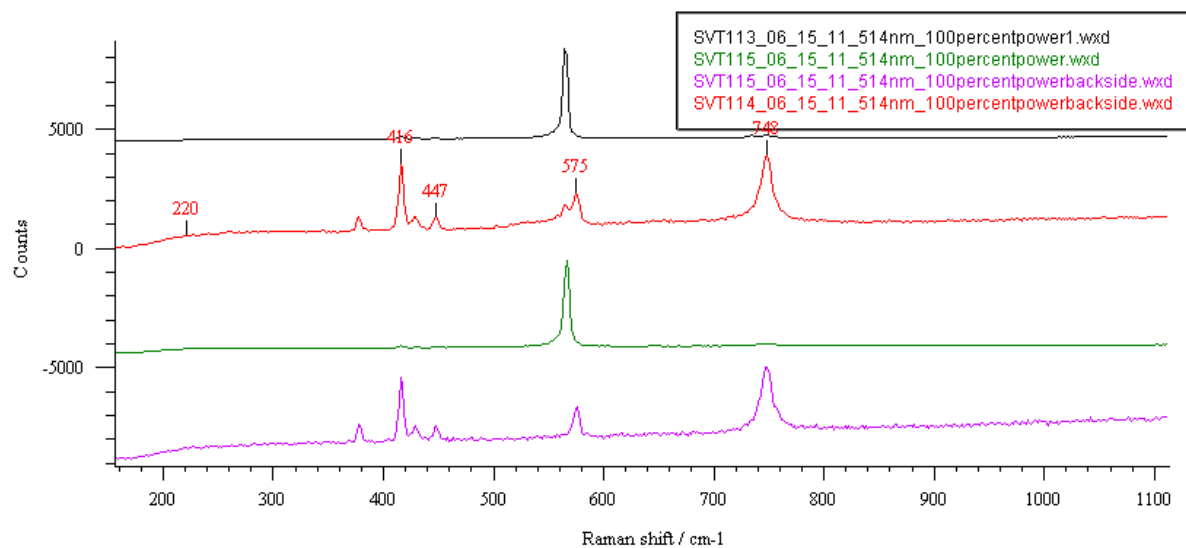


Figure 2.16 Raman Spectra of several unknown materials

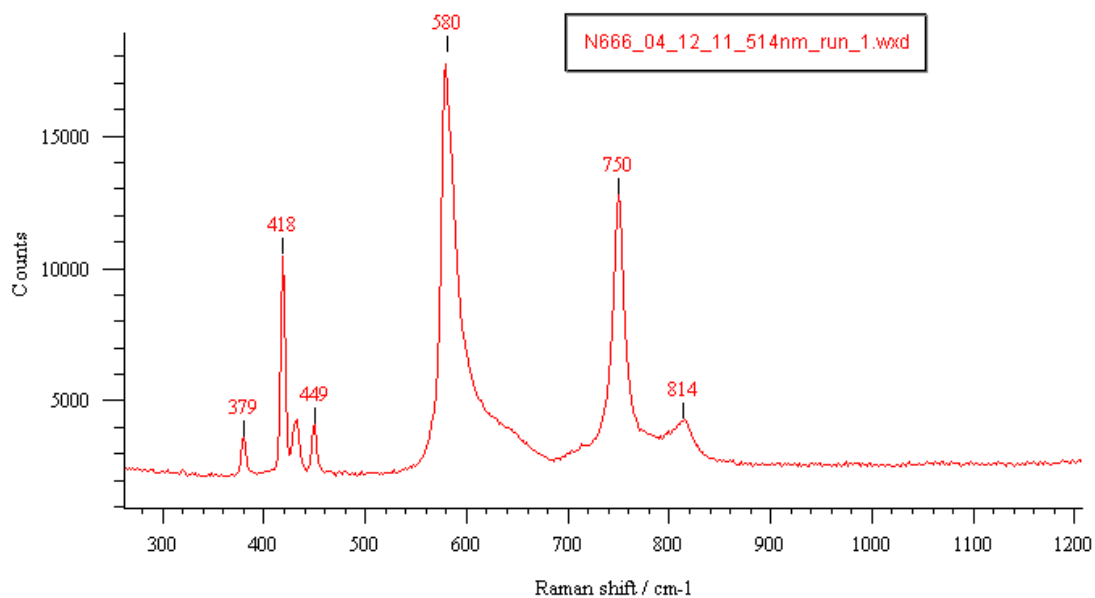


Figure 2.17 Raman Spectra of sample N666 showing E_2H and $A_1(LO)$ phonons.

The values for the E_2H and $A_1(LO)$ phonons, 580 cm^{-1} and 814 cm^{-1} respectively, are clear and, using Eq. 38, we determine that the sample has 42.3% Al. We wish to now develop a second relation for determination of Al%. While the idea is similar to the use of $A_1(LO)$ there are some difficulties. The E_2H phonon is part of the TO branch of the phonon dispersion curve as seen in Figure 2.11. This branch has a degeneracy that should result in two separate phonon dispersion curves in AlGa_N, better known as two mode behavior. Additionally, the $A_1(LO)$ is a longer range phonon which is fairly immune to localized fields but the TO phonons are not. They are highly susceptible to localized field effects and their peak can shift from strain, material quality and free carriers. So, while they can be useful, they will not provide the same accuracy and are more for getting a good sense of the values that are more accurate than when the $A_1(LO)$ phonon is obscured by the Al_2O_3 phonon.

We now plot out the layer samples in order of increasing Al% in figure 2.18. The two mode behavior of the GaN line of the E_2H phonon and the AlN line of the same phonon are marked by trend lines showing the positions of the phonon modes versus percentage. We do notice that, when the Raman Spectra are magnified, that the AlN phonon branch shows up as a shoulder at 640 cm^{-1} in concentrations as low as 10% Al, much lower than other groups have reported [10, 56, 63]. Even more interesting is the fact that it does not shift until we start reaching approximately 50% Al. I believe what we are seeing is the decoupling between the GaN and AlN phonon branches resulting in the two separate spectra. When we plot the peaks of the GaN and AlN branches we get the following:

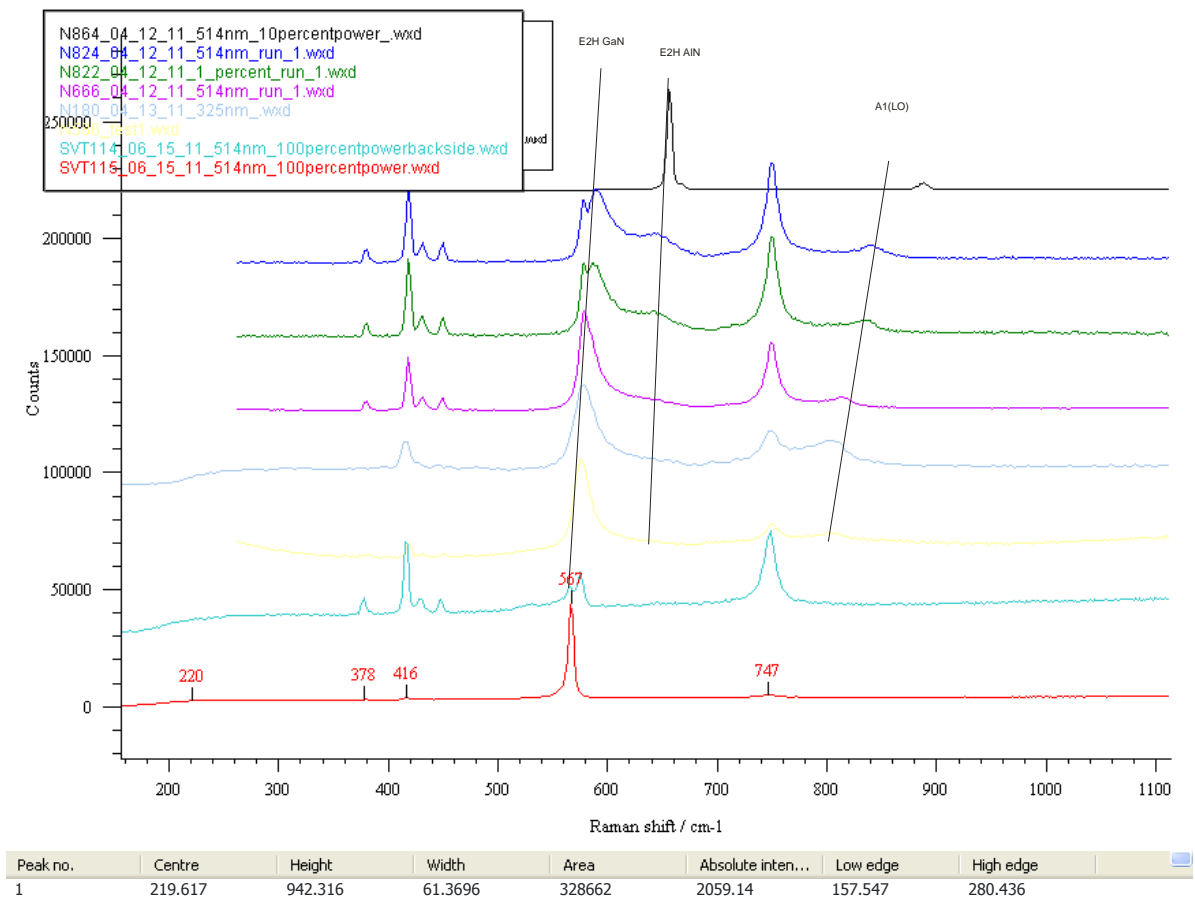


Figure 2.18 Raman Spectra of AlGaIn layer samples according to Al%.

$$\text{Raman Shift GaN branch} = 18x^2 + 21x + 570 \text{ cm}^{-1} \quad (39)$$

And,

$$\text{Raman Shift AlN branch} = 32x^2 - 14x + 640 \text{ cm}^{-1} \quad (40)$$

In figure 2.19 we plot the two lines of the curves. We do show the curves for the entire composition range for the simple reason that we see both lines throughout the compositional range. We have explained the AlN reason for being present, now we examine the GaN line. If one looks again at the spectra of the samples we see that, not only does the GaN line exist across the whole range, but above 60% Al we have a peak to the longer wavelength side of the peak. The persistence of the GaN peak across the range is due to localization effects on the E₂H phonon in GaN. The adjacent peak is actually the E1(TO) phonon coming through due to a small portion of the probe beam coming in at the x(y,z)-x angle.

So, by using Eq. 39 and Eq. 40 we are able to estimate the Al% in an unknown sample of AlGa_{1-x}N_x. A note of caution however, the E₂H phonon does vary according to strain, temperature and pressure so care must be taken to minimize this error in order to use it as a valid characterization technique.

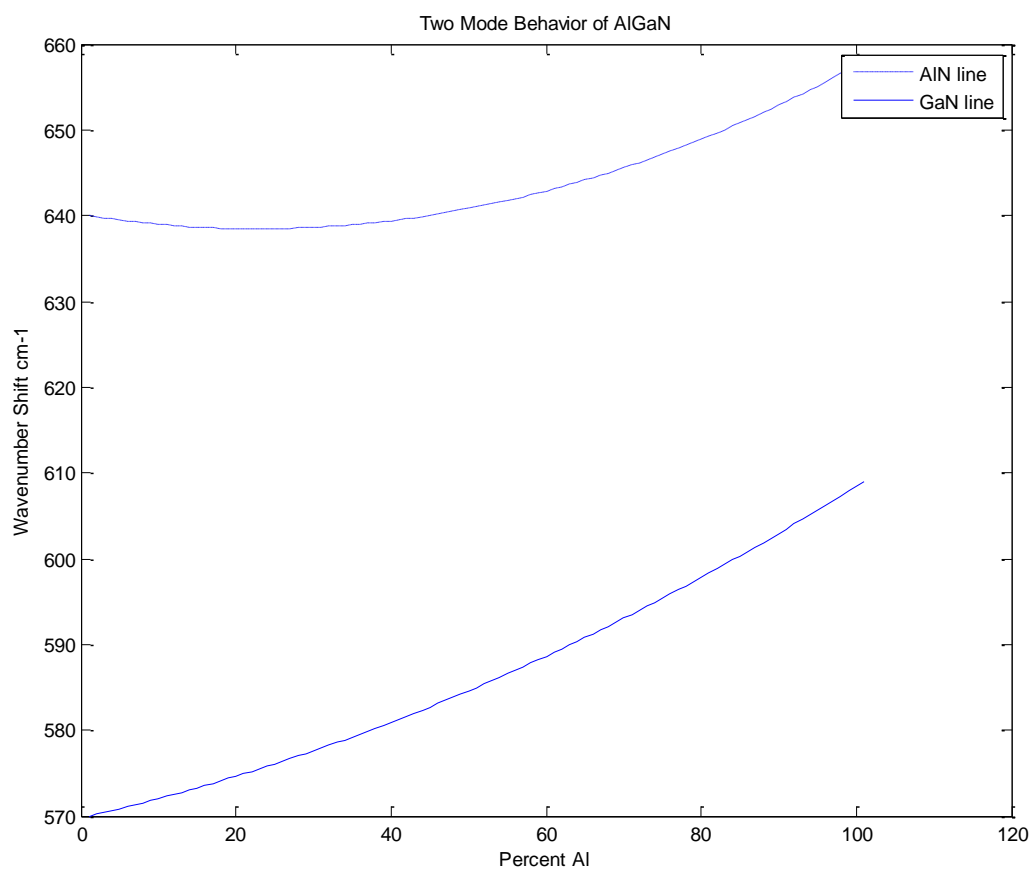


Figure 2.19 Two mode behavior of E_2H phonon in AlGaN.

As a final technique we want to cover the use of Raman Spectroscopy, coupled with multiple laser wavelengths, to characterize a multilayer sample. We know that the probe beam penetrates different depths into the sample depending on the specific absorption of the material in that layer. For instance, 325 nm laser in relatively thin layers for most materials while the 514nm penetrates deeply. GaN also tends to absorb most of the probe beams quickly so we favor backside illumination to determine material characteristics when the GaN layers are on top. We decided to test our theory on one of our known samples to show how it would work. To our knowledge, this technique has not been used to characterize material.

We start with N919, a sample of known layer thicknesses, but unknown Al%. The spectra from the 442nm and the 514nm probe beams pass entirely through the 80nm thick AlGaIn-NCI layer, through the 100nm AlGaIn buffer layer and start to get absorbed in the AlN buffer before going into the Al₂O₃. We see the characteristic peaks for the sapphire substrate telling us what material it is grown on. And, while we can't see the A₁(LO) phonon peak, we do see the characteristic E₂H peak at 657 cm⁻¹ telling us there is a thick AlN layer which is either 100% Al or high Al% AlGaIn under compressive strain, which makes sense as it is grown on Al₂O₃. We now use the 325nm probe beam as it is absorbed effectively by the AlGaIn-NCI layer and the AlGaIn buffer layer. Since this layer is thin, the lattice will not have a chance to relax and strain effects will predominate. This will prevent us from effectively using the E₂H phonon for characterization but we do have the A₁(LO) phonon present at 855 cm⁻¹. If we insert this into the Eq. 38 we get 69% Al. Which, when compared to the PL analysis of the sample, is correct. We can see sample N919 in figure 2.20:

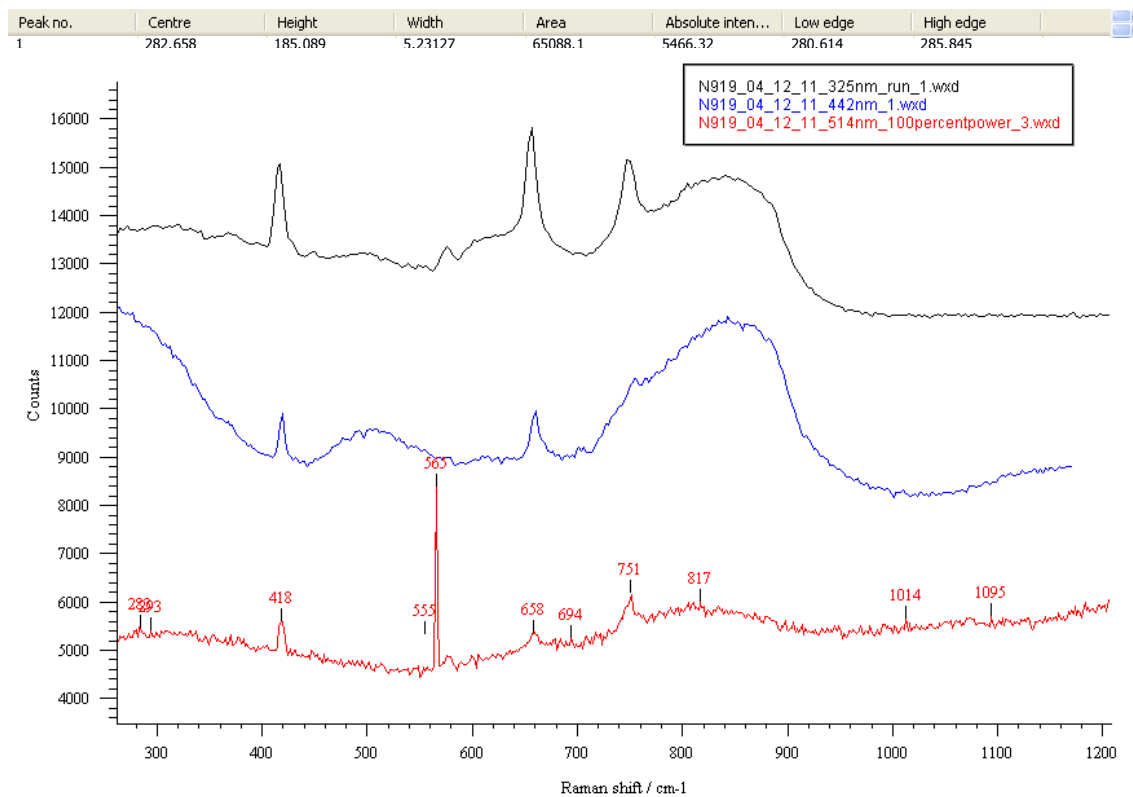


Figure 2.20 Sample N919 Raman spectra for different wavelengths.

We have shown that, through use of varying probe wavelengths, we can get a good sense of the structure of unknown devices. Though the thickness determination is lacking, we are able to determine the buffer layers, the substrate and the active portion of the device through Raman Spectroscopy.

2.8 Conclusion

Through extensive background coverage and practical examples we have shown how Raman Scattering spectroscopy can be used to rapidly and accurately determine material parameters for semiconductor materials. As it is easy to use, real time and applicable to any material it is no wonder that this technique is used by everyone. There are endless uses for this technology in the processing of semiconductor devices that we have not covered such as accurate stress determination, temperature determination, free carrier concentration and doping levels and many others in the biological and chemical sciences. We hope that this has been effective in giving the reader the background necessary to carry out the experimentation to meet their individual needs.

CHAPTER 3

Inductively Coupled Plasma Etching of the III-Nitrides

3.1 Introduction

Basic material properties, substrate selection and growth methods primarily determine the performance of any solid state device however, all devices require proper processing and packaging to realize the benefits of their unique capabilities. Standard photolithographic processing utilizing wet chemical etching has long been the dominant processing technology for the semiconductor industry. It is reliable, robust, technically simple, and has been used to produce many of the devices and processors on the market today. While low cost and excellent selectivity are some of the benefits of wet chemical etching, it does have severe limitations when applied to more sensitive semiconductor devices, especially optoelectronics. Some of the limitations are related to the inherent isotropic nature of the wet chemical etchant which results in poor feature dimension control and undercutting of masks. This wasn't a problem with early devices but as feature control and anisotropic profiles became important, that needed to change. In the 1970s the development of new process technologies to control the physical process of etching brought about Reactive Ion Etching (RIE) and Electron Cyclotron Resonance (ECR) microwave coupled plasmas allowed a far higher high degree of anisotropy than the previous wet chemical etching.[20] The flexibility of these processes was limited however by limitations and through the 1980s groups worked on tailoring not only the physical production of the plasma but also varied the chemical species involved in etching. These groups developed techniques such as ion assisted etching, [21] side wall protection,[22] RF Bias etching,[23] and many others.

All of these led up to the dry etching technologies in use today for the processing of III-Nitrides, RIE, ECR, Magnetron Reactive Ion Etch (MRIE) and Inductively Coupled Plasma (ICP.) While there are benefits to the other technologies such as faster etch rates or better large scale performance, the most important and, subject for this study, is the Inductively Coupled Plasma etching technique.

3.2 Background

The veritable explosion in devices based on the III-Nitrides comes largely from improvements in growth technology. The realization of these materials brought with it a new problem for the device designers. While wet chemical etching was effective on earlier material systems and technologies, it was difficult to implement in the nitride material system due to the natural chemical resistance of these materials. These new devices were increasingly utilizing mesa structures, and other complex architectures, where highly anisotropic features and smooth sidewalls were required to function as the designers intended. Additionally, the superlattice and quantum well structures were being developed that required highly consistent etch rates through many different material compositions. This simply couldn't be done with wet chemical etching. ICP etching is really the perfection of previous techniques so we will cover the basics first, then move to the full explanation of ICP.

Initial development of a dry etching utilized the chemical and physical effects of plasma. This process simply generated ionized plasma using a high voltage plate. This etching process utilized physical sputtering or chemical action or a combination of both.

The general configuration of the electrodes used for generating the plasma led to a moderate anisotropic effect from the ions impacting the surface of the substrate. Additionally, with the introduction of a chemically reactive species in the plasma, you could get a high degree of volatile compound formation on the substrate that would be easier to sputter from the surface. These effects would combine to help provide a process that would yield moderate etch rates with good feature formation. However, there are several drawbacks to this procedure. First, due to the highly inert chemical nature and physical resistance of the nitride materials, you would need high ionization energies to physically sputter material or high chemical concentration to react with the substrate. For instance, the bonding energies of the different materials are as follows [24]:

GaN- 8.92eV/atom

InN- 7.72 eV/atom

AlN- 11.52 eV/atom

From these values one can see the difficulty in chemical etching. One method for increasing the sputtering of the substrate would be to increase the energy of the ions. This would result in extensive damage to the substrate, a problem that increases leakage current and can effectively destroy optoelectronic devices, and reduce the chemical effect by minimizing the time for reactions to occur. One can alternatively increase the chemical concentration by raising the pressure, however that would serve to lower your etch rate to unacceptable levels and reduce the anisotropic ratio of the process. Finally, due to the substrate being mounted to the electrode in this configuration, you have unavoidable inhomogeneity in the plasma field

yielding inconsistent etch rates across the substrate. These factors needed to be addressed with new technologies.

An improvement to the regular plasma etching came in the form of the Reactive Ion Etching process. This was a variation on the standard plasma etch with the addition of driving the substrate with a RF field, (Typically 13.56 MHz.) This technique, as similar techniques before it, utilizes the chemical and physical actions of the plasma to give high etch rates. The substrate to be etched is placed on the powered electrode of the chamber and the ion energies induce a DC bias which accelerates the ions perpendicular to the surface of the substrate. While this is achieved using the earlier techniques, RIE is performed at a much lower chamber pressure increasing the anisotropy of the etch. Additionally, the RF power driving the field gives better etch uniformity across the substrate. While this technique featured improved control over etch rates and anisotropy, there still are difficulties associated especially with the nitrides. In order to etch the nitrides at a reasonable rate for production, either the ion energy needs to be high or the reactant concentration should be high. With high chemical action you reduce the anisotropy, however, with high ion energy you damage the substrate making electrical and optical processes less efficient. As Adesida *et al.* reported when they first etched GaN, with RIE, there was slight overcut to the substrate due to the significant ion energy required to process GaN. [25] But the sidewalls and substrate were relatively smooth with good epitaxial material. While this procedure was good, there still was room for improvement.

ICP was developed as part of a group of current technologies that sought to increase the plasma density through various excitation and plasma confinement techniques. In the ICP system, in addition to mounting the substrate on a powered susceptor driven by an RF

power supply in order to drive the sputtering ions, you have a second field RF power source that separately generates the plasma and confines it to an area upstream of the substrate. This coil is inductively coupled to the plasma across a dielectric vessel wall. These changes were key in decoupling plasma density and ion energy and give the user greater control over feature dimensions and substrate conditions. Additionally, etch rate is higher than RIE since the plasma density is typically 2 to 4 times higher than with RIE.[25]

Here is an example of an ICP reactor.

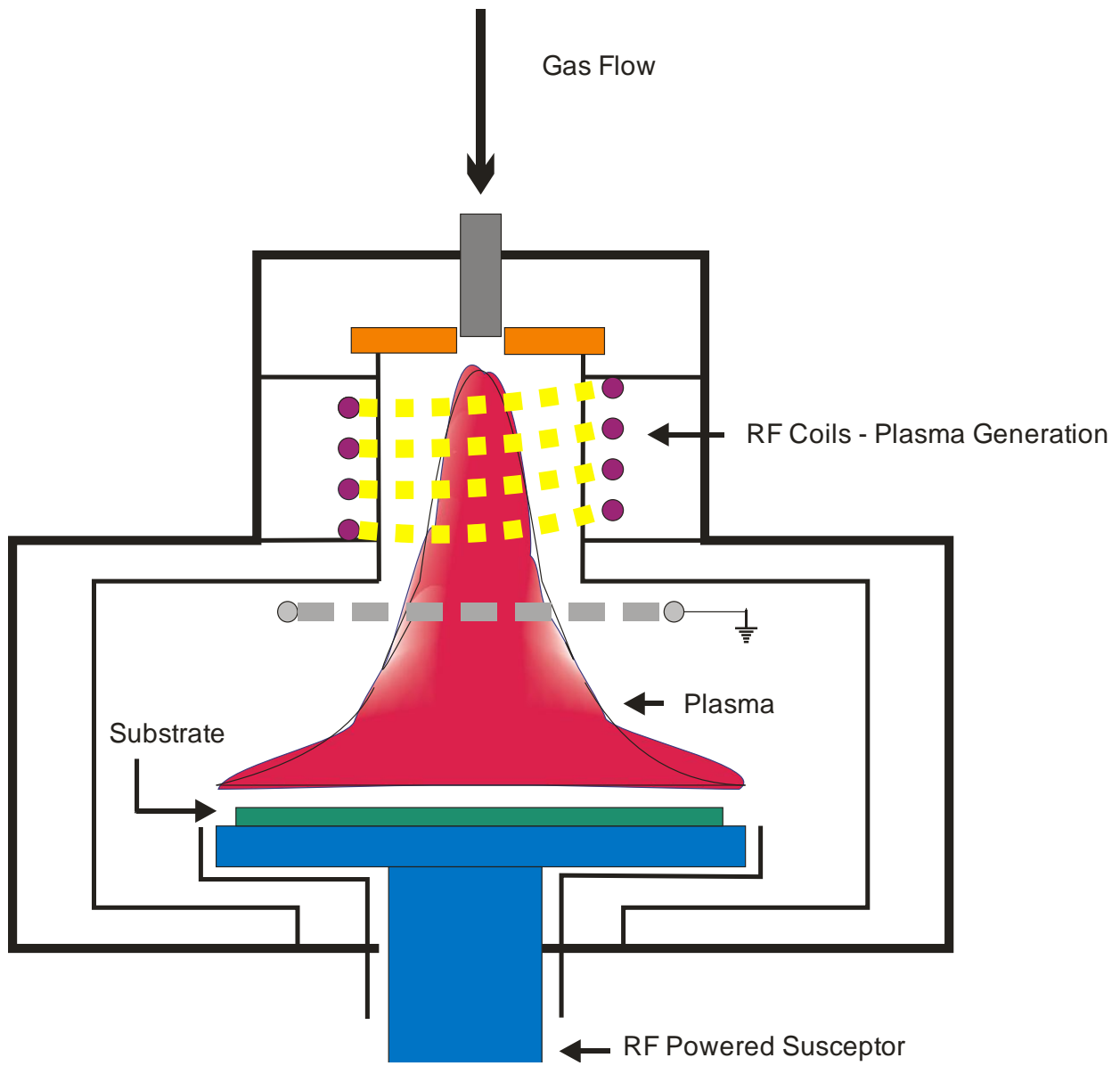


Figure 3-1 General ICP reactor

3.3 ICP Etching of III-Nitrides in Detail

ICP etching is a process that can be divided into two distinct etching mechanisms, physical and chemical. It is the ability of the ICP systems to individually control these separate processes that makes it such a useful tool for device processing. While there are interconnected effects when you adjust the physical and chemical parameters, one has the ability to tailor each individually to achieve the desired result. Many groups have successfully developed robust processes to control these mechanisms and we will cover them before moving on to our experimental results. Through proper control of these parameters we are able to realize effective control of the dependant ICP parameters which result in the properly processed devices we want. These are the etch rate, selectivity and degree of anisotropy.[20-26] The best way to describe the control of these parameters would be to cover how the plasma is physically controlled in ICP and then to cover the chemical aspects and considerations specific to the III-Nitride materials. After that, we will be a position to cover the tradeoffs and etchant considerations that are commonly used in the III-Nitride material systems.

3.3.1 Physical Plasma Parameters

The physical aspects of the plasma have arguably the most important contribution to the whole process of etching. By varying the chamber pressure or the various RF energies we can get entirely different effects with the process. Additionally, while the plasma chemistry determines the volatile reaction products, we can get vastly differing etch rates and anisotropy by utilizing the same chemistry, but different energies or pressure.

We will cover the effects of modifying the physical parameters by reviewing the changes to the following parameters:

Chamber pressure, Plasma density,(ICP RF Power,) and ion energy,(RIE RF power.)

Chamber pressure was one of the modifications that made RIE and ICP much better than general plasma etching. Previous dry plasma etching techniques utilized chamber pressures as high as a few hundred mTorr. While this approach works well for isotropic etching, the combination of low mean free path for the ions, which reduces the sputtering effect, and a resulting increase in selectivity between materials based on varying bond energies of the substrate materials. R.T. Green *et al.* found that the selectivity was highest at 14.1, for GaN:AlGa_N, when using a chamber pressure of 50mTorr when doing gate recessing on their HEMTs.[27] This was due to the fact that, at higher pressures or lower RIE power, the ions do not have the mean free path required to develop enough energy to remove the AlF₃ compound while they still have enough energy to remove the GaF₃. [27,30] That is better for HEMTs however as these devices rely on the gate recessing. With III-Nitride optoelectronics, where quantum well and mesa structures abound, we need to have non-selective etching. As the chamber pressure is lowered below 50mTorr, as in RIE or ICP, you start to realize a highly anisotropic etch with varying degrees of selectivity, surface roughness and stoichiometric surface conditions that are optimum for our devices.

This is due to the increased physical component to our process that is less sensitive to chemical composition than the chemical component. There is however a point where the pressure is too low. Both Pearton *et al.* [27] and Kuryatkov *et al.*[26] found that dropping the pressure below 2mTorr and 5mTorr respectively resulted in a slow, isotropic etch. This was determined to be the result of a rarefied etching environment.

Finally, the last aspect of pressure changes that has been identified is the increase or decrease in surface roughness resulting from the increase or decrease in chamber pressure respectively. This again is due to the shift of the predominant etching mechanism from the physical sputtering to the chemical reaction when the mean free path of the ions decreases. One can however increase the RIE power for the system to compensate for the decreased mean free path. This is a great example of why there are a number of solutions to balancing the physical and chemical effects of etching.

The next physical attribute that can be controlled is the Ion energy in the plasma. This was the sole power variability in the RIE system and is typically referred to as the RIE power on ICP systems. In the ICP system it has the same importance as in the RIE and is nearly the identical electrical configuration in both. While the grounding configuration in the ICP systems reduces the plasma contribution from the RIE power, it does provide the energy to the ions that drives sputter desorption. It works in tandem with the chamber pressure and the chemical composition to determine the etch rate, degree of anisotropy and the surface roughness. If the ions are too energetic, they will cause excessive surface damage. If the ions become even more energetic than that, they will cause the reactants to desorb before reacting with the substrate preventing the chemical etching from happening also known as the adsorption limited regime. At that point they will cause nonstoichiometric conditions on the surface since the more weakly bonded atoms, in our case Ga, will be preferentially etched over the Al. Another representation for the ion energy is the DC bias Voltage and it is simply the representation of the plasma self bias voltage for a given power. Whether the power is reported as Watts or as DC bias really depends on the equipment being used.

Care must be taken to differentiate between the two however as they do not represent the same number, but a linear relation can usually be determined when analyzing the system. Generally, given typical ranges of values, one can make the following approximation, as the RIE power or bias voltage goes up, so does the etch rate, but so does the surface damage.

Plasma power, ICP power or many times just RF power in an ICP system represents the inductively coupled RF power that is responsible for creating the plasma. In the RIE system the power had to not only generate the reactive species and ions in the plasma, but was also responsible for the anisotropic sputtering. ICP enjoys the benefit of much better control of the plasma as one can raise the density of the plasma simply by increasing the ICP power without raising the DC bias, or increasing the ion energy. This allows you to realize 2-4 times higher plasma density than with RIE.[24] The primary response that can be seen to increasing ICP power is that the etch rate will increase monotonically. This is in direct relation to the increase in reactive species and ions available for the chemical etch process. This value will eventually saturate as there is a limit to the concentration of reactive species at the surface. Due to the increased concentration of ions there will be a commensurate increase in surface roughness, but as true with every other value, it will be balanced by changes in the RIE power, the chamber pressure or plasma chemistry. Selectivity of the GaN over the AlGaN isn't sensitive to the plasma power as that has a greater dependence on chamber pressure and RIE power.

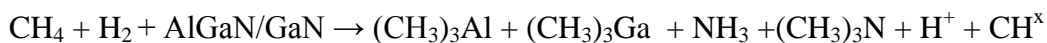
Finally, it can be seen that the control of the physical parameters allows us to choose the process parameters that will work for our intended device.

No one value can be set as they are all interdependent, but there are choices that will work for a range of values. At the end of the day, you will definitely need to determine the optimal setting based on the equipment used and the devices produced.

3.3.2 Chemical Etching Considerations

We have shown, in the considerations of the physical plasma parameters, that there is a wide range of settings that need to be considered when using plasma etching systems. The chemical choices are a little easier as it has long been established that you either go with a chlorine based reactive species, other halogen based one or methane/hydrogen based technique. The most common class for the III-Nitrides is the chlorine based system as is if effective in etching every material commonly grown at high rates with anisotropic smooth profiles. There are a few additions that need to be added to improve performance, but chlorine is still highly popular and serves as the base used for all of our etching. We will begin by covering the typical nitride based material system chemical processes and products of these reactions. We will then cover the alternate systems, their reactions, byproducts and examples of use. We will finish this section with a review of currently utilized techniques. For reference, here are some of the reactants:





Chlorine etching is still the workhorse of the chemical element of III-Nitride material processing. While it frequently is used with a small flow of argon, Cl_2 , BCl_3 and SiCl_4 have been used for processing most of the devices in literature and in industry.[20-23,28-33] technique used in the literature. The complete chemical description of the chemical etching process is beyond the scope of this thesis. Briefly, energetic radicals and ions are formed when the process gas flowing into the chamber is ionized by the ICP RF field. The ionization of the process gas forms a cloud of highly chemically active radicals, due to the loss of shell electrons, and ions, due to dissociation of the process gas. It is these particles that impinge upon the substrate due to the RIE field between the RIE coils and the substrate. These particles are then adsorbed by the substrate where oxidation and reduction reactions create volatile compounds that can evaporate, sublime or are less energetically bound to the substrate. While there are a number of possible compounds formed the primary reactants are the AlCl_x , GaCl_x , InCl_x , and NCl_x products. The etch rates for the purely chemical portion of etching are based on the radical flux to the surface, the energy required for the oxidation/reduction reaction to occur and the volatility of the reactant products and are primarily limited by the III-Halogen reactant. [24] In studies of the relative etch rates of AlN, GaN and InN with Cl_2 plasmas the ratio of etch rates, and resultant selectivity, was in line with the different bond energies of the substrate material.[28,29] As previously mentioned,

while this is a preferential situation for HEMT device processing, for optoelectronic devices this leads to non-stoichiometric surfaces, pits and pillars and sloped sidewalls which will prevent devices from functioning. Many groups have utilized a different chlorine based process gas to get around this limitation. The first is BCl_3 . It has been commonly used for both the primary chlorine source for etching and as a secondary source of Chlorine and heavier Boron ions. When etching III-Nitrides, the chemical etch rate as compared to straight chlorine is slower, due to lack of available chlorine radicals, but it is compensated for by the ion, physical etching due to both the heavier ions and their heavier resultant reactant products as the Boron aids sputter desorption. While it seems that higher ion energy would lead to rougher surfaces, that isn't always the case. It turns out that the addition of the heavier boron allows one to etch the harder compounds that typically aren't etched by the lighter Cl_x radicals. Additionally, Boron radicals tend to act as a getter for oxygen in the chamber. This helps prevent the formation of the Al_2O_3 compound that self masks AlGaIn materials. This is the reason many groups use it as a pretreatment to break through native oxides on the surface of AlGaIn materials prior to the critical etch steps, it prevents the etch delay that frequently occurs.[29] A final Chlorine based etch gas is Silicon tetrachloride. It was one of the earliest reported gas mixes used to successfully etch the III-Nitrides[25] and was basically a carryover from the standard processing with AlGaAs/GaAs system. It was widely used for III-Nitride in the RIE systems early on but has been primarily been replaced due to its slow etch rate.

While Chlorine based etching is the typical, there are a number of different gases also used for etching III-Nitrides. Argon, CF_4 (Tetrafluoromethane,) CH_4 (Methane,) SiF_4 (tetrafluorosilane,) and CCl_2F_2 (Dichlorodifluoromethane,) are some of the other gasses

used. While the chemical composition and resulting radicals are different than the chlorine based etches, the result is similar. Many of these gasses are used to directly address the reduced volatility or etch resistant properties of some of the volatile compounds formed when etching. Selectivity is another key factor that favors using these different gasses. In some cases, selectivity is higher than 40:1 for GaN:AlGaN when using these process gasses due to the hard compounds formed when using the fluoride based gasses which form AlF_3 when reacting with the Al. The highly reactive compounds preferentially etch the less strongly bonded molecules so its etch rate on the nitride materials proceeds in ascending order from In to Ga to Al. Finally, Ar is probably the most common additive to the standard etch process and, while it does not contribute to the actual chemical reaction at the surface, it increases plasma density, plasma stability and improves sputter desorption of reactant products. Ar can also be used for plasma etching by itself, but this isn't commonly done with III-Nitrides.

In addition to the process gas used for the bulk of the chemical etching component, there are a few gasses added to derive specific etch rate or selectivity goals for different devices. These gasses can be the Ar, O_2 , H_2 N_2 and other process compatible gasses. Oxygen for instance has been used to intentionally form AlO_x on the surface of the substrate to act as a rigid mask to preferentially etch the GaN on HEMTs.[33] It is also added to etch materials such as indium gallium zinc oxide, a material that is relatively resistant to standard chlorine based etching.[39] Hydrogen has been added to methane and chlorine processes in order to increase reactant species, but only helps for a small percentage.[38] Nitrogen is commonly added to BCl etching as it helps in dissociation of the BCl and forms the heavier BN_x ions that further assist in sputter desorption. As growth technology improves and material

combinations become more complex, it will be expected that the use of small amounts of additional gasses will continue to supplement the halogen based etching processes.

While there are endless physical and chemical variations that we can use for ICP etching, in practice, there are only a few variations on the process. Chemically, most groups have settled on straight Cl_2 , $\text{Cl}_2 + \text{BCl}_3$, $\text{Cl}_2 + \text{Ar}$ and $\text{Cl}_2 + \text{BCl}_3 + \text{Ar}$. This mixture gives us good etch rates and, by adjusting the Plasma power and bias, can give us anisotropic, smooth walled etches, small feature sizes and rates high enough for manufacturing processes. While it does take some practice, as we will show in the experimental section. It is relatively easy to achieve.

3.4 Experimental Procedures

3.4.1 General procedure

These etch trials were performed on a Plasmatherm/Uniaxis VLR-700 located in the cleanrooms at the Army Research Laboratory,(ARL,) in Adelphi Md. This type of equipment can be equipped with multiple chambers for processing and all are accesses through an automated load lock. The VLR-700 at the ARL has three chambers each dedicated to a separate process technology. This is in line with the practice at many other research facilities where users of various materials systems interact. For instance, the users of the Silicon based bosch process have difficulties with contamination when etching in the same chamber as the three nitrides. The chamber we used for our testing was named PM2 and is used by the other researchers processing III-Nitrides.

The gasses are supplied individually to each chamber through supply lines controlled by the system controller. The gases available for processing are Cl_2 , BCl_3 , SF_6 , O_2 , CH_4 , HBr ,

Ar with a nitrogen or helium purge. This makes the system useful for nearly any material system as it has all the typically used gases for ICP etching. The RF power available for each chamber is from 0-300W at 13.56MHz for the substrate susceptor mounted source, or RIE source. With the ICP coupled source capable of generating from 0-2500W or power at 2MHz. This, as mentioned in the background section, is inductively coupled to the plasma chamber through a dielectric vessel wall and the coils surrounding it. Temperature control for the substrate is provided by a helium backplane cooling system which cools the backside of the substrate. The three chambers, PM1, PM2 and PM3 are arrayed around the load lock chamber and individual samples to be etched are mounted using vacuum grease on a Silicon wafer. The wafer we used to mount samples on had a thick coat of SiO₂ which is far more difficult to etch than the III-Nitrides so we discount the contribution from the by-products of the SiO₂, Si etch. The process for this coating appears in Appendix A.

After mounting on the wafer, the samples loaded into the chamber by the loading system and the etch run begun. The runs were controlled by a PC based controller according to recipes set up in the system. On delivery, the system had a number of pre-loaded recipes based on previous research which serve as starting points, however the group I was working with had a recipe that had worked for their UV-LED structures named III-V so we started with that. The initial conditions for the III-V etch can be found in Table 3.1:

Process parameter	Setting
Gas Flow	30 SCCM
RF1 (RIE) Power	30 W
RF2 (ICP) Power	500 W
Chamber Pressure	5 mTorr
Chamber Temperature	25 C
He cooling backpressure	5000 mTorr
Time	240 S.

Table 3.1: Settings for Etch recipe III-V

The material we are using is a variety of AlGaIn/GaN quantum well heterostructures. These devices are being grown by Dr. Michael Wraback's group at the ARL to be used for UV LEDs. The typical structure for these devices can be seen in Figure 3.2. The quantum well configuration that is required for functional LED devices can easily be modified to perform well as UV laser diodes. The design of the device necessary to produce the LDs appears in Appendix B.

It should be pointed out that these tests were run not as a means to characterize a particular process for research results, but were intended to perfect the process necessary for producing a stable, highly reliable etch process that gave smooth sidewalls and was of sufficient anisotropy to produce a feature sidewall with a slope of no more than 2 degrees from the normal. From calculations performed, this is the minimum value required to get the gain necessary for laser diodes. We will therefore present the results and necessary modifications necessary to achieve this goal.

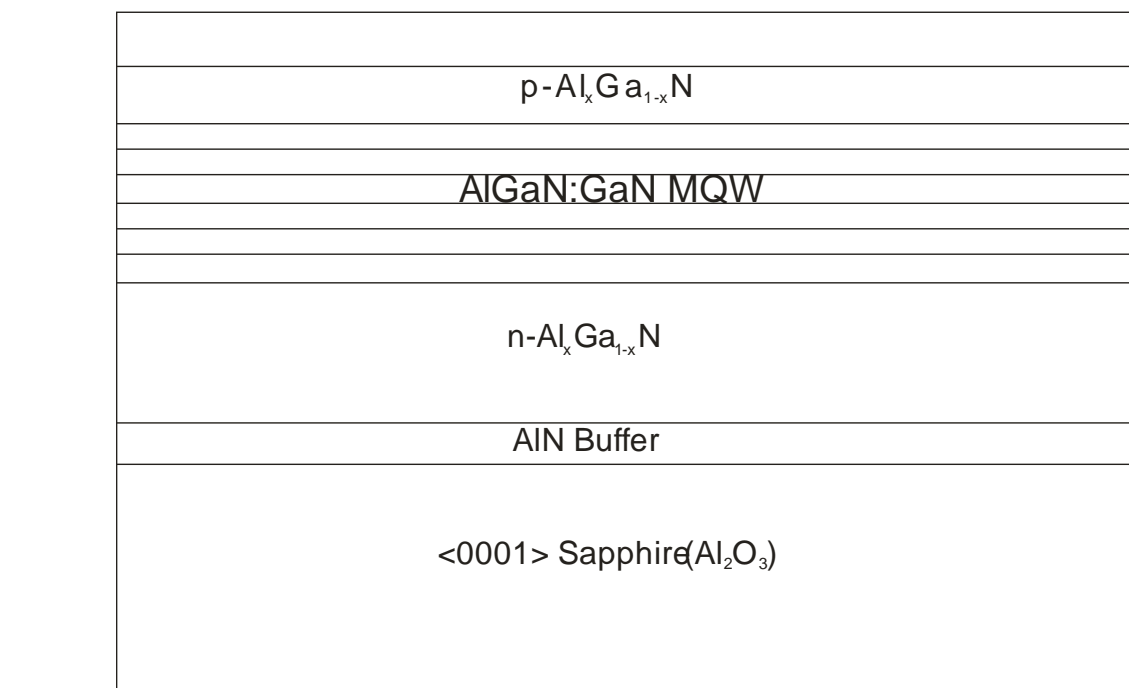


Figure 3.2- AlGaIn/GaN QW structure on Al_2O_3

3.4.2 Experimental Results

Our first run was performed on sample numbers N425M and N356. Both of these material growths feature AlGaIn/GaN quantum wells grown on a buffer layer of AlN deposited on a sapphire substrate. These devices are then cut into 5mm x 5mm square pieces with a dicing saw. After sample preparation, we mount the samples on a Si wafer for use in the chamber and load the samples through the load lock. Our first run we intend to etch up to 5000 angstrom in order to enable us to couple light into and out of the edge of the mesa structure. After loading the sample, we started the standard III-V run as shown above. However, the system had a fault after 30 seconds so we had to restart. We ran the sample for an additional 210 seconds to total 240 seconds of etch, removed the samples and cleaned them with acetone and piranha solution, (See Appendix A for details.) We then ran the samples through a Dektak-II profilometer to measure the depth of the etch. We found the etch to be only 1500 Å on sample number N425M and only 1250 Å on sample N356. These numbers are lower than expected and it was upon visual inspection that we realized something was wrong. As can be seen in the rough surface portion of Figure 3.3, there was highly variable etching. We made no attempt to measure RMS across the surface. I determined that the reason for the highly variable surface etch was simply incomplete removal of the photoresist in the previous development step... Unfortunately I did not determine this until I had stripped the oxide layer, re-deposited the oxide, re-processed the devices and ran the etch test again. In Figure 3.4 you can also see the effects of misalignment of the masks for the mesa structures and the resulting reprocessing of device N356.

From Figure 3.4 it appears we are starting in the right direction. We did notice however from the initial processing pieces that we did not have a consistent etch rate overall. Our values for etch rate varied wildly from 10 Å/sec. all the way up to 50 Å/sec. As we determined our likely cause of deviation was the poor process control we spent several weeks running dozens of samples through the etch process.

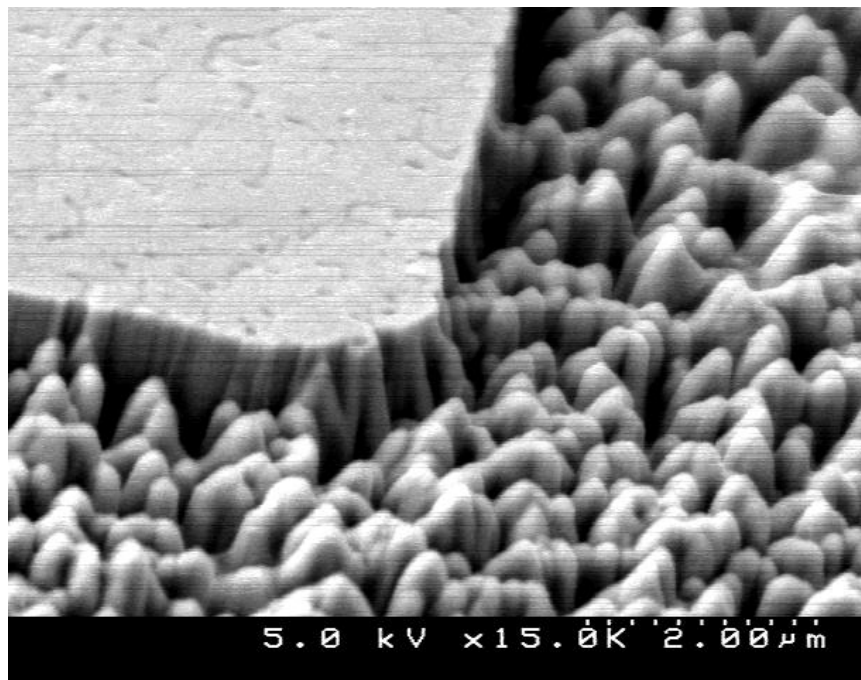


Figure 3.3 Incorrect processing of N325

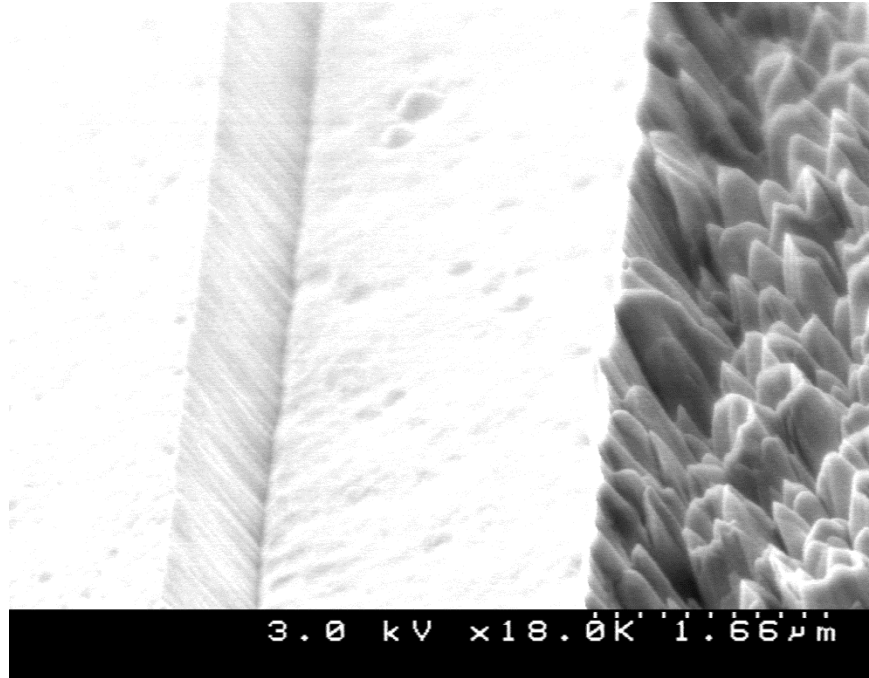


Figure 3.4- Second run of material showing offset of mask and material effects

After several weeks of etch testing we had achieved a consistent etch rate with the devices tested. For the 120 second etch we consistently had $25 \text{ \AA}/\text{sec.} \pm 0.5 \text{ \AA}/\text{sec.}$ across 81 separate devices etched. However, as the time increased, our etch rate declined.

For instance, while we continued to etch as time went on, as we got to the 240 second etch runs our rate declined to 21-22 Å/sec. and as we further increased the time to 480 seconds for the etch the rate declined even further to ~15 Å/sec. While we input the RIE power as the RF power we want to use, the VLR 700 does provide a reading of the plasma self bias (DC Bias.) One would expect that if the decrease in etch rate were due to oxidation of the surface of the substrate which increases the resistance of the RIE circuit or a related effect that our DC bias reading would change, (since the RF power input is constant.) We did not see any changes in the DC bias reading as the etch times were increased. This led us to believe that formation of chemically etch resistant compounds were formed on the layer being etched. These compounds did not have the volatility to evaporate on their own nor did the ions we use have sufficient energy to clear the surface. So, even though we were consistently etching the material at a slow and steady rate, we determined that we needed to modify our process to make it time independent. We will cover the changes we made in the next section as it comprises the second series of test runs we made in developing our process. For now we will take a side topic that is a good measure of the quality of the etch process. The first is the measure of the RMS roughness on the surface of the etched material. The second, a measure not typically reported in research, but vitally important to batch processes, uniformity. We cover those here.

RMS roughness, or RMS Surface roughness, is the statistical analysis of the variation in height across the material. In the various etching processes it is used as a measure of the amount of damage the ions cause on the surface of the material. In our case, it is also a good indicator of the selectivity of our process as an etch run that excessively etches Ga over Al will result in a rougher surface as well.

For all of our measurements we used a SEM to measure the deviations in height across a section of the surface of the etched material and utilized the following formula for the RMS roughness:

$$RMS\ Roughness = \sqrt{\frac{1}{n} \sum_{i=1}^n y_i^2} \quad (41)$$

Where y_i is the deviation in the height from the average value and n is the separate measurements of y . Our very first run we didn't even bother to measure the RMS value as it was obvious that the etch was poor. For the series of runs with just Cl_2 we found the different runs to vary between 6-14 nm with an average value of 10.5nm. While this is a good value and is close to other groups we will need to improve this in our future run.

Uniformity is the measure of the consistency of an etch across the surface of the substrate. While it isn't a value that is reported in literature, it is a very important measurement for batch processing of optoelectronic devices as the thickness of the buffer layers and the processing tolerances are dependent on this value. A high percentage of uniformity will necessitate either a lower yield target or redesigning the device to increase the allowable thickness tolerances. The standard formula we used for uniformity is:

$$Uniformity\ (\%) = \frac{[E_{Max} - E_{Min}]}{2 \sum_{i=1}^n \frac{E_i}{n}} * 100 \quad (42)$$

Where E_{Max} , E_{Min} , are the maximum and minimum etch depths across the range of measurements and E_i are the individual etch measurements across that range.

We used a Dektak II profilometer to measure the etch depths across the etched substrate. The Dektak II uses a diamond tipped stylus to drag across the surface and utilizes a piezoelectric element to provide voltage feedback to characterize the surface. The system we utilized is completely automated and will automatically measure a grid of values. Utilizing this profilometer, we had values of uniformity that were as high as 35% from piece to piece. As we improved our process we were able to reduce that value down to an average 12% across 3 samples 10mm apart. When we measured the uniformity on individual 5mmx5mm pieces, that number was on average 3.9%

While the initial test run using the standard III-V etch program was consistent, with good uniformity, relatively low RMS roughness, good feature anisotropy and smooth sidewalls, it did suffer from a low etch rate that was dependant on the etch time. This wouldn't be a good process to use for any device so we implemented a few changes. If we recall the theories presented in the introductory section of the chapter we will remember that the following actions will raise the etch rate:

Raise the ICP power to increase plasma density

Raise the RIE power to increase ion energy

Introduce heavier ions to assist in sputtering

Introduce more chemically active species that attack difficult to etch products

Raise temperature

Raise pressure, (To a small degree)

Increase process gas flow

While all of these will help increase etch rate, they will not always provide optimal results. For instance, recall that raising the RIE power will increase ion energy, but at the expense of a higher RMS and surface damage. We must be careful to modify the original III-V etch to optimize our results. We identify that we need to increase ion energy slightly and increase the chemical activity slightly. To this end we elected to first introduce BCl_3 to the Cl_2 process gas.

BCl_3 has several beneficial effects, in addition to increasing the concentration of radical Cl in the mix, thereby increasing the chemical action, it also serves to stabilize the plasma giving us a more uniform etch. BCl_3 is also very good at scavenging Oxygen present in the chamber which prevents the formation of Aluminum oxides which are very difficult to sputter. BCl_3 in small amounts is one of the most common additions to straight Cl_2 based etching. As a side note, we did also think of using Argon as an addition to the process gas, however we were concerned with damage so, unless it was absolutely necessary, we were determined not to use it.

The second modification we chose to make was to increase the RIE energy from 30W to 100W. We determined that this would increase the etch rate, in conjunction with the addition of BCl_3 , and it would sputter the products that were forming on the longer etch time substrates giving us a time independent etch rate. This modification would get us the additional etch rate for the substrate but without the BCl_3 addition we would realize unacceptable roughness on the surface and sidewalls. In discussions with Dr. Charles Collins, who used the same equipment to process UV LEDs based on the same material, it was determined that they're second step from the standard III-V etch program was to simply increase the RIE power,(DC Bias) [39].

The key difference was that with the LED devices, it was found that a rough surface allowed better ohmic contacts to the LED. Additionally, they were not worried about sidewall roughness or the angle of the sidewalls relative to the surface normal as roughness tended to improve output efficiency of the LED devices. They raised the RIE power to 200W and reduced the ICP power to 350W to get the effect they wanted, we will keep ours at 100W and 500W respectively.

When we take a look at the effect of simply adding BCl_3 to the Cl_2 etch. We expect that this will serve several purposes. It will make the plasma more stable and easier to light that before with just Cl_2 , we also expect a slight increase in the etch rate. We changed the flow rates for the gasses on the III-V recipe to the following:

Process parameter	Setting
Gas Flow	30 SCCM Cl ₂ :30 SCCM BCl ₃
RF1 (RIE) Power	30 W
RF2 (ICP) Power	500 W
Chamber Pressure	5 mTorr
Chamber Temperature	25 C
He cooling backpressure	5000 mTorr
Time	240 S.

Table 3.2: Settings for Etch recipe III-V modified to include BCl₃

What we found was that the sample etch rate went up slightly from the Cl only rate of 25Å/sec. up to 32Å/sec. And, as we were concerned with the smoothing benefits of BCl₃ we measured the RMS roughness of the etched substrate and found this value had improved to 7.5nm over the 10.1nm from just Cl₂. It is obvious that we are moving in the right direction, now we needed to increase the etch rate even further by changing the RIE power. In figure 3.5 you can see the improvement in the smoothness of etch. The sidewalls are where they need to be in terms of being smooth, however they are at too steep an angle. Additionally, the pits you see are evidence that there is too much selectivity in the etch as the radicals are preferentially etching the GaN over the AlN. This shows us that while the BCl₃ addition helped, we still need to increase the physical etch.

Etch rates are highly dependant on the RIE power as we have seen. Our original recipe started with only 30W RF power since this was what the existing etch recipe had. While we could get smooth devices with this power, we really needed to increase etch rate as the mesas we needed to etch for our devices were on the order of 1.95-2um in height. This would require us to make a run 15 minutes long, too long for a process. We decided to increase the RIE power to 100W but that wasn't the only modification, the important value in the physical sputtering isn't necessarily the RIE power, but the DC Bias that drives the ions. We need to ensure that not only the power but the bias as well was consistent in our trials. For our first trials we ran the recipe listed in Table 3.3, the standard III-V recipe with the RIE power increased to 100W.

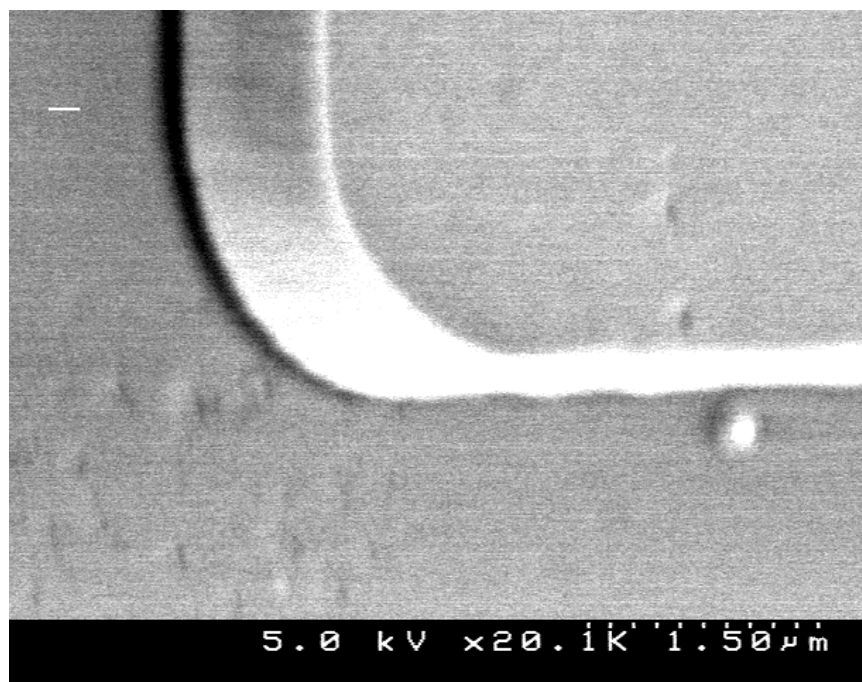


Figure 3.5 Etch after addition of BCl_3

Process parameter	Setting
Gas Flow	30 SCCM Cl_2
RF1 (RIE) Power	100 W
RF2 (ICP) Power	500 W
Chamber Pressure	5 mTorr
Chamber Temperature	25 C
He cooling backpressure	5000 mTorr
Time	240 S.

Table 3.3: Settings for Etch recipe III-V RIE 100W

We immediately saw a sharp increase in etch rate. The rate increased to as high as 53 Å/sec. however there was a problem. The etch rate was as low as 31 Å/sec. on some material. We noticed that the effectiveness of the thermal grease bonding and the type of wafer impacted the conductivity of the circuit thereby changing the plasma self bias,(DC Bias.) For the low etch rate the DC bias was only 189 V while at the higher etch rates it was 240 V. We switched over to the sapphire wafer and were careful to apply exactly the same amount of thermal grease each time. By making these modifications we were able to consistently generate a DC Bias on the system. This lowered our etch rate slightly, but we was offset by the resulting consistency of the etch. Our new, stable etch rate was 45 Å/sec. with a RMS roughness of 8.5nm. This etch rate remained consistent from 5000 Å etch all the way up to 2.5um. We tested this run by putting in a structure that we needed to etch exactly 1.95 um. This should have taken 435s to etch. When we tested it, the etch was exactly 1.95 um deep. More importantly, the etch test was run on the MQW LED material and did not exhibit even a moderate level of selectability which is key as our devices need to etch at the same rate and the mesas need to have uniform sidewalls.

Now that we have determined how to properly adjust the settings for our etch we are finally ready to tackle the finished devices. It appears that the most effective modification to the standard recipe was to increase the RIE power to 100W. The only question is how much BCl_3 should be added to stabilize the process and improve the etch. We started with equal amounts of Cl_2 and BCl_3 , both at 30 SCCM. While this worked well, its etch rate was fairly low, 42 Å/sec., and we wanted better roughness in the etch. We thought that we might get better results if we combined multiple effects into one device. We opted to keep the chamber pressure low and the gas flow rate low to decrease selectability.

Additionally, we increased the RIE power to compensate for the reduced rate from the low gas flow. WE then added a small amount of BCl_3 to our proven Cl_2 recipe to come up with the following recipe:

Process parameter	Setting
Gas Flow	15 SCCM Cl_2 5 SCCM BCl_3
RF1 (RIE) Power	100 W
RF2 (ICP) Power	500 W
Chamber Pressure	5 mTorr
Chamber Temperature	25 C
He cooling backpressure	5000 mTorr
Time	180 S.

Table 3.4: Settings for Optimized Etch recipe

We knew we were successful immediately, all of the trials were within +/- 8 V on the DC bias, the plasma lit immediately and was consistent and the devices looked exactly the same. After oxide removal, the process parameters were:

Etch rate- 55 Å/se.

Etch depths tested – 5000Å to 2um

DC bias Range- 238-246 V

Average surface roughness- 2.5nm

Uniformity across separate samples- 1.9%

Slope of sidewall from normal- Less than 2%

As can be seen, from these numbers we have the process necessary to produce our devices. SEM images show the quality of the etch and the smoothness of the sidewalls. It should be noted however that the sidewall image is taken at an oblique angle resulting in the perception that it is sloped steeply. Upon measuring the value is less than 2%. Figure 3-6 shows the smoothness of the sidewalls and the degree of anisotropy we were able to achieve. Figure 3.7 shows several aspects of the process. You can see that there are no pits in the etched material and the sidewalls are uniform showing we were able to get low enough selectivity. Additionally, you can see how smooth and uniform the etched surface is. It should be mentioned that the kink in the edge of the device has been transferred from the photomask and isn't a defect in the process. As a final example, Figure 3-8 is an SEM image of an unmounted, commercially developed UV LED mesa structure that was the height of processing technology at the time of these experiments.

Notice the high degree of selectivity, rough sidewalls and pits on the etched material. This device functions so we can be assured that, given proper processing, our devices will function as well.

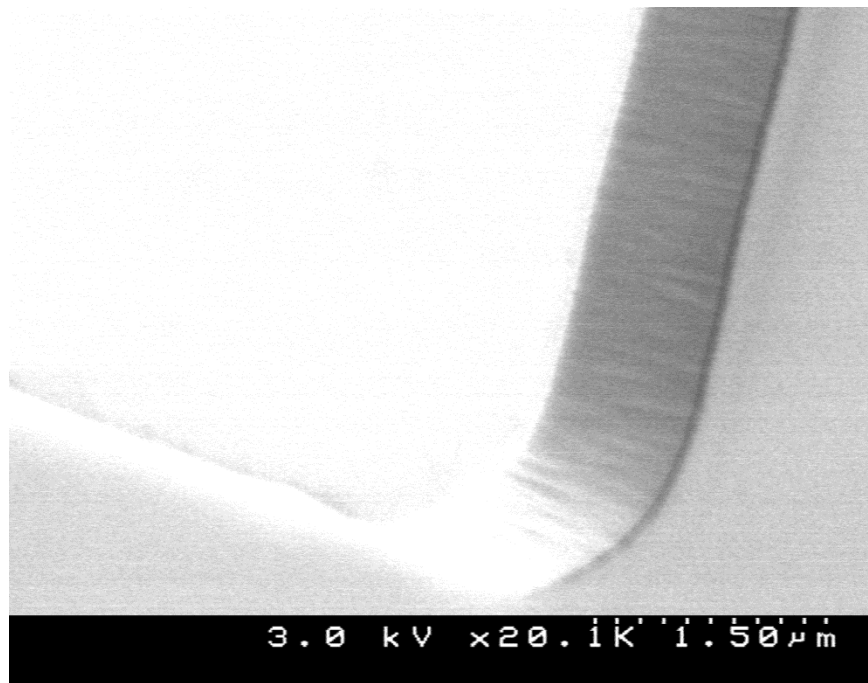


Figure 3.6 Image showing the quality of sidewall from the final etch process.

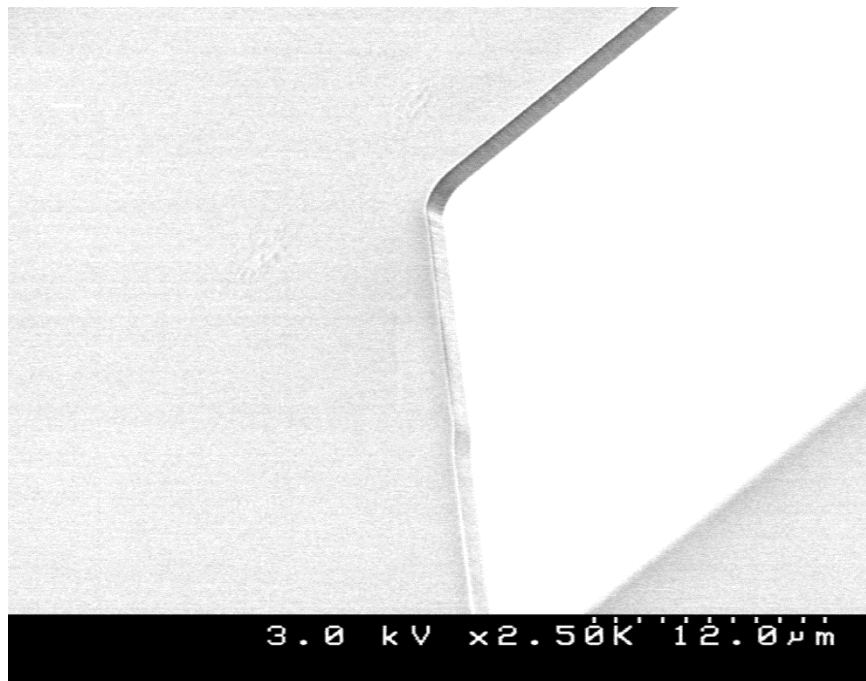


Figure 3.7 SEM Image showing the uniformity and anisotropic etch of the mesa structures using the optimized etch process.

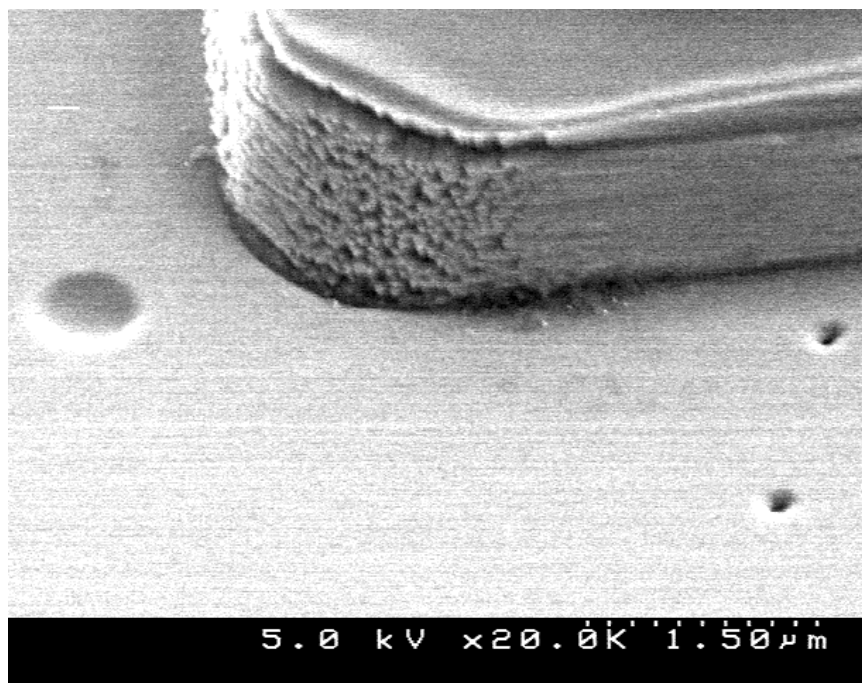


Figure 3.8 Commercial version of the same device types.

3.5 Conclusion

Our goal of successfully developing a stable, reliable etch process for fabricating UV laser diodes has been met. We have shown that our final process meets all stated metrics in terms of etch rate, surface roughness, anisotropy, uniformity and speed. Additionally, we have covered the basics behind the ICP etching process, its history, the physics behind the process and the different process techniques used to perfect device processing. It is our hope that one can use these discussions and results to successfully develop their own process for future devices. While the ICP etch process is only part of the fabrication of the final device, it is critical that one gets this step right in order to realize efficient, functioning devices.

CHAPTER IV

EFFECTIVE BONDING OF LASER DIODES TO HEATSINKS

4.1 Introduction

A matter of great importance to the overall design and production of any semiconductor device is providing the interface necessary between the device and the outside world. Semiconductor devices seldom are processed originally having environmental protection, mechanical support or contacts. This necessitates the use of some sort of package to ensure protection from the elements, provide support and electrical contacts. Electrical or optical connections also must be made in order for optoelectronic devices to work. Thermal connections must be made to remove excess heat which can cause device degradation and reduced lifetime. And finally, we need to provide a stable physical platform to mount these devices. While covering all of these items is beyond the scope of this chapter, we will address providing good electrical and thermal contact to AlGaAs:GaAs laser diodes in order to improve their packaging's thermal and electrical conductivity. By doing this, we hope to not only provide a simple method for mounting these diodes, but to also lower their threshold current and increase their quantum efficiency.

4.2 Background

When determining the proper technique to employ in bonding laser diodes to heatsinks there are numerous techniques to consider. Polymers filled with metallic particles are fairly popular due to ease of use, elasticity and low temperature processing and have been the choice for packaging our diodes for testing [42]. While the epoxy utilizes Ag particles to improve its thermal and electrical conductivity, it still has lower conductivity than hard solders and is difficult to accurately and consistently gauge the thickness applied and to place the diode parallel to the surface of the heatsink every time. Soft solders such as Pb based solder or Pb-Sn or Pb-Ag are also easily used materials for bonding. These are typically used for clip chip or SMT bonding [43], and exhibit good thermal and electrical conductivity. However, these bonds exhibit low thermal tolerance and poor mechanical stability at relatively low temperatures as they tend to soften at temperatures as low as 100 °C. While some mixtures, such as $\text{Sn}_{0.97}\text{Pb}_{0.03}$, are more resistant to strain, they do suffer from thermal fatigue and deformation [44]. A final issue with soft solder is creep. The solder tends to creep up the facets of the laser diode causing the device to perform poorly or fail altogether. Hard solder such as AuSn, AuGe, AuIn are proving to be the best choice for bonding. All of these solders exhibit high thermal and electrical conductivity as well as no creep as their melting temperature is far above what will be realized for junctions during operation. These solders will introduce a level of strain to the device, but that has been found to be minimal when the solder joint is well formed and without voids which leads to localized stresses high enough to cause cracking [45]. Of prime concern when dealing with AlGaAs devices is processing temperature. If we raise post annealing processing temperatures too high we will cause migration of the active layers resulting in device failure. This was the reason for initially

using solder paste instead of a hard solder. Temperatures below 400 °C are safe to use. If we look at the following table, we can see that there are a few choices for hard solder, and soft solder bonding methods based solely on temperature concerns [46].

Alloy	Melting Point (°C)	Thermal Conductivity (W/m°C)	Thermal expansion (10 ⁻⁶ /°C)	Bond Strength (MPa)
Hard Solders				
Au-20Sn	280	57.3	15.9	275
Au-12Ge	356	44.44	13.3	185
Au-3Si	363	27.2	12.3	220
Soft Solder				
Pb-60Sn	183-188	50.6	24.7	1.5
Pb-5Sn	308-312	23	29.8	14.8

Table 4.1 Properties of Hard and Soft Solder Alloys

Alloy	Electrical Conductivity ($\Omega\cdot\text{m}$)
Au-20Sn	16.4×10^{-8}
Pb-60Sn	15×10^{-8}
Au-40In	5×10^{-8} [47]

Table 4.2- Electrical Conductivity of sample hard and soft solder

From Table 4.1 we can see that the thermal properties of the varying alloys are similar, and the electrical conductivities are similar, but the real difference is in the longer term reliability and ease of formation. Our initial attempt at bonding was performed using the Au-In bonding process. When we analyzed the phase diagrams, it appeared that we would be able to bond at a temperature as low as 157 °C, well below the onset of detrimental diode effects. We ended up having difficulties with that process, which we will cover later. We then decided to go with the Au-Sn bonding process. This ended up being far more successful and is the process we developed to move forward with. We will now cover the two bonding processes briefly then move on to experimental results.

4.3 Bonding Dynamics

4.3.1 Au-In Bonding

The use of In bonding on AlGaAs/GaAs laser diodes has been around for some time. It was found to be relatively immune to long term degradation and did not cause any residual stress in the bond [50]. It was also highly compatible with the processing steps as Au was already used to form the contacts for the laser diodes. Additionally, the Au-In bonding process is commonly used in flip chip procedures. In bumps are deposited on the surface and used for a low temperature bonding procedure. This is initially where we got the idea to make our first attempt at bonding with In and Au. In order to understand the metallurgy behind the process, we need to go no further than the binary phase diagram for the Au-In system shown in Fig 4.1.

Before we get into the phase diagram we do need to cover some brief terminology. The Au-In phase diagram is called a binary phase diagram because it, and its resulting alloys, is a combination of two constituent components. On the left you will see the temperature for formation of each of the compounds. Across the bottom you will see the atomic percent of indium in the alloy that is present. There are a series of lines in the diagram. The most important is the topmost line in the graph. It is called the liquidus line. It is the temperature above which the alloy will be liquid. In the case of the In, you can see on the right side that In melts at 156°C. As the temperature increases the Au actually dissolves into the liquid In forming a liquid that is both Au and In. As you increase temperature you see that eventually, at the melting point of Au, everything will be melted. At that time, you will have a stoichiometric liquid based on the amount of each material that is present. What happens in

between those points depends on solubility of constituents, diffusion, time at certain temperatures, and finally rate of cooling. We are attempting to achieve what is referred to commonly as 'Eutectic' bonding. Let us cover the commonly used terms in binary phase systems:

Reaction	Constituents
Eutectic	Liquid \leftrightarrow Alpha + Beta
Peritectic	Liquid + Alpha \leftrightarrow Beta
Monotectic	Liquid \leftrightarrow Alpha + liquid Beta
Eutectoid	Alpha + Beta \leftrightarrow Gamma

Table 4.3- Common invariant reactions in binary phase systems

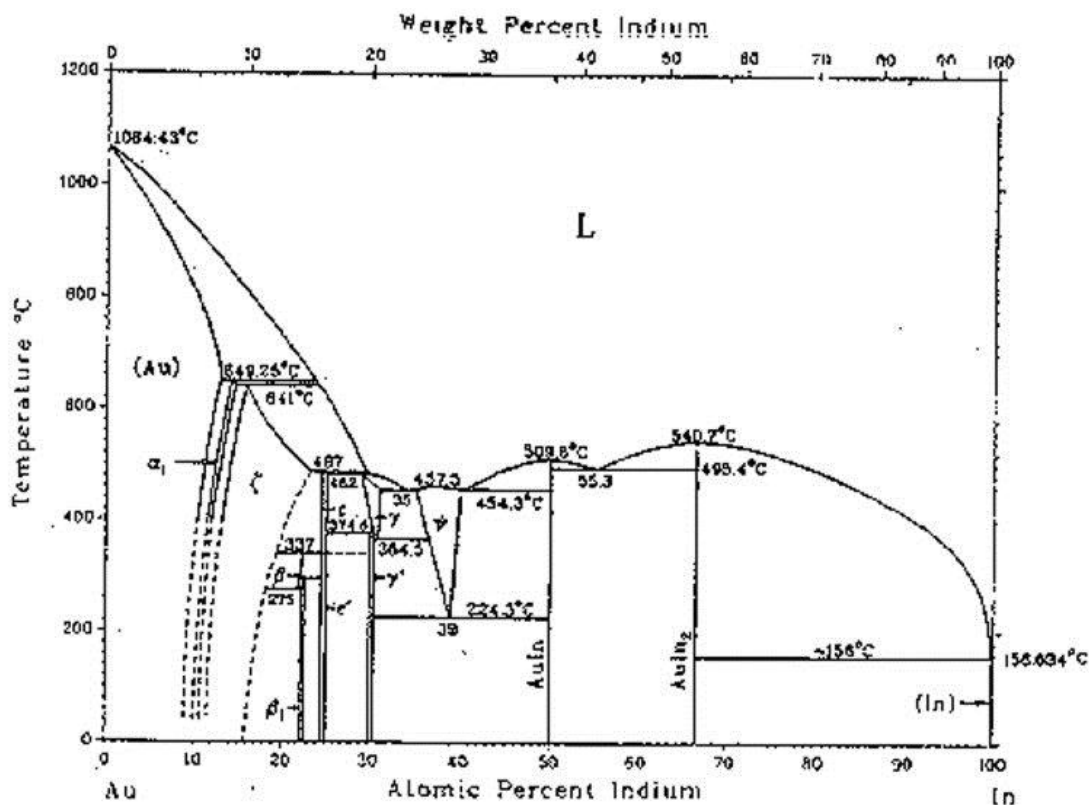


Figure 4.1- Au-In Phase Diagram

From this we can see that in a eutectic invariant reaction we will get an alloy of solid alpha plus solid beta. This is exactly what we want, but we have to control the temperature and concentration of the constituent materials in order to get the desired eutectic alloy.

During the process of forming the alloy, we can realize peritectic alloys. These are formed when the material with the higher melt temperature forms alpha rich materials in a liquid beta. This will happen if say the alpha is far from its melt point and exhibits low solubility and diffusion rate in beta. The final one we will concern ourselves with is the monotectic alloy which occurs when there is no solubility or diffusion of alpha in beta, something we will not cover however. When we look at the phase diagram we can see several horizontal

lines, several vertical and various arcs. These lines denote the regions where different eutectic, peritectic and monotectic alloys form. Briefly, when you are in the liquidus region and you start to cool your alloy the finished eutectic alloy will be determined by the ultimate temperature reached and the concentration of constituents in the liquid. For instance, if we look at the Au-In phase diagram, suppose we have the alloy at a temperature of 460°C. Assuming we were not limited in the Au supply, as we cool the mixture back down we will eventually form a eutectic alloy comprised of ~40% alpha (Au) and 60% beta (In.) While in actual practice, there are other factors that will come into play, the general effect is the same for all phase diagrams. The vertical lines represent separation points for different alloy atomic configurations. These are controlled by controlling the percent weight of the different constituents, for instance, in the Au-In phase diagram, if we were to heat the mixture up to 510 °C and then cool the alloy down while maintaining 51% In in the alloy then we would form AuIn₂. If we were to maintain the beta (In) at 49%, we would end up with AuIn instead.

Horizontal lines, where they intersect the vertical lines, represent peritectic points. These are the points where one material starts to solidify. If we look at the AuIn phase diagram we see this at the point where 67%. If you look at the point at 495°C you see one of the peritectic points for the AuIn phase diagram. Horizontal lines on their own also represent delineation between two types of solid. For instance, two in the AuSn system, which we will show next, the line at 13.05°C and 100% Sn denotes the split between α Sn, a semiconductor, and β Sn, a metal both existing at similar concentrations, but different temperatures. It also serves as a line along which you will see continued dissolution of the alpha material in beta which will continue as long as there is sufficient alpha, or in this case Au, available.

When forming alloys it is important that we get to a eutectic alloy for multiple reasons. First of all, the eutectic points represent stable alloys. The peritectic and monotectic points frequently form alloys that are either not stable or are intermetallics. Intermetallics are highly brittle, with poor conductivity so we need to form the eutectic alloys. When we look at the Au-In phase diagram we see that the lowest eutectic point is around 454 °C. This is far higher than we want to use as a bonding temperature, fortunately we don't have to use such elevated temperatures. Recall the horizontal line at 157 °C. This line represents the process where the In starts to melt. Au is soluble in In and as the In wets the gold it forms AuIn₂. As long as we continue to provide Au for the reaction we will form AuIn, the stable eutectic, which will in turn form more AuIn₂. This process will continue until all available Au is consumed or we drop the temperature. Once the AuIn₂ has been formed, it will be stable. If there remains an excess of Au in the alloy, the AuIn₂ will form stable AuIn. This process is a slower solid state reaction and is the reaction process that occurs in sputtered In on Au even at room temperature.

4.3.2 Au-Sn Bonding

After our initial trials, and failures, with the Au-In based solder process, we needed to find another lower temperature bonding technique that would meet all of our criteria. If we look at the chart of various hard solders we see that Au-Sn is another promising candidate. Au-Sn has been utilized in the environmental packaging of electronic devices as it can be easily bonded to metal and ceramic packages used in military and commercial applications. From table 4.1 and 4.2 we can see that it has good thermal and electrical conductivity and is compatible with our process. Stress analysis of the resulting bonds show that for the case where there is one alloy junction [50], and two alloy junctions [45,46], the tensile stress

increases when the alloy hardens, however, the force of this stress is less than with any other hard solder. And, as long as we have void free alloy formation, this stress can be easily handled by the bonded device [45]. A final important property of the Au-Sn solder system relates to the diffusion of Au and Sn. There is a high degree of diffusion that goes on even at room temperature. The Au atoms will diffuse into the Sn even at room temperature and interstitially form AuSn alloys as long as we place them in intimate contact, such as sputtering or vapor deposition. This shows us that we can bond with minimal effort. We will now cover the phase diagram of the Au-Sn system and the important alloys formed.

As we have already covered the phase diagram theory in the previous section we will get to the discussion of the specific properties of the Au-Sn alloy. As before, we should start with the phase diagram seen in Figure 4-2:

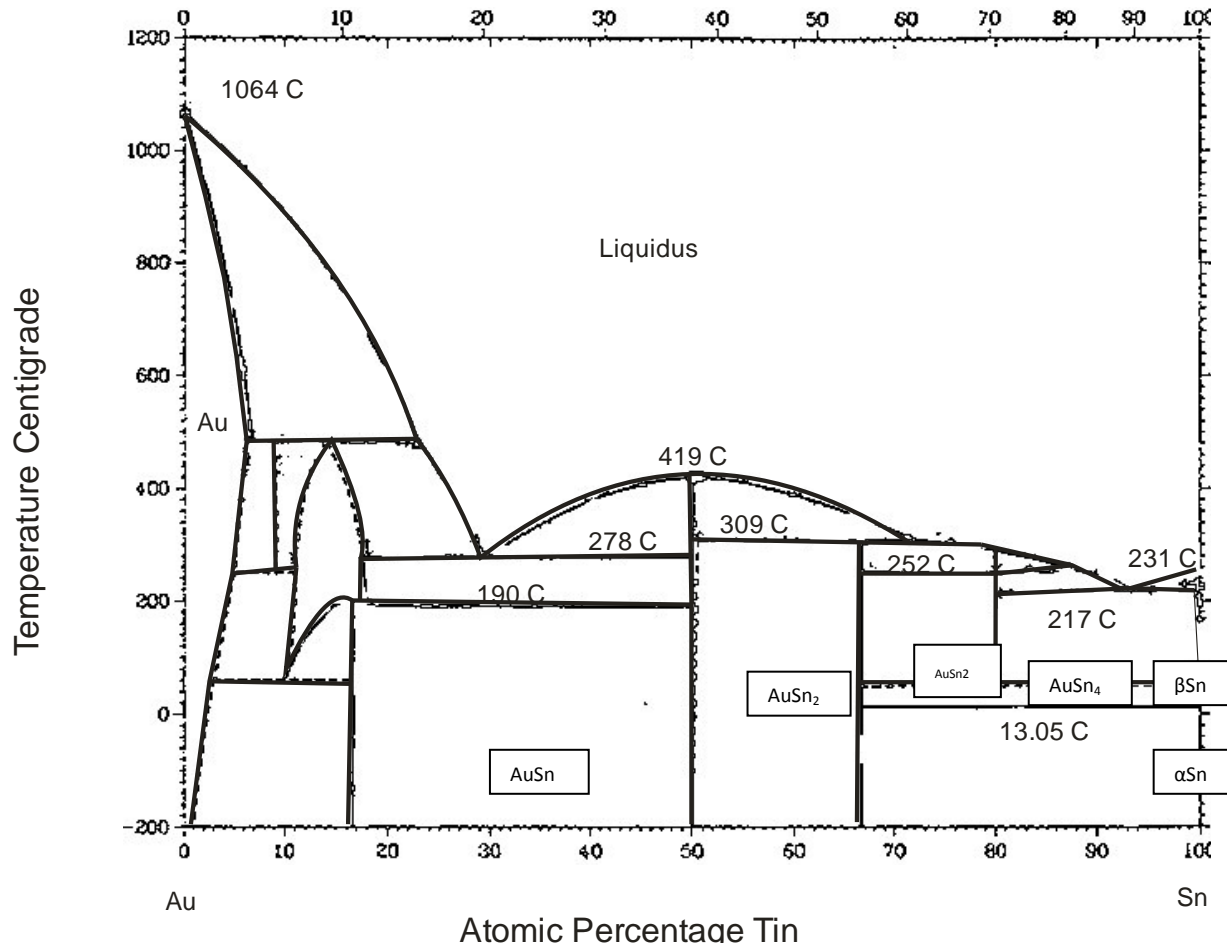


Figure 4.2 AuSn Phase Diagram

There are many different alloys that are formed such as terminal solutions of Au, β Sn, α Sn and many alloys such as Au_{10}Sn , Au_5Sn , AuSn, AuSn_2 and AuSn_4 . The resultant alloys are a combination of the available Au, Sn and the temperature. In the phase diagram we can see that there are two clear eutectic points, one Au rich at 280°C and the other Sn rich at 217°C. While the entire range of alloys is important, we are only concerned with the small range that impacts us. And, while we could use either the Sn rich or the Au rich alloy there is

a big reason to go with the Au rich alloy despite its higher processing temperature. The Sn rich alloys and the intermetallics, have been found to be responsible for most solder joint failures and cracking. For this reason we chose to go with the 280°C Au-rich eutectic which forms AuSn primarily, but can continue to form Au₅Sn at room temperature over long time periods. This is not perceived to be a problem for the diode lifetime.

4.4 Experimental Procedures and Results

4.4.1 Introduction

The experimental processes can be broken down into four distinct sections. The first two are the In and the Sn deposition procedures, followed by the annealing of the diodes and finishing with the measurements of threshold current, quantum efficiency and a brief study of bond quality. We will utilize the standard 4mm X 4mm copper blocks coated in 3.5µm Au to bond our devices to. These blocks are what all our testing to date has been done on and the thermal and electrical conductivities, as well as physical dimensions, make them ideal to use as a substrate for testing the laser diodes.

We will deposit either In or Sn on the blocks using thermal evaporation and in the case of the Sn, we will deposit Au using an e-beam evaporator. Once the metal is deposited on the block, we will mount the laser diodes, p side up, on the blocks, put them in the holder, and anneal them at the specified temperatures. After cooling, we will test the devices to determine if there are changes in threshold current and efficiency.

4.4.2 Evaporation and Bonding of In, Sn and Au

Evaporation of the metals we are using for soldering is performed by thermally, or in the case of Au, e-beam heating of the source material which causes rapid evaporation of this metal. If we place a substrate in a high vacuum chamber we will coat nearly everything in the chamber with a layer of that metal. This coating is fairly robust to begin with, but after heating they will bond to the gold layer of the heatsink block. We used two separate chambers and processes for the evaporation so I will cover each separately. Both the evaporation of metal and the bonding of the diodes to the heatsink blocks are performed in a custom holder I fabricated that holds the blocks in proper placement for evaporation, and have leaf springs that will apply pressure to the diodes to ensure void free bonding. This holder can be seen in Appendix C.

Evaporation for the In layers was performed on an Edwards Auto 360 Thermal evaporator. This equipment is comprised of a resistive heating element that evaporates the sample material which is loaded in a titanium boat. This resistive element is at the base of an evacuated chamber topped by a large bell jar. Samples are mounted on a rack at the top of the chamber and deposition is controlled by a shutter between the source material and the substrate to be coated.

Monitoring of the deposition rate is accomplished by monitoring the loading on a piezoelectric crystal mounted at the top of the chamber. To calibrate the system, we enter the density and Z-factor for the material and the system then automatically calculates the thickness of deposited material based on changes in the loading of the crystal. The source material we use is electronics grade In, 99.99999% pure. More detailed instructions can be

found in Appendix C.

To start the process, we rinse each block in acetone to remove any contaminants then dry with N₂. We mount the heatsink blocks in the holder then mount the holder in the carriage at the top of the bell jar. We load a predetermined amount of In, enough to ensure that we don't run out before enough material is deposited. Once that is ready, we lower the bell jar and press run. Once the vacuum seats the bell jar we can let go and wait for the system to pump down to approximately 6×10^{-7} mTorr. Once we are at this pressure, we can push start and turn the current control to maintain a current of ~150Amps. At this current we will deposit approximately 25 Å/sec. Press run again to open the shutter and wait 20 min. This will deposit approximately 20,000 Å of In. After 20 min. pressing run again will close the shutter, turn the current down to zero then off, wait several minutes then press vent. Once the system has gotten to atmospheric pressure you will hear a whoosh sound, simply raise the bell jar and remove the samples.

Once we have the In coated heatsinks we take the already manufactured AlGaAs laser diodes, which have a Au coated p-side electrode. (As an aside, the laser diodes also have a Ti/Au blocking layer that will prevent In from diffusing into the device.) This bonding method is intended to bond the Au on the heatsink and the Au on the diode to the indium, forming an alloy

We mount these diodes into the holder and install the leaf springs on the holder to apply pressure of approximately 10KPa to the diodes when heating to prevent void formation and, as in adhesives; static pressure lowers the free energy and forces the bonding to occur.

We then place the holder on the resistive heating element of a custom annealing chamber. This chamber has a roughing pump to get the pressure down to 10^{-3} mTorr. Once there, we will start a flow of H_2 in order to prevent oxidation. The flow rate found to yield the best control over temperature was 2.6 Standard Litres Per Minute (SLPM.) A thermocouple is mounted to the heating element holder and the temperature is controlled by changing the current with a rotary dial. For the In, we are attempting to go for a low temperature solid-liquid-solid bonding process. This happens when the temperature is above $157^\circ C$. Given uncertainty in the exact temperature of $\pm 5^\circ C$ caused us to raise the annealing temperature to $170^\circ C$ for our process. Timing was performed by visual inspection of the surface of the In. When the In on the surface of the heatsink, adjacent to the diode alloys with the underlying Au you can see the In become shiny then take on a golden hue. This is a sign that $AuIn_2$ has formed. Once we saw this, we waited 60 seconds for the bond to form fully with the diode then turned the power down and allowed the devices to cool in the H_2 flow down to $90^\circ C$ and then flow N_2 until the temperature reads $40^\circ C$ in order to prevent excessive oxidation.

The Au-Sn bonding technique is more difficult than the In one. The main reason for this is that the Au cannot be easily thermally evaporated so we needed an e-beam source to evaporate the Au.

This is not available in the Edwards 360 so we had to switch to the Sloan Pak-8 Evaporator, known as the NRC Evaporator. The NRC Evaporator is a larger evaporator with the ability to use two separate thermal and two separate e-beam sources. While the basics with regard to the process, rate measurements and loading/unloading are nearly the same as

on the Edwards 360, the process is more involved. The instructions can be found in Appendix C. We first thermally deposit 5000Å of Sn on the heatsinks. While Sn will bond directly to the Au of the p-side of the laser diode, it will also readily form SnO that will prevent formation of the AuSn eutectics that we need. In order to prevent this from happening we will also deposit 250 Å Au on the surface of the Sn. Since the Au and Sn are in intimate contact, AuSn₂ alloys start to form immediately by the diffusion reaction, preventing oxidation and preparing the heatsink for mounting diodes.

We then mount the diodes on the heatsinks in our holder in the same manner as with the In and place the holder on the resistive heating element of the annealer. We pump down, flow the H₂ at 2.6 SLPM then raise the heat to 305°C. We chose 305°C instead of 280°C since we were concerned with the heat gradients between the thermocouple and the actual diode. Going over 280 °C will not affect the alloying and we could go as high as 309°C before forming unwanted peritectic tin-rich alloys. We were able to observe the same color change as with the AuIn bond as a measure of reaction after approximately 2 min. After early testing however we increased this time to 5 min. as there were large areas of the diode that were not bonded. After the time expired, we turned off the power to the heating element and allowed the devices to cool in the H₂ ambient down to 90°C, then cooled under N₂ ambient until 40°C then removed the devices.

4.4.3 Experimental Results

We tested a series of AlGaAs/GaAs laser diodes produced by Professor J. J. Coleman's group at UIUC. The basic structure of these devices is simply a stripe laser in a buried double heterostructure configuration. Each growth yields a wafer with uniform coating on it. These devices are coated with the p-layer and then cleaved to the desired length resulting in strips of 10 laser diodes each which are again cleaved to form individual diodes. These devices are tested on an Agilent Parametric Analyzer which sweeps current and measures the output power. This data is then collected and, by measuring the slope of the output power to the drive current, we get a value of the differential quantum efficiency. Additionally, by tracing the slope back to the x-axis we get the value of threshold current. These two values are typically used to measure the quality of the devices.

Our first trial with $\sim 20,000 \text{ \AA}$ was a failure. Once bonding was performed, we took the cooled devices and moved to testing, prior to running the power analysis, we decided to mimic the MIL STD testing for bonding by pushing on the facet of the laser diode with tweezers. In every one of the five cases the diodes fell off with a minimum of pressure applied. We assumed that there was insufficient pressure applied by the original arms on the process mount so we decided to apply stiffer leaf springs and run again. Upon inspection it became clear that the 5 diodes we used still had intact Au mounting surfaces so we just cleaned them and reused them on 5 new heatsink blocks. After processing, we attempted to press on the facets and, while there was minimally improved adhesion, all five laser diodes fell off.

We were not able to determine the cause of failure at that time so we moved to a more stable Au-Sn bonding process. Later, after reexamination of the problem, we realized that the formation of InO on the surface of the evaporated In was preventing bonding from occurring.

With the Edwards 360 evaporator we did not have the ability to evaporate Au so it wasn't revisited prior to changing to AuSn. There was no pressing reason to go back after we started the new runs so this topic was dropped.

Our initial failure with the AuIn system shifted us to the AuSn bonding method. We used the same evaluation method and success criteria as on the AuIn technique. For this testing we ran through a series of 47 separate devices mounted to the heatsink blocks. The measured values for the laser diodes threshold current (mA,) and quantum efficiency (%,) before and after appear in table 4.4. It should be noted, the testing of these devices didn't happen in sequential order.

Growth Run	device #	Efficiency Before %	Efficiency After %	Threshold Before (mA)	Threshold After (mA)	Result
S8072209	1	28	32	193.6	180.1	
S8072209	2	27	28	186.8	186.8	
S8072209	3	28	31	152.2	136.5	
S8072209	4	23	29	162.4	159.6	

S8072209	5	20	31	188.5	165.2	
S8072209	6	27	29	145.9	147.3	
S8072209	7	28	26	156.5	155.2	Tilted
S8072209	8	16	14	158	152.1	Tilted
S8072209	9	21	22	165	169.2	
S8072209	10	29		165.2		failed to bond
S8072209	11	27		147.9		failed to bond
S8072209	12	30		163.8		failed to bond
S8072209	13	31		156.4		failed to bond
S8072209	14	31		152.8		failed to bond
S8072209	15	31		154.6		failed to bond
S8072209	16	28		147.5		failed to bond
S8072209	17	29		145.7		failed to bond
S8072209	18	27		167.4		failed to bond
S8072209	19	33		135.4		failed to bond
S8072209	20	33	35	142.2	132.7	
S8072209	21	33	35	138.2	140.6	
S8072209	22	33	35	135.4	138.8	

S8072209	23	33	27.5	145	135.1	tilted
S8072209	24	33	34.5	169.5	149.9	
S8073108	25	33	33.7	177.5	163	
S8073108	26	28.95	31.2	169.4	153.2	
S8073108	27	29.68	34.1	166.1	145.1	
S8073108	28	29.76	24	163.11	155.3	Tilted
S8073108	29	30.38	30.7	163.5	150.2	
S8073111 A	30	27.31	25.7	190.2	172.53	Tilted
S8073111 A	31	18	35	134.8	136.3	
S8073111 A	32	33	32.5	144.3	155.8	Poor bond
S8073111 A	33	36	33	147.7	148.7	Failed Bond
S8073111 A	34	33	30	160	154.9	Tilted
S8073111 A	35	32	32	207.7	144.4	
S8073111 A	36	32	32	149.6	155.8	
S8073111 A	37	32	31	150.2	152.7	
S8073111 A	40	28	29	152	150.6	
S8073111 A	41	24	20	148.3	169.3	Poor bond
S8073111	44	21.6	30	253.92	203.1	

A						
S8073111 A	45	35.2	36	165.8	165.5	
S8073111 A	47	29.94	28	162.8	160.2	
S8073111 A	38	33		138.4		failed
S8073111 A	39	34		152.3		Failed
S8073111 A	42	22	28	162.5	158.7	
S8073111 A	43	14	16	152	143.9	Unevenly set
S8073111 A	46					failed

Table 4.4 Bond Testing Results.

It is immediately clear that the predominant result from this bonding is an increase in the measured quantum efficiency, compared to bonding with the Ag particle filled epoxy, and a decrease in the threshold current. These combine to give us devices that will be higher power and longer lifetime than the traditionally bonded devices. It will also reduce a factor in the uncertainty of the device testing. By reducing the variability in the series resistance and capacitance values of the bonding part of the laser diode package we will better be able to diagnose growth or design issues.

There are several diodes that do not have test data. In the note sections you will see that some devices failed, meaning they did not function for final testing due to some undiagnosed issue, or that they didn't bond. Devices 10-19 were a set of devices that we decided to perform the bond strength testing prior to optoelectronic testing and were the first set of diodes we tested. We will cover those results first, then move on to the functioning devices.

We wished to show the mechanical as well as electrical benefits to this bonding process by mimicking the bond strength testing covered in MIL STD 883C [50]. We were not able to solder pull leads to the laser diode for testing so we opted to evaluate the bond strength by a shear test. To perform this test we applied a pressure, measured with a pull test gauge, to the face of the laser diode. The pull gauge measured the pounds of force so we took that, divided it by the surface area of the diode, and came up with a value for testing. We used 200 PSI as the test value then applied this force to each diode. Unfortunately, for each of these 10 diodes, the bond failed. Upon inspection we saw that there was a partial bond where portions of the diode cladding were still attached to the heatsink block.

We further inspected device #10 in an SEM taking an image of the surface of the bond right where the bonded and failed bond meet and is seen in Figure 4-3.

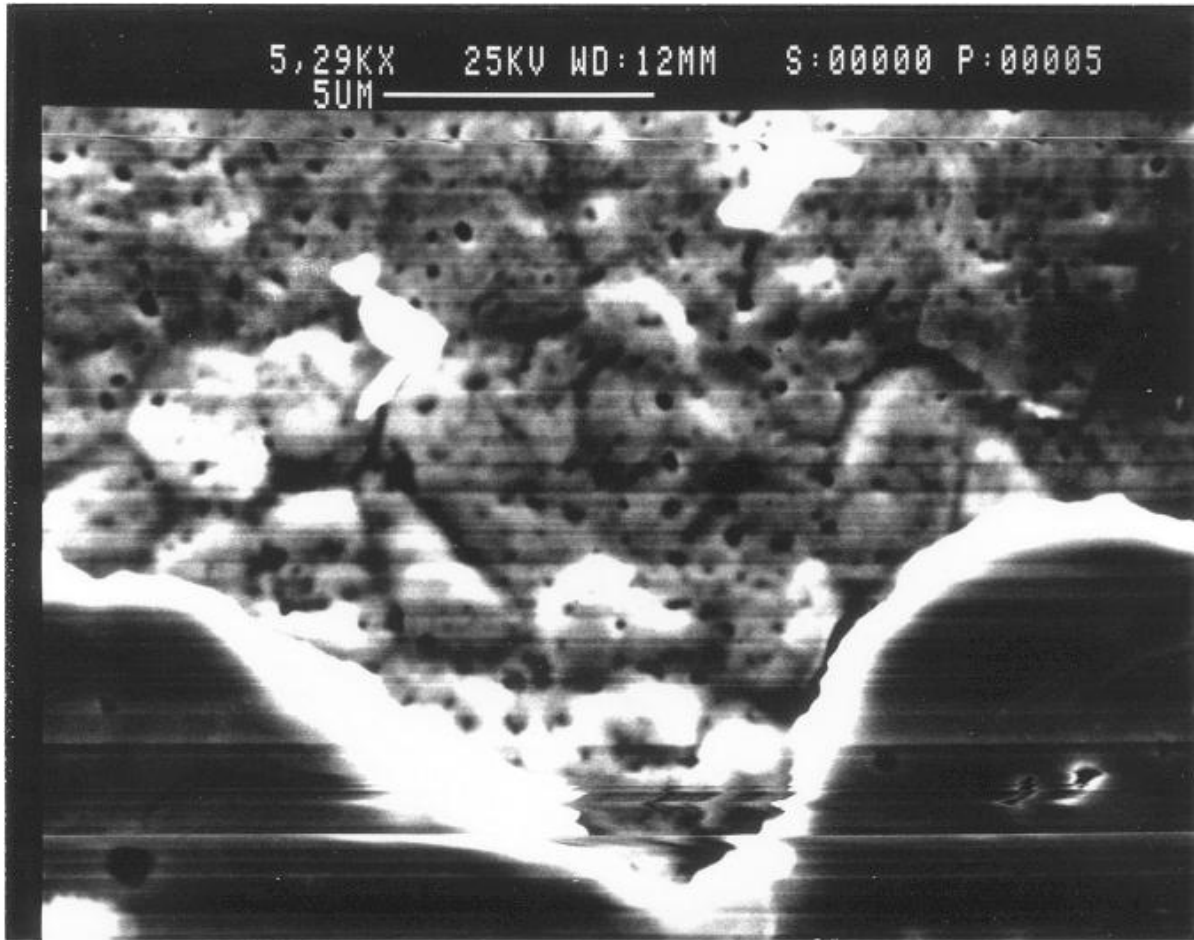


Figure 4-3 SEM Image of Failed Bond on device #10.

What we see is the flat, bonded AuSn layer and a rough incomplete bond. We believe there are two possibilities. First, it is possible that we did not apply sufficient pressure to the device during bonding. Since the free energy of the Au and the AuSn lattices is high, it can force the molten Sn to migrate away from the bond leaving Sn rich morphology, which appears exactly like the rough portion of our image. Second, it is possible that we simply didn't give the solid liquid diffusion process to completely react across the device face leaving the bond only partially formed. To address these concerns we added stiffer leaf springs to raise the pressure applied from ~10KPa to 20KPa as increased pressure lowers the free energy of the surface preventing migration. We also increased the bonding time to 5 min. to ensure complete alloying of the surface.

The next round of trials proceeded smoothly. Most of the devices experienced an increase in the Quantum efficiency and a decrease in the threshold current. The results for the change in quantum efficiency are plotted in Figure 4-4 and Change in threshold in Figure 4-5.

In Figure 4.4 the Mean increase is seen to be 1.47 with a standard deviation of 4.4. This isn't that high a value, but when we take a closer look at some of the numbers for the different devices we see that there are several where the performance of the device went down. Likewise, when we take a look at the change in threshold current we see the mean decrease in threshold current was 8.1mA with a standard deviation of 15.37. But this also represents devices that appear to be incorrectly bonded or damaged.

Upon investigation there were several devices that exhibited either a reduced efficiency, an increased threshold or both. We selected the diode 41 as the first device to

examine as it exhibited a decrease in efficiency and an increase in threshold. Visual inspection revealed that the surface of the diode was slightly tilted in regards to the surface of the heatsink.

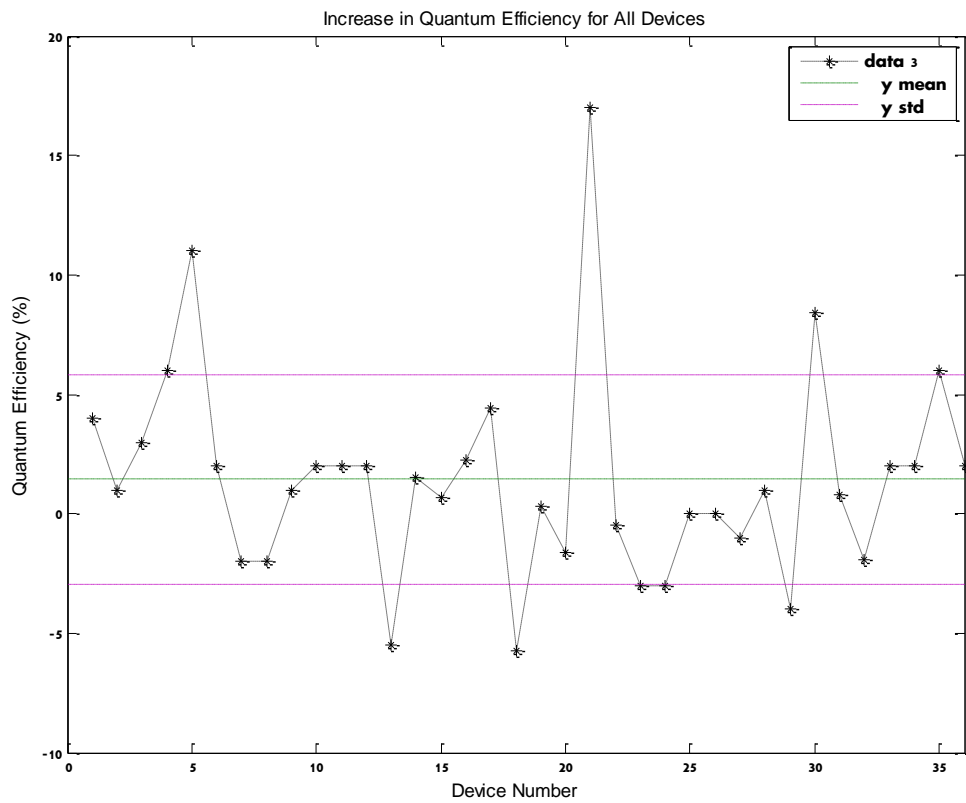


Figure 4-4 Change in Quantum Efficiency for Laser Diodes

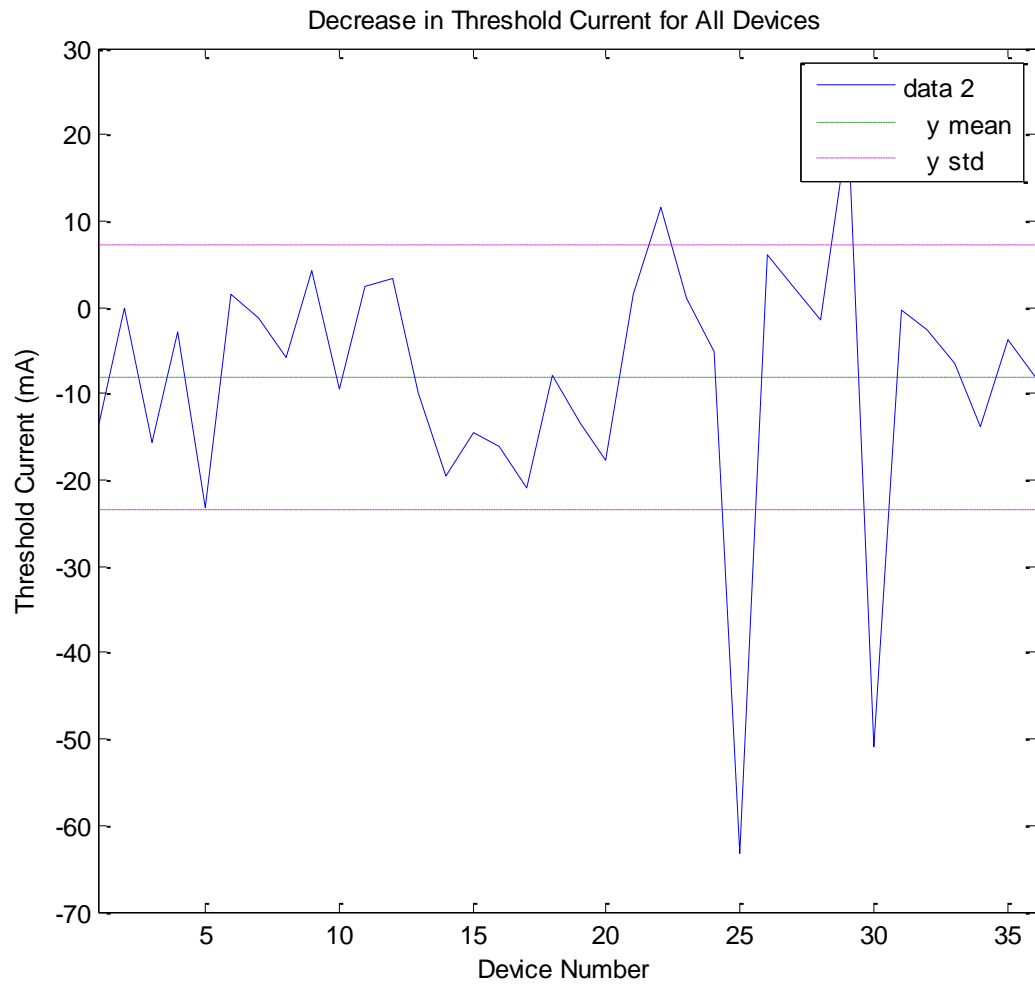


Figure 4-5 Decrease in Threshold Current for Laser Diodes



Figure 4-6 SEM Image of Failed Device #41

When we tested the bond strength, the device failed and exhibited much the same bonding failure as the earlier devices as seen in Figure 4-6. While the bond wasn't complete, it appears that the surface of the failed bond is much smoother implying that there was a partial bond that simply had too many voids. We surmised that this was due to the leaf spring on the mount not being fully centered.

If the diode is tilted slightly, it will not bond uniformly and will exhibit reduced efficiency and possibly increased threshold current due to current crowding effects caused by reduced contact area.

While the bond issues seem to explain the reduced efficiency and increased threshold, there is a number of devices that are slightly tilted, pass the pressure test, but have a reduced efficiency. Mainly device numbers 7, 8, 23, 28, 30, 34 and 37. All of these devices have a reduced threshold as well. Two possibilities are the tilt in the diode prevents power from the diode from being effectively detected by the measurement cone, or current isn't effectively flowing through the laser stripe but is getting through the barrier materials. Both of these would result in a reduced efficiency, but the test setup does have a tip/tilt stage to account for this so we believe the first explanation is probable. Either way, both of these issues can be resolved by ensuring the leaf springs are applying uniform pressure normal to the surface of the heatsink.

A final class of device changes are the ones that had a huge increase in quantum efficiency, but also had an increase in threshold current such as device 31. I believe the reason for this is poor bonding on the initial testing of this device prevented the current from effectively flowing through the device. So, while a minor increase in threshold current, less than 2%, resulted, it achieved nearly a 50% increase in efficiency.

Our testing ended before we could implement full controls over a new run of devices so we weren't able to effectively test our conclusions fully.

As a theoretical measure, we decided to represent the increase in efficiency and decrease in threshold current as if we correctly processed the devices by removing from the data, all devices that were determined to have failed due to errors in processing. We present this data in figures 4-7 and 4-8.

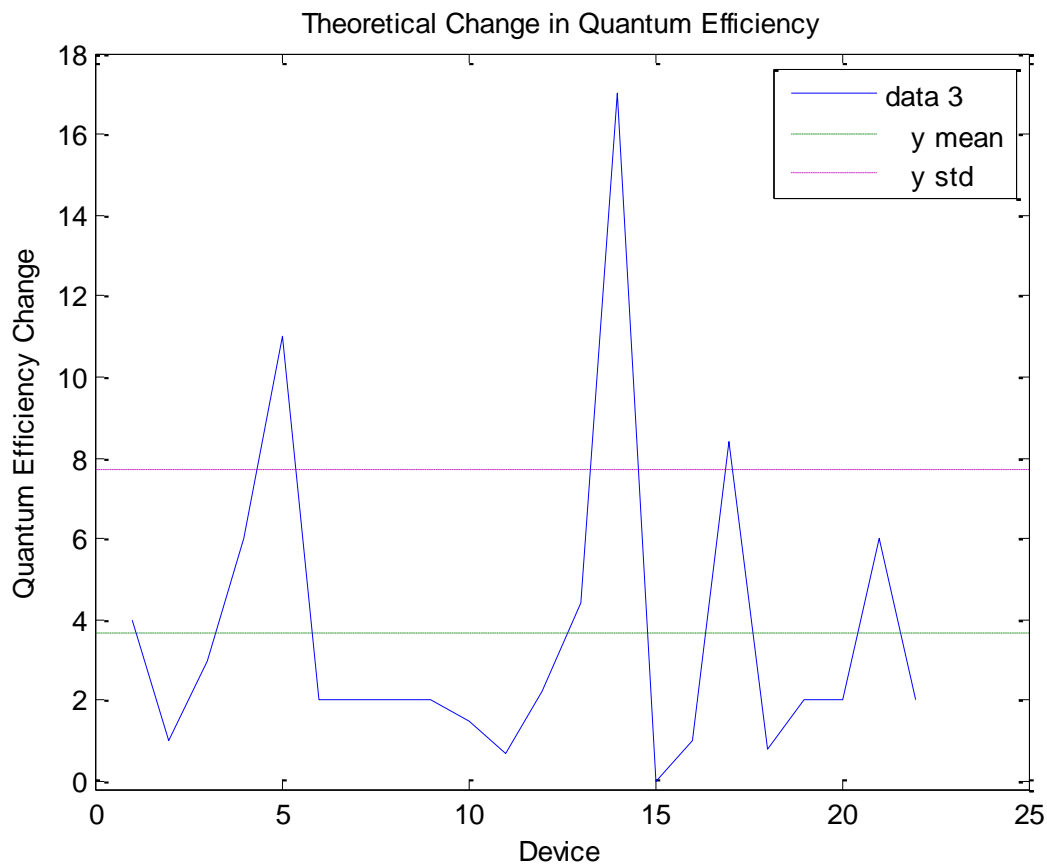


Figure 4-7 Theoretical Increase in Quantum Efficiency by Utilizing New Bonding Process.

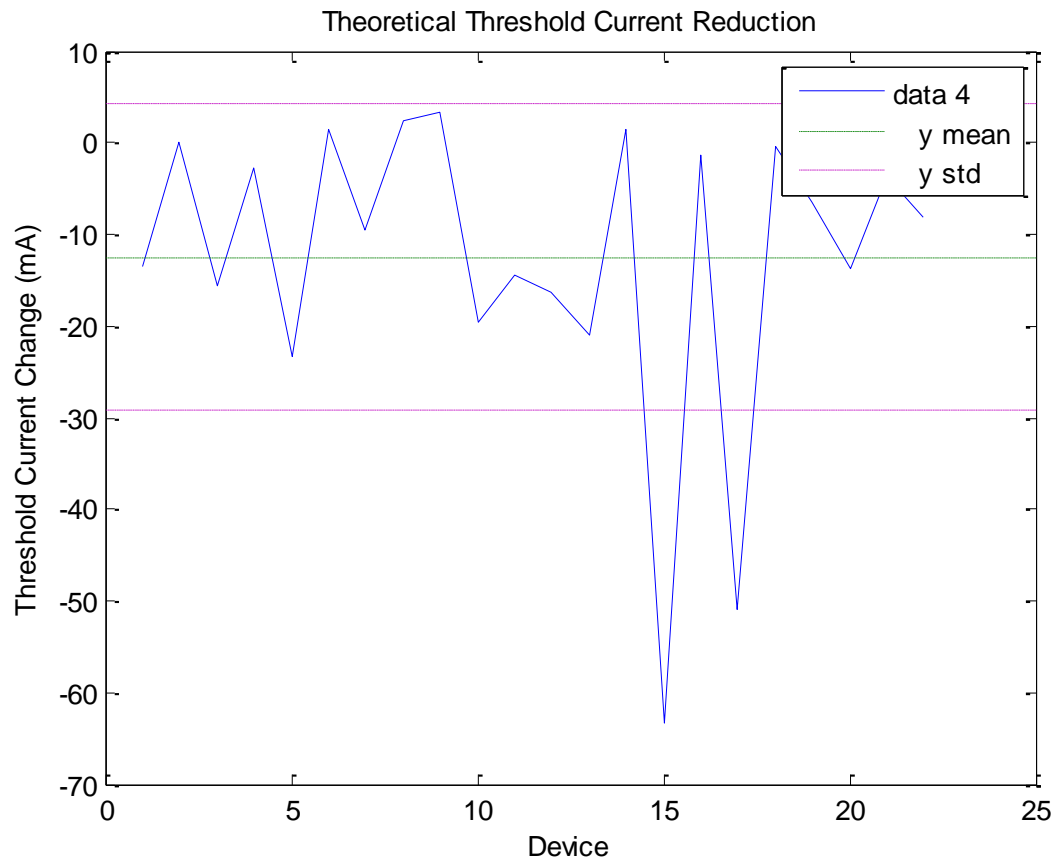


Figure 4-8 Theoretical Decrease in Threshold Current

Utilizing this methodology, we realize an 8% decrease in the threshold current and a 13% increase in the quantum efficiency. While these numbers aren't huge, it does show the utility of this process.

4.5 Conclusion

The need to develop a consistent, controllable bonding process drove us to investigate the use of hard solder bonding methods to replace the epoxy methods that had been used. We found two promising techniques, AuIn and AuSn and began testing. We determined there were several considerations that needed to be addressed and that the AuSn process was the optimal technique for our devices. After several test runs, we optimized our process and determined that, given good process control, our bonding technique would increase device efficiency 13% while reducing threshold current by 8%. This process is now fully developed and it is our hope that it can be utilized in future devices.

CHAPTER V

CHARACTERIZATION OF III-NITRIDES BY SPECTROSCOPIC

ELLIPSOMETRY

5.1 Introduction

Spectroscopic Ellipsometry has long been used to characterize the optical properties of transparent bulk materials or thin absorbing layers. Its initial use by Paul Drude in the 19th century was to simply characterize the optical constants of a number of metals by measuring the polarization change in the reflected light [64]. This was primarily the extent of the uses for this technology until the advent of the microcomputer. Once computing power became available in the 60's to the 70's groups were able to control the ellipsometers to gather more information than before. Many of the early improvements were presented by Aspnes et al. [65] and further expanded on by Palik et al. in their exhaustive study of optical constants [66]. These works heralded the beginning of a new phase of ellipsometry where the use of a variety of polarization techniques, light sources, variable angle spectroscopy and the implementation of more effective analysis techniques opened the door to its use by everyone. Today, Spectroscopic Ellipsometry is widely used to not only characterize optical constants of simple layers, but to evaluate the complete optical properties of complex, multilayered structures requiring an array of measurements. Spectroscopic Ellipsometry is not employed ex-situ as a research and quality control technique and in-situ to accurately control the growth process for the semiconductor growth industry.

It continues to be a simple, non-destructive technique that can easily be automated to provide real time control of the semiconductor growth process. Our interest is that it can quickly and accurately determine the optical constants and crystalline properties of the III-Nitrides quickly down to the Å thickness scale. While there are a multitude of measurements we can get from this technique, our primary interest is in the simple determination of the refractive indices for their use in design considerations for optoelectronic devices and in the determination of Al% in the AlGaN material. We will briefly cover the theory behind spectroscopic ellipsometry then move on to our experimental determinations.

5.2 Background

While there are many complex steps involved in the accurate determination of optical constants, ellipsometry at its most basic is simply the determination of the change in polarization after reflection from a substrate, by measuring the complex ratio of s-polarized light to p-polarized light and is represented in equation 40:

$$\tan \Psi \cdot e^{i\Delta} = \rho = \frac{r_p}{r_s} = \tan \Psi (\cos \Delta + i \sin \Delta); \quad (40)$$

With standard spectroscopic ellipsometry this data is captured at a range of wavelengths usually up to the material transparency (UV.) If this material were a bulk, isotropic material we could simply invert the equation to get the relations to the optical constants, however for graded layers or materials with surface layers or oxides we need an additional data point. If we also collect the spectroscopic data at a range of incident angles we can now account for these layers. And, upon inversion, we can get the optical constants as in equation 41:

$$\langle \varepsilon \rangle = \langle \varepsilon_1 \rangle + i \langle \varepsilon_2 \rangle = \langle \tilde{n} \rangle^2 = (\langle n \rangle + i \langle k \rangle)^2 = \sin^2 \phi \left[1 + \tan^2 \phi \left(\frac{1 - \rho}{1 + \rho} \right)^2 \right]; \quad (41)$$

Where ε represents the dielectric function of the material, n and k are the refractive indices and ϕ and ρ are as before. While mathematically this formula clearly shows collection of the optical constants simply by inversion, in real life this isn't that simple. Actual materials have a number of inhomogeneities, surface features and voids that would give inaccurate data should we attempt to invert ρ directly. As a measure of the variations that can impact our measurements, at angles of Δ close to 180° the sensitivity for some materials is high enough that we can measure thickness variations down to the \AA scale [67]. We need a method that can handle the multitude of variations that are present in real materials.

Early pioneers such as Cauchy and Sellmeier developed good models of the behavior of the dielectric functions and refractive indices of materials. These early models work well in the transparent region of the material and have been used to model the behavior of materials for over a century. We see Cauchy's formula in equation 42 and Sellmeier's in 43. Cauchy's formula is older, 1836 versus 1871, but Sellmeier's is more accurate.

$$n(\lambda) = A + \frac{B}{\lambda^2} + \frac{C}{\lambda^4} + \dots \quad (42)$$

Where A, B and C are determined by fitting parameters. And Sellmeier's:

$$n^2(\lambda) = A + B + \frac{\lambda^2}{\lambda^2 - \lambda_0^2} \quad (43)$$

Where λ_0 is the resonance wavelength for which the refractive index diverges. Now that we have the equations that we can use to model the material behavior we look at the process necessary. As mentioned before, while we can invert Ψ and Δ to directly calculate the optical constants and dispersion formula, this value will not be accurate. We will employ a regression based analysis to come up with more accurate models for our process. The simple flowchart example appears in figure 5-1.

With all regression based solvers you simply make estimations then take those values to improve on the accuracy of the measured values and models. With SE we start by measuring Ψ and Δ . We then develop a basic model based on simple Fresnel equations to estimate simple thicknesses, or Cauchy or Sellmeier equations for more complex structures. We calculate the expected results based on this new model and evaluate the accuracy of these results most commonly, for SE, with the Marquardt-Levenberg algorithm for determining the Mean Squared Error or MSE [68,69]:

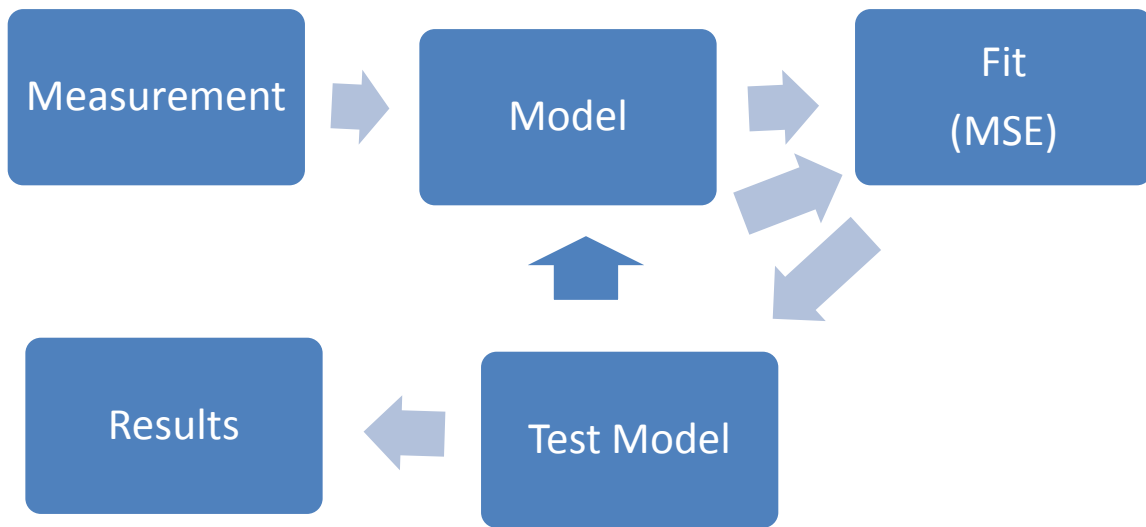


Figure 5-1 Flowchart for Spectroscopic Ellipsometry

$$MSE = \sqrt{\frac{1}{2N-M} \sum_{i=1}^N \left[\left(\frac{\Psi_i^{Mod} - \Psi_i^{Exp}}{\sigma_{\Psi_j}^{Exp}} \right)^2 + \left(\frac{\Delta_i^{Mod} - \Delta_i^{Exp}}{\sigma_{\Delta_j}^{Exp}} \right)^2 \right]} \quad (44)$$

An MSE closer to 0 is optimal, but good fitting results can be had if you get close to 1. Ideally, either simple Fresnel or Sellmeier equations gave good results for fitting but this is seldom the case as they have a problem dealing with anisotropy and they were only good in the transparent range of the spectra so metals and semiconductors could not be effectively modeled . There has been much work in the past few years on addressing this limitation. If you treat the behavior of Ψ and Δ as being due to fluctuations in the dielectric constant, you can easily model the material as a linear system of oscillators of varying strengths and couplings to get the dispersion relation of the material. These oscillators are easily modeled as Gaussian or Lorentzian or can be a combination of the two. Additionally, a number of different oscillator models have been developed to address the varying materials. Some of these appear in table 5-1 [71].

Dispersion Formula	Materials Family	Materials Examples
Lorentz Oscillator	Transparent and weakly absorbing dielectrics	Oxides (SiO ₂ , SiON, Al ₂ O ₃ , MgO, ZrO ₂ ,) and polymers
Drude Oscillator	Metals	Al, Ag, Cr, Cu, Ti
New Amorphous Tauc Lorentz	Semi-absorbing dielectrics and semiconductors	SiN, a-C, oxides (TiO ₂ , Ta ₂ O ₅ , ZnO,.) AlN, photoresist
Kato-Adachi Adachi-New Forouhi	Crystalline Semiconductors	InP, InAs, AlGaIn, InGaP, AlInP, InGaAsP

Table 5-1 Examples of model applications for specific materials

The final important part in accurately modeling the material you are analyzing is having an as accurate as possible optical model of the material we are investigating. Real materials not only have the bulk layers of isotropic material, but also have interfacial mixing, surface roughness, crystalline defects, voids and compositional grading.

All of these need to be accounted for in order to get good values on the optical constants. Recall that a properly chosen angle of incidence, one where Δ is as close to 90° as possible, will allow for sub-nanometer resolution in the thickness measurements [67], so even the thinnest layers can have an impact on the measurements. The growth process will determine what types of modeling layers you will need. For instance, we are using MBE and MOCVD processes, both of which have a high level of control over the abruptness of each layer and compositional isotropy across the layer. For example, on our materials which are a layer of AlGa_xN on Al₂O₃ with a thin AlN buffer layer we use the following (Figure 5-1.)

10nm thick Al _x Ga _{1-x} N/ void layer.
640 nm Al _x Ga _{1-x} N Layer
25nm AlN buffer layer
Al ₂ O ₃ Substrate

Figure 5-1 Simple model for determination of Al_xGa_{1-x}N optical constants

If we were to use other techniques which inadvertently or intentionally, resulted in inhomogeneous growth, we would want to use interfacial mixing layers such as the model we used for one of our samples that has a layer of 34% Al sandwiched between 43% Al layers. Since the percent Al is difficult to control when switching from one layer to the next, we have an interfacial mixing layer which we model by using a layer of 34% Al mixed with 43% Al (Figure 5-2.)

10nm thick $\text{Al}_x\text{Ga}_{1-x}\text{N}$ / void layer.
100 nm $\text{Al}_{0.43}\text{Ga}_{0.57}\text{N}$ Layer
25 nm $\text{Al}_{0.43}\text{Ga}_{0.57}\text{N}$ / $\text{Al}_{0.34}\text{Ga}_{0.66}\text{N}$ Layer
100 nm $\text{Al}_{0.34}\text{Ga}_{0.66}\text{N}$ Layer
25 nm $\text{Al}_{0.43}\text{Ga}_{0.57}\text{N}$ / $\text{Al}_{0.34}\text{Ga}_{0.66}\text{N}$ Layer
200 nm $\text{Al}_{0.43}\text{Ga}_{0.57}\text{N}$ Layer
25nm AlN buffer layer
Al_2O_3 Substrate

Figure 5-2 More complex model employing interfacial mixing layers.

These are just some of the possibilities with SE. If it is combined with variable angles of incidence, there is no limit to the number of layers of transparent or semi-absorbing materials that we can characterize. Because SE is non-contact and requires just the use of monochromatic light it is easily mounted in-situ for most semiconductor processes. This ensures that it will continue to expand as a characterization technology. We will now cover the experimental setup.

5.3 Experimental Setup and Results

5.3.1 Introduction

While there are a number of material characteristics that can be determined using Variable Angle Spectroscopic Ellipsometry (VASE,) such as optical constants, strain values, crystalline quality, grading, composition, thickness and many other too numerous to list, we are initially interested in the dispersion formula for the refractive index. The refractive index is important for us since we will use this value to determine the optimum dimensions for our UV laser diodes. We need to know values such as facet reflectivity, optical confinement and effective cavity length in order to know how to make the proper devices, and the refractive index needs to be known to calculate these. As a secondary interest, we are also interested in novel determination of the percentage of Al in the material.

We can do this by checking what the static dielectric constant is for the sample. Since it is a value we already have we will use it.

5.3.2 Experimental Setup

Our measurements were carried out on the Horiba-Jobin Yvon UVISSEL variable angle spectroscopic ellipsometer located in the Center for Nanoscale Materials at Argonne National Laboratory. This spectrometer utilizes a Hg arc lamp to provide illumination from the UV to the near IR. This light is passed through a polarizer, then a monochromator and is directed to the substrate mounted on a motorized stage. The reflected light is then passed through the polarization selective analyzer and on to the detector. The light source and detector stages are mounted on arms that are motorized to allow for variable angle of incidence and detection. The whole setup is controlled by the DeltaPsi 2 software loaded on the desktop controller. The software controller, combined with fully automated stage, light source and detector allows for fully automated scanning and characterization of large wafers up to 4 in. in diameter. Mapping of a wafer is a highly useful process step for the semiconductor industry and is one of the more common applications for this equipment.

Once the spectroscopic data is collected it is saved by the control software in an acquisition file. This file is saved for use in the modeling process where we compare the experimental Ψ and Δ to the theoretical model to determine our MSE. The software is very simple to use and simply requires the input of a good optical model coupled with the proper selection of oscillator functions to provide a good fit to the experimental data.

We ran a series of various samples, primarily thick AlGaIn layers of varying Al concentrations, over the course of several months. These samples were run using a spectral range from 0.5 eV to 6 eV to cover from transparency up to the absorbent range. In earlier

testing we found that from 68° to 72° were the optimal Angles of Incidence (AOI,) to use for these materials. Once the spectra were collected we employed the regression analysis steps to develop the best fit models. From these models, we were able to collect a series of dispersion relations for the various concentrations which we report in the results section. Also, since it is automatically collected with the spectra, we show the static dielectric constant.

5.3.3 Experimental Results

Using the regression based modeling process we were able to consistently get good fitting results for all of our different samples and the layers within those samples. Our average MSE was 1.9 with some values as low as 0.39 while the highest was 7.9. While that particular sample was suspect, we used it anyway. We have plotted the various results averaged over our sample set for the AI% values from 0% to 96% in Figure 5-3. We believe that, in some of our the samples, the NCI based material served to distort the smooth progression from the value of n at infinity to the bandedge. Also, there is a great deal of distortion as the material becomes absorbing so we continued the plot as a linear function through that portion of the spectra. This will not affect us as the emission wavelength for these devices is redshifted from the bandedge.

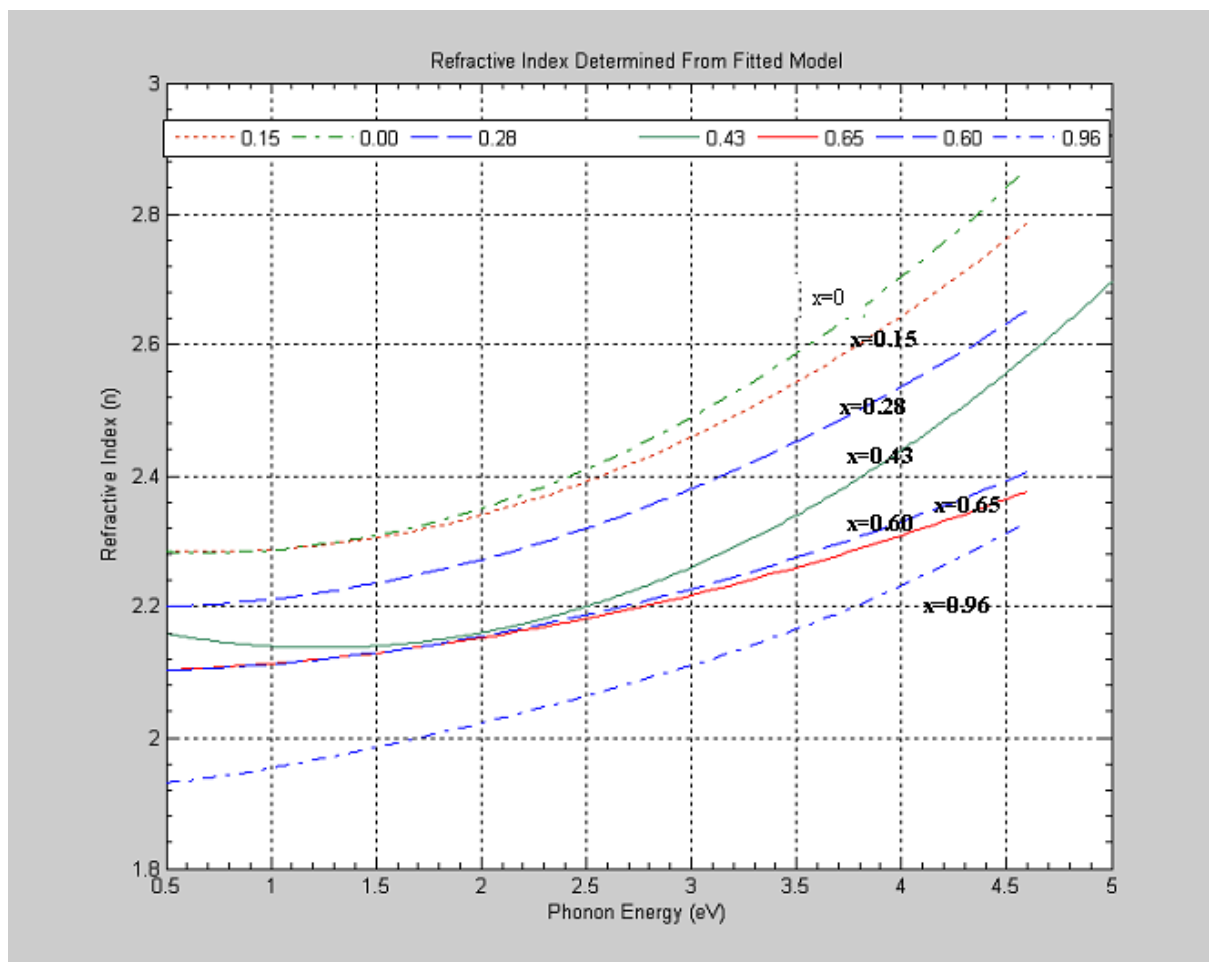


Figure 5-3 Refractive Index for Varying Al% in AlGaIn from the IR to UV

When we compare our results to other groups that have tested similar materials we found that our results are in good agreement with theirs [69,70,77,78], for the samples with $Al\% < 70$. We did find that our 96% Al sample had a slightly lower value than found by Brunner et al. [77], but this is most likely due to defects in the as grown material as the Al% gets closer to 100.

In addition to the refractive index determination, we used the VASE experimental data to get the dielectric constants for the different materials. It turns out, that a method similar to what was reported on by Lee et al. [72], we can determine the Al% in AlGa_N by measuring the dielectric constant. We have plotted these values in Figure 5-4:

As can be seen, we have a decrease in dielectric constant which is close to being linear. Our data shows a lower dielectric constant than originally reported by Collins et al. [73], but is in line with later reporting by Goldberg et al. [74]. This gives us the following relation for the dielectric constant variation with respect to percent Al:

$$Al_x = 4.4 * \epsilon_s^2 - 46 * \epsilon_s + 120 \quad (45)$$

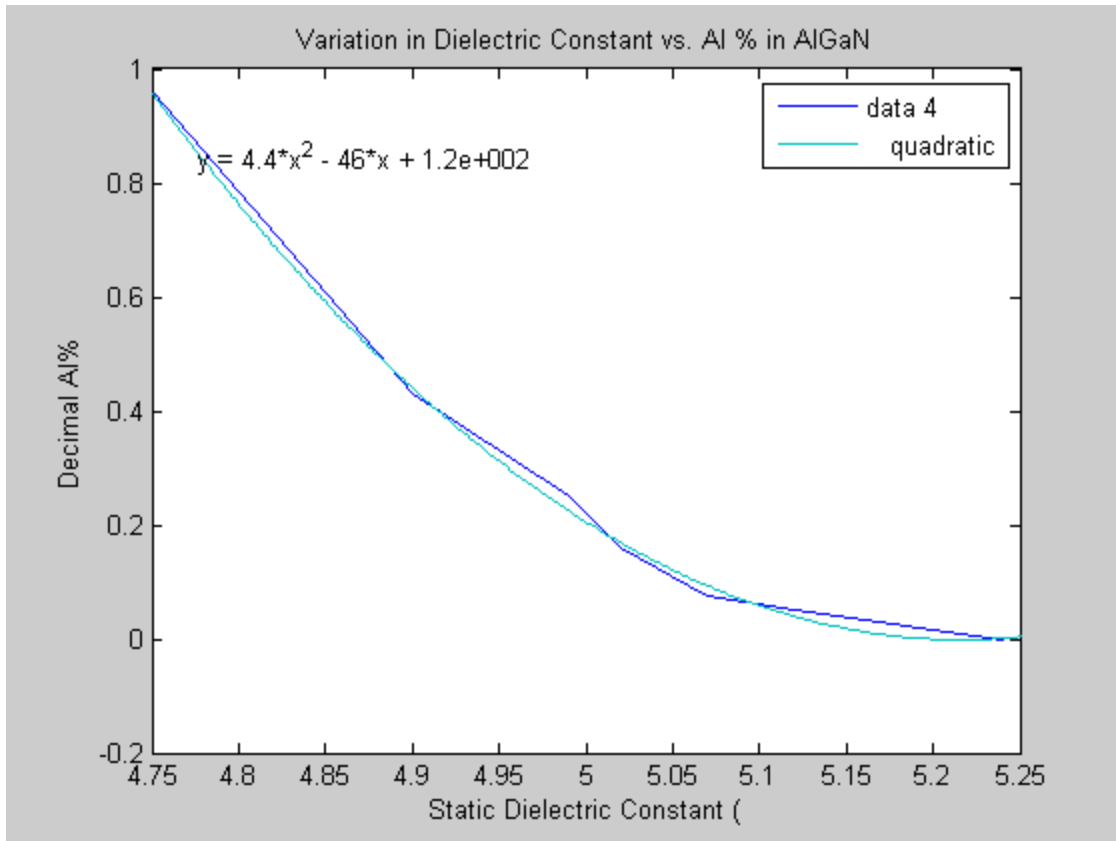


Figure 5-4 Plot of Change in Dielectric Constant per percent Al.

5.4 Conclusion

Variable Angle Spectroscopic Ellipsometry has shown to be a continuously improving analytical technique that will continue to be at the forefront of processing technologies and characterization. It's simple, non-destructive and highly flexible capabilities were one of the reasons we chose to implement this analysis as opposed to techniques such as prism coupling. We have effectively employed this technology to determine the refractive index for the materials we are studying and also employed it as another manner in which to determine the composition of these samples. It is expected that VASE will be useful in many other future areas of measurement and investigations.

APPENDICES

APPENDIX A

A.1 Introduction

This appendix will cover the necessary process steps that we used to prepare the samples for processing. This will include the pre-deposition cleaning, oxide deposition, photolithographic processing, cleaning prior to plasma etch, and final stripping after the etch was performed. All of these tasks were performed in the Army Research Laboratory in Adelphi Maryland.

A. Oxide deposition

Silicon Dioxide is very useful for our device processing as it serves as a supplemental mask to the photoresist. SiO_2 is 9 times more resistant to the ICP etch process than the III-Nitride materials we are using [40]. It is easily and cheaply deposited using a plasma deposition setup and is fully compatible with every step in our process. And, most importantly, BOE readily removes it without etching the III-Nitrides. For our devices we would deposit 3000 Angstrom on the grown material prior to processing. This layer is thick enough to provide protection to the device mesas without causing problems with the aspect ratio of the ridges to the trenches. If we were to go thinner, we may etch through the layer during etching and, were we to go thicker, we may have issues getting the necessary etch depth.

Prior to deposition we cleaned our samples using the standard RCA cleaning procedure in order to strip the organic and inorganic contaminants off the material. We then placed the

APPENDIX A (Continued)

samples on a sacrificial Si wafer and closed the chamber lid. We used a plasmatherm CVD chamber to deposit the oxide layer. The recipe was already loaded in the equipment so we simply had to put the desired thickness of oxide and press go. After deposition, we checked the oxide thickness on a simple ellipsometer. For successive runs, we used the color of the oxide to determine that the proper thickness was achieved. This chamber was also used for deposition of SiN layers for later experiments. The process was exactly the same except for the process gas used.

A.2 Photolithography

Photolithography is the process of using a photoreactive polymer, selectively exposed, to define features for etching, deposition or other process step. It is common to nearly every semiconductor device and is used for VLSI, thick film, thin film and nearly every other process that requires the definition of a structure. There are many different types of photoreactive chemicals that are used, but we will only cover the chemicals and processes that are used in our device fabrication.

The basic chemistry behind the photoresist we are using is simple enough. By exposing an organic polymer in solution to an Ultraviolet light source cross-linking occurs. The end result of this cross linking is to make the resist either more (positive) or less (negative) soluble in the respective developer.

APPENDIX A (Continued)

At this point we can either put the coated substrate in the developer and dissolve away the unwanted coating sections utilizing a positive photoresist process or we can subject the coating to another bake step and subsequent flood exposure of the coated area to utilize the negative photoresist process.

Our initial attempts were geared towards using a negative photoresist process. The reasoning for this was that the additional baking steps required resulted in a more robust polymer that was even more resistant to ICP etching. The process steps for a negative resist process are as follows:

- 1- Deposit 3000 angstroms of SiO₂ per the oxide procedure.
- 2- Clean surface with acetone.
- 3- Apply 2 drops Hexa-Methyl Di-Silizane (HMDS) an adhesion promoter.
- 4- Spin at 4000 RPM for 40 seconds.
- 5- Apply 2 drops of Photoresist type AZ 5214 made by Shipley.
- 6- Spin @4000 RPM for 40 seconds.
- 7- Soft bake @ 95° C for 150 Seconds to activate the polymer chains
- 8- Expose for 15 seconds with 7.4 MW/cm² (Or change time depending on lamp output) on a mask aligner loaded with the appropriate feature mask made of transparent chrome on quartz.

APPENDIX A (Continued)

- 9- Hard Bake @110° C for 135 seconds to harden the exposed cross-linked polymers.
- 10- Flood Expose for 30 seconds to lock in the exposed ones and make the unexposed ones ready to remove by developer.
- 11- Develop using a solution of 1:1 AF 312 Developer and DI water for 35 Seconds
- 12- Etch using BOE for 60 seconds to remove the oxide mask from the features you wish to remove.

After numerous trials it was determined that the negative photoresist process was too difficult to use. While it was more resistant to ICP etching, the additional exposures and bakes made it highly variable. We especially had difficulty with the alignment on the Suss (sp?) mask aligner resulting in poorly formed features. We determined that it would be easier to use a positive process so I remade the masks and ran the following process:

- 1- Deposit 3000 angstroms of SiO₂.
- 2- Clean surface with acetone.
- 3- Apply 2 drops Hexa-Methyl Di-Silizane (HMDS) an adhesion promoter.
- 4- Spin at 4000 RPM for 40 seconds.
- 5- Apply 2 drops of Photoresist type AZ 5214.
- 6- Spin @4000 RPM for 40 seconds.
- 7- Soft bake @ 95° C for 150 Seconds.

APPENDIX A (Continued)

- 8- Expose for 15 seconds with 7.4 MW/cm^2 using new positive photomasks.
- 9- Develop using 1:1 AF 312:DI water for 30 Seconds.
- 10- Etch using BOE for 60 Seconds.

Some of the issues that you will see with the positive resist processes are:

- Poor definition on the smaller features- This is caused by either not sufficient contact between the substrate and the mask causing poor definition or overdeveloping causing the smaller features to dissolve away.
- Poor adhesion of the developed resist- This is caused by too short a hard bake time, use a longer hard bake time.
- Incomplete trenches and pits- Lengthen the developing time

A.3 Removal of Photoresist

Initial trials of etching were run with the resist still on the oxide layer when we introduced the samples into the etch chamber. This is how devices had been run previously and we assumed that the additional layer would serve to protect the oxide layer further from the etch process making it more robust. It turns out that the oxide layer, given its high resistance to the Cl_2 based process we are using, is sufficient. Additionally, difficulties in ensuring all of the photoresist is removed by developer, especially when using small device features, leads to numerous issues on the etch. In fact, it was this failure to develop the resist

APPENDIX A (Continued)

that resulted in the extreme morphology exhibited in our first etch runs. For these reasons we needed to remove the photoresist. There are two methods commonly used for this process, one, is plasma ashing using O_2 as a source gas for the plasma and using the stripper called Piranha, a mixture of $H_2SO_4:H_2O_2$ prepared according to the following discussion.

While either method is acceptable for the removal of organic contaminants, we were concerned with the removal of inorganic contaminants. While RCA cleaning after plasma ashing will achieve this, we found the process was easier when just using piranha.

A.4 Preparation of Piranha Solution

Piranha solution is simply a name given to a highly active organic stripper. This stripper is a mix of the 3 parts concentrated sulfuric acid and 1 part hydrogen peroxide (30%). This is the solution that we use to strip off the photoresist after we're done ICP etching leaving just the oxide layer.

APPENDIX B

B.1 Introduction

The intention of this whole project was to design a new laser diode based on the AlGaIn/GaN QW material being grown for the SUVOS program in DARPA. Unfortunately, there were not sufficient masks or devices designed at the time which were suitable for materials characterization and device fabrication. To this end, we designed a series of masks to achieve two objectives. First, we needed to characterize the optical properties of the material, mainly optical gain. Second, using the data we collected, we needed to fabricate our UV laser diodes. I will cover the basics of device design for our Metal-Semiconductor-Metal (MSM,) devices then go into general detail on our laser diode device.

B.2 Metal Semiconductor Metal (MSM) Device

At the most basic level, laser diodes, and in fact all lasers, can be expressed as an active medium in a resonator that provides optical gain. We have the refractive index of our material from the Spectroscopic Ellipsometry we have performed, this will allow us to calculate the mirror reflectivity using the simple relation in equation 46:

$$R = \left(\frac{n_2 - n_1}{n_2 + n_1} \right)^2 ; \quad (46)$$

APPENDIX B (Continued)

Where n_1 and n_2 are the refractive indices of air and the AlGaN of the waveguide we are using. Now, in order to have lasing we need gain of more than the losses, we need to know the material gain in order to effectively model our resonators. While we could have used ellipsometry to get the absorption of the material by using equation 47:

$$\alpha = \frac{4\pi k}{\lambda} \quad (47)$$

Then estimated the gain with the theoretical concept that the value of gain at threshold exactly equals the loss [85], can simply be calculated using the following relation [87]:

$$\frac{1}{g_{Threshold}} = \frac{1}{\alpha} = (-L_{Cavity} \ln(R)) \quad (48)$$

Where $g_{Threshold}$ is the threshold gain of the material, the highest value, L_{cavity} , is the effective length of the cavity and R is the mirror reflectivity already calculated.

Unfortunately the effective length of the laser cavities is an issue with material such as the AlGaN we are using due to defects. For instance, even though we could use the measured length of the waveguide and the refractive index to get the expected optical length, this value will be off from the exact value due to the relatively high concentration of defects in the III-Nitrides. A better way to get a value for the absorption, and conversely the gain, would be to employ a variation on the Variable

APPENDIX B (Continued)

Stripe Length technique outlined by Shaklee and Lee [86]. This technique employs Beer's

law:

$$I = I_0(e^{-\alpha L}) \quad (49)$$

To get a value for the absorption by exciting the waveguide at one point and sampling the intensity at positions further down the waveguide at position L.

While this works well for thick layers of material, the thin waveguide structure we are dealing with on these devices makes it difficult to couple light into the face of the waveguide. We can however employ Metal Semiconductor Metal (MSM,) structures to do this. The MSM structure is designed to detect photoexcited carriers by effectively placing metal fingers on top of the substrate material that is tuned to the wavelength of interest. In our case, we would employ a mesa structure as seen in Figure B.1:

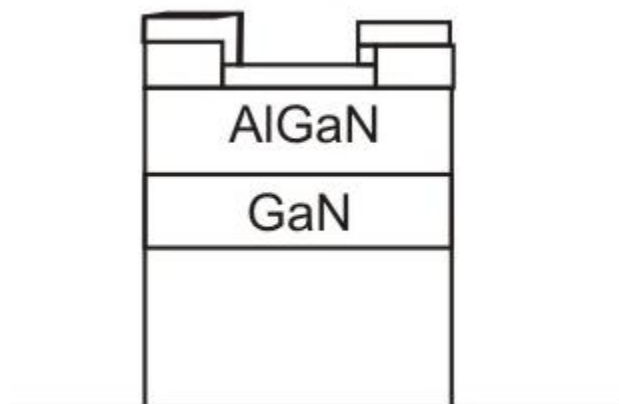
APPENDIX B (Continued)

Figure B.1 MSM fingers on top of AlGaN layer

The main consideration that determines the sensitivity of the MSM device is getting the electrical contacts close enough to the photoexcited carriers to detect them. This is done by ensuring the contacts are within the diffusion length distance for the carriers we want to detect. The rough estimate for AlGaN is 2 μ m. Additionally, we wish to have good coverage of the area to ensure high enough signal intensity so we will use interdigitated electrodes. And finally, we need to have a range of values of L to work with that will give us good numbers on the absorption so we made a series of devices arrayed along a 500 micron stripe as seen in Figure B.2:

APPENDIX B (Continued)

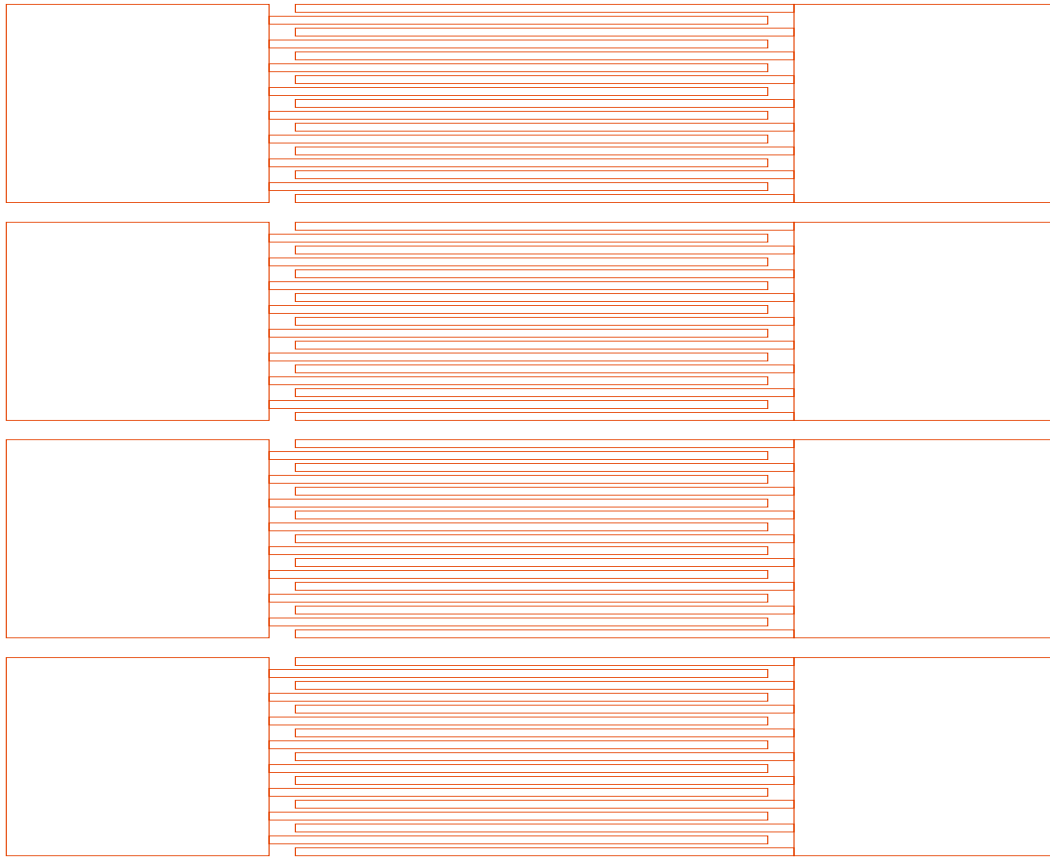


Figure B.2 MSM Design

APPENDIX B (Continued)

Once the device is fabricated you simply illuminate one end of the waveguide and measure the signal intensity on pad sets at a range of distances. Then, plot this range out and use Eq 49. Then use Eq. 48 to calculate the material gain at threshold.

B.3 Laser Diode Bars

The ultimate goal of these studies was to develop an Ultraviolet laser diode for use in a host of different applications. While there were commercial diodes available at longer wavelengths, there were no available designs for us to use. I needed to design a new set of masks for the devices I wanted to use. I opted to start with a ridged waveguide structure for the basic devices. This structure wasn't dependent on effective regrowth or ion bombardment, just highly anisotropic and smooth sidewalls to define the resonator. We wanted to have a range of resonator widths and lengths as well as we didn't have a good value on which to calculate waveguide confinement or material gain yet. I decided to start with the basic design of a ridge waveguide visible laser diode and simply modify it, using some of the techniques implemented by Wraback's group in fabricating UV LEDs. A design for a single block of diodes appears in figure B.3:

APPENDIX B (Continued)

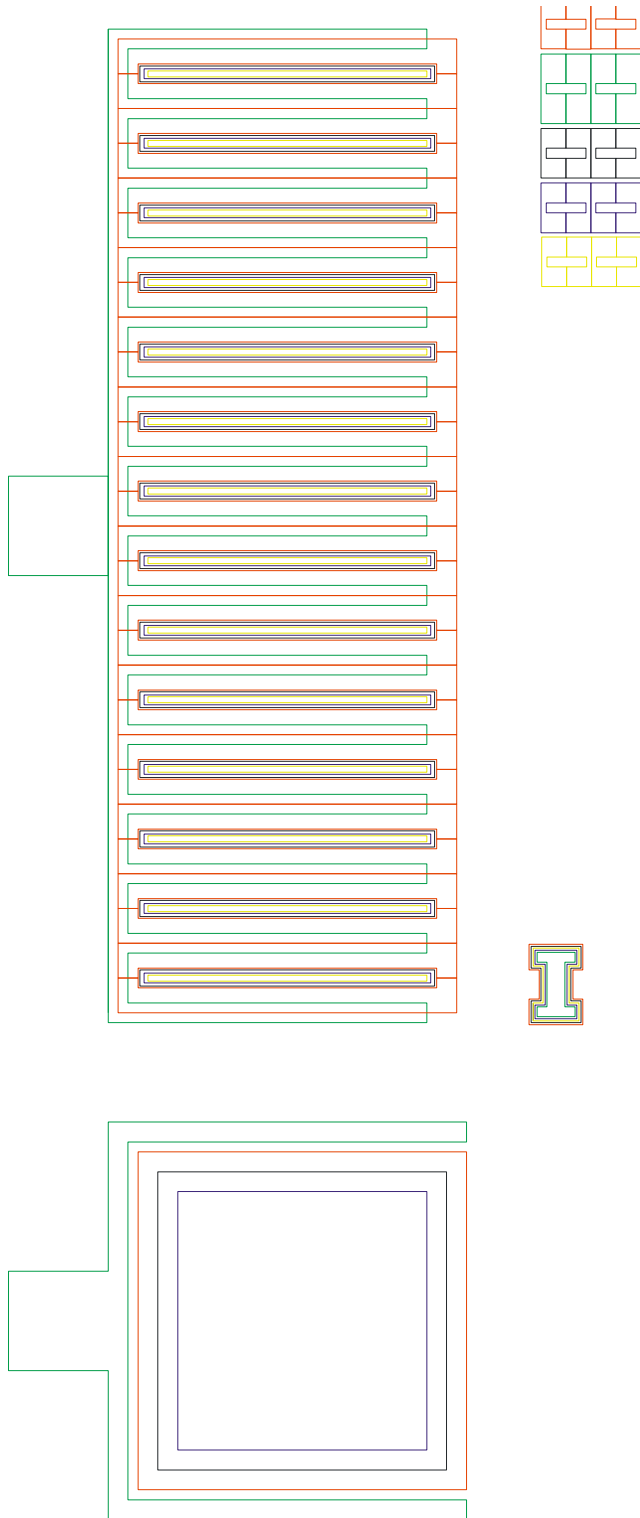


Figure C.3 Laser Diode Bars

APPENDIX B (Continued)

You can see that there is one large pad that will become a UV LED. We intend to use this as a quick test to determine the emission wavelength as the LED device will function at the same emission wavelength as the adjacent bars. Assuming you can see the colors, the layer structure is as follows:

RED- This is the mesa structure etch for the ridge waveguide on the laser bars and the LED structure. There are a variety of dimensions for this structure across the mask ranging from 10 or 20 microns wide and from 50 to 300 microns long in 50 micron steps. These mesas are etched all the way down to the substrate. share a common Anode. The layers are defined as:

GREEN- This layer is the n-metal contact. We will use a multilayer metallization composed of Ti(2nm)/Al(10nm)/Ti(400nm)/Au(200nm) to serve as a common anode for all of the devices. We will wire bond to the contact pad at the side of the device for electrical contacts.

BLACK- This is the oxide mask layer. In the ridged waveguide structure an oxide mask allows for gain guiding of the laser. This provides better confinement for the device and, while reducing the volume of gain material, typically allows for better laser performance as it keeps fewer carriers from the non-radiative recombination processes that occur near the edges of the waveguide.

YELLOW- This is the oxide via that will Provide the gain guiding contact mentioned in the black layer description. We simple use this mask to define the resist mask and use BOE to etch through the oxide down to the AlGa_N p-layer.

APPENDIX B (Continued)

BLUE- This is the metallization layer for the p-contact. We will use liftoff and a metallization of Ni(5nm)/Au(200nm) which is annealed after liftoff at 500°C. We then will then connect our test probe to the top of each of the individual bars to test.

While we can test the UV LED structures on the as processed wafer, we can't test the laser bars on the wafer. Our mask design has provided dicing spaces between the rows of devices so we can collect the light from the face of the waveguide.

APPENDIX C

Bonding Procedures and Tools

C.1 Bonding Tools

This is a drawing of the holder we developed for our laser diode bonding process. It was intended to hold 10 Au coated Cu heatsinks for deposition of the bonding material. After deposition, the diodes were then held in place with a leaf spring arm which applies pressure to ensure void free bonding. It can be seen in Figure C.1.

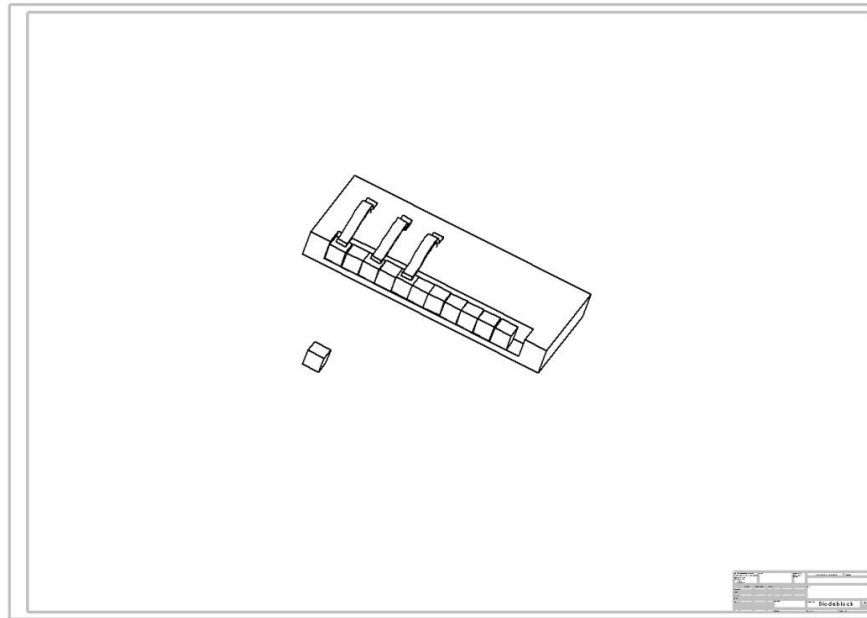


Figure C.1 Heatsink and diode holder for bonding process.

APPENDIX C (Continued)**C.2 Sloan PAK-8 Evaporator (NRC) User Instructions**

1. Check the log sheet for the previous user's comment. If OK, fill out the log sheet.
2. Turn off the ion gauge (press and hold)
3. Close the high vacuum valve, and wait for 10 secs
4. Open vent valve
5. When atmospheric pressure (~760 Torr) is reached, raise the hoist fully.
6. Close the vent valve
7. Insert/take out source and load/unload sample
8. Lower the hoist (lower until it's ~2inch below the top screw at the top of the hoist).
Adjust the hoist to align with the bottom support if necessary
9. Make sure vent valve is shut. Open the roughing valve
10. When the pressure reaches 100 ~ 150 mTorr, close the roughing valve
11. Open the high-vacuum valve
12. Check Crystal lifetime by pressing XL in crystal monitor controller. Make sure the parameters (DE, ZF, TF) are correct for aluminum (press the PRGM button first on the large controller on the right, and use ENT or ↑ and numeric pads to enter values.
When all the parameters are set, press PRGM button once more) (Parameters for AL:
DE: 2.7, ZF: 1.07, TF: 100)
13. Wait for 5 mins, and turn on the ion gauge ONCE. If it turns off automatically, then leave it high-vacuum for 5 more mins before turning the ion gauge on again
14. Wait until the desired pressure is reached (below 10^{-6} Torr is best, but depends on chamber condition).

APPENDIX C (Continued)

15. Turn on degas on the ion gauge for 5 – 10 mins before evaporation. Turn the ion gauge back on and log the pressure and pump down times.
16. Re-zero the thickness by pressing ZERO button
17. For thermal evaporation, make sure the current adjust knob is at 0 (a large knob on the lower corner of the evaporator right next to Amp-meter)
18. Turn on EVAP SUPPLY
19. Open the shutter and slowly increase the current for evaporation. The evaporation rate and thickness will be displayed on the controller (units in Angstrom)
20. Evaporate desired amount of Aluminum
21. Close the source shutter, set the current knob at 0, and turn off EVAP SUPPLY.
22. Wait 10 min to let the source to cool down (unless you deposit less than 100A)
Repeat #2 – #11
23. Check Crystal lifetime by pressing XL in crystal monitor controller. Complete the log sheet

C.3 Instruction for the Thermal Evaporator (Edwards Auto 306)

I. Quick Start.

1. Mount samples onto the sample holder plate.
2. *Vent* the chamber.
3. Open the top lid, remove the glass bell jar and the safety guard. Clean out vacuum grease with IPA moistened wipes. Clean out a small window on the bell jar with

APPENDIX C (Continued)

IPA, apply Bell Shine onto the window.

4. Mount metal holders (boat, rod, or coil) onto the four position turret and load target metals. Vacuum metal flakes and other particles off the turret and the base plate.

5. Regrease the L-gaskets. Reposition the glass bell jar onto the base plate followed by the safety guard.

6. Mount sample holder plate onto the top shaft. Close the top lid.

7. *Cycle* the system.

8. Wait for the chamber pressure to reach 8_{-10}^{-6} mBar. Add liquid nitrogen through the metal funnel.

9. Adjust z ratio and density parameters corresponding to the metal. Start sample rotation before deposition. Turn on the temperature monitor. Make sure the shutter is closed.

10. When chamber pressure reaches 2.0_{-10}^{-6} mBar, deposition can be started. Turn the main switch to LT position, slowly ramp up the current, when the target metal starts to glow brightly or melt, press the *Run* button to open the shutter and start

APPENDIX C (Continued)

11. When desired film thickness is reached, press the *Run* button again to close the shutter.
12. Turn down the electrical current then turn off the LT switch.
13. Wait for the chamber temperature to drop to 50-60 degree C.
14. Stop sample rotation.
15. *Vent* the chamber, open the top plate and remove the sample holder.
16. Remove the glass bell jar and safety guard. Clean out grease with IPA moistened wipe. Remove metal source holders. Vacuum metal flakes and other particles off the turret and the base plate.
17. Regrease the L-gaskets. Replace the glass bell jar onto the base plate followed by the safety guard. Close the lid. *Cycle* the system.
18. When chamber pressure decreases to 9.0_10⁻⁵ mBar. Press the *Seal* button.

II. Detailed Instruction.

1. Check the QCM usage and the tooling reading by pressing “*DATA*” on the upper right control panel. The ‘Usage’ reading should be less than 300, the ‘Tooling’

APPENDIX C (Continued)

reading is 1.0. Generally, the usage reading increases by 10 for every 100 nm deposition. If you are concerned that this reading might be over the limit during your deposition, contact MCF staff to replace the piezo-crystal.

2. Fix samples onto the sample holder plate using screws and washers. If your samples are lightweight you may use heat resistant double sided tape. Turn sample holder around with sample facing down and shake it over the table to check if samples have been securely fastened.

3. Press “*VENT*” on the lower right control panel to bring the chamber to atmospheric pressure. Wait two (2) minutes to complete venting. The displayed chamber pressure should be 1_103 mBar.

4. Slowly lift the chamber top lid and lock it in place with the safety pin.

5. Use an IPA moistened wipe to remove vacuum grease from the top L-gasket and the top lid.

6. Remove the plastic safety guard. Remove the glass bell jar and invert it, then put it on the work bench. Use IPA moistened wipes to remove vacuum grease from the other L-gasket and the base plate.

APPENDIX C (Continued)

7. Make two clear vertical windows on the inside of the glass bell jar with IPA moistened wipe. Spray a little polymer solution (Bell Shine) onto a wipe and coat the clear windows with the polymer. Coat the window for a second or a third time if necessary. Blow the polymer solution dry with air gun. The Bell Shine solution is stored in the fire cabinet under the bench for the spin coater.
8. Change your gloves before working with samples and evaporation sources.
9. Install metal source boat or rod on the four position turret. For chromium use the plated rod. For other metals use tungsten boat. Make sure the sources have good electric contact with the electric post on the turret. Tighten the nuts by hand. Load metals into tungsten boats. Rotate the turret slowly and make sure metal pieces do not fall out of the boat during rotation. Rotate the turret to place the desired metal source directly under the shutter. Make sure the brush connecting to the live electrode have good electric contact with the copper post holding the boat.
10. Press the “*remote*” shutter control button at the lower left control panel. Press “*Run*” at the upper right control panel a few times to make sure the shutter works properly. Press “*Run*” again to close the shutter.

APPENDIX C (Continued)

11. Vacuum all metallic flakes and residues off the source turret and the base plate, especially around the high vacuum valve (the round plate at the bottom of the evaporator).
12. Check the thermal couple, make sure it is securely connected to the connector.
13. Regrease the bottom L-gasket. Place the glass bell jar back onto the base plate.
14. Place the plastic safety guard back onto the base plate.
15. Apply vacuum grease to the top L-gasket.
16. With new glove, mount sample holder onto the chamber top shaft and fasten it with the fixing screw. Gently pull the sample holder out with hands to make sure the holder is secured to the shaft.
17. Pull out the safety pin and slowly lower the top lid to the glass chamber. Make sure it fits properly.
18. Press "*CYCLE*" to begin evacuating the chamber. The high vacuum valve will open automatically after 3-5 minutes. If pressure decreases more slowly than expected, check the L-gasket and make sure the top lid is well positioned and sealed.

APPENDIX C (Continued)

19. Press “*DATA*” to scroll between deposition parameters. Set “density” and “z” values of the metal using arrow buttons. Continue to press “*Data*” until the screen displays ‘rate reading’.
20. Wait for the chamber pressure to reach 8_{-10}^{-6} mBar, which will take about one hour. Then add liquid nitrogen through the metal funnel until liquid nitrogen overflows. Once chamber pressure drops to 2.0_{-10}^{-6} mBar, you may start deposition.
21. Make sure the shutter is in closed position and the shutter source control is in remote mode.
22. Press both “*Start*” buttons (on the upper left corner of the panel) to start sample holder rotation.
23. Turn on chamber temperature display by pressing the left button under the temperature controller.
24. Switch the current selector to LT (the green LED should light up). Increase the current very slowly and check the chamber pressure reading from time to time to

APPENDIX C (Continued)

make sure it does not increase too fast. **When the metal boat or rod starts to turn red, put on protective welding goggles.**

25. When the metal source glows brightly and the metal piece melts, press “*Run*” to open the shutter and start deposition.

26. The chamber pressure at which metal starts to melt is usually below $1.0 \cdot 10^{-5}$ mBar. The chamber pressure during metal deposition is usually below $2.0 \cdot 10^{-5}$ mBar. If the pressure goes beyond $2.0 \cdot 10^{-5}$ mBar, turn down the current and wait for the pressure to drop before resume deposition.

27. Increase or decrease the current to adjust the deposition rate. Deposition rate of 0.02-0.20 nm/sec is recommended for better film quality and film to substrate adhesion. A deposition rate of 0.4-0.5 nm/sec can be used if relatively thick film is desired or the substrate is heat sensitive.

28. Wait for the desired film thickness to be reached. Press “*Run*” again to close the shutter, then turn off source current and switch the current selector to ‘OFF’ position. If the chamber temperature exceeds 120 degree C during deposition, stop deposition by switching off the source current and let the chamber cool down

APPENDIX C (Continued)

to 50 degree then resume deposition.

29. Wait for the chamber temperature to drop to 50-60 degree C.

30. Stop sample rotation.

31. “*Vent*” the chamber and wait for two minutes.

32. Open the top plate and lock it in with the safety pin. Remove the sample holder.

Clean out grease on the L-gasket and the top plate with IPA moistened wipes

33. Remove the safety guard. Remove the glass bell jar, invert it and put it on the

work bench. Remove vacuum grease from the L-gasket and the base plate with

IPA. Remove metal source holders (boat, rod, etc.). Vacuum metal flakes and

other particles off the turret and the base plate.

34. Regrease the L-gaskets. Replace the glass bell jar onto the base plate followed by

the safety guard. Seal the glass chamber with the top plate. “*Cycle*” the system.

35. Make sure chamber pressure decrease to 9_10-5 mBar in 5 min.

36. Press “*Seal*”.

Metal source parameters

APPENDIX C (Continued)

Metal Source Density (g/cm³) Z-ratio Current /100 Amp

Gold 19.32 23.17 5-6

Silver 10.49 16.68 4-5

Copper 8.92 20.20 4-5

Aluminum 2.70 8.17 3-4

Chromium 7.20 28.94 3-4

III. Useful Instrument Specs.

1. Maximum operating temperatures.

Glass Chamber 400 °C

L -Gasket **180** °C

Implosion Guard 40 °C

2. Maximum electrical current output: 63 Ampere. (6.3 on the current meter.)

CITED LITERATURE

- [1] S. Nakamura, T. Mukai, M. Senoh,: High-power GaN P-N junction blue-light-emitting diodes, J. J. of App. Phys., Vol. 30 No. 12A, pp. L1998-L2001 (1991).
- [2] R. Dingle, D. D. Sell, S.E. Stokowski, M. Ilegems, Absorption, Reflectance, and Luminescence of GaN Epitaxial Layers Phys. Rev. B, Vol. 4, pp. 1411 (1971).
- [3] H. Harima: Characterization of GaN and related nitrides by raman scattering. In: III-Nitride Semiconductors Optical Properties I, eds. M.O. Manasreh, H.X Jiang, pp. 283-331, New York, Taylor and Francis, 2002.
- [4] C. Kittel, Introduction to Solid State Physics, New York, John Wiley and Sons, 1996.
- [5] J.A. Reissland, Physics of Phonons, New York, John Wiley and Sons, 1973.
- [6] G. Nilsson and G. Nelin: Study of the Homology between Silicon and Germanium by Thermal-Neutron Spectrometry Phys. Rev. B, Vol. 6: 3777-3381,1972.
- [7] T. R Hart, R.L. Aggarwal and B. Lax: Temperature Dependence of Raman Scattering in Silicon: Phys. Rev. B, Vol. 1, pg. 638-642, 1970.
- [8] R. Loudon: The Raman Effect in Crystals, Adv. Phys., Vol. 13, pp. 423-482,1964.
- [9] L. Bergman, M. Dutta, C. Balkas, R.F. Davis, J.A. Christman, D. Alexson and R.J. Nemanitch: Raman Analysis of the E1 and A1 Quasi-LO and -TO Modes in Wurtzite AlN. J. Appl.Phys. 85:3535,1999.
- [10] D. Alexson, L. Bergman, M. Dutta, K.W. Kim, S. Komirenko, R. Nemanich, B.C. Lee, M. Strosio, S. Yu: Confined Phonons and Phonon-mode properties of III-V Nitrides with wurtzite crystal structure, Physica B, 263, 510-513, 1999.
- [11] Herzberg, G.: Infra-red and Raman Spectra of Polyatomic Molecules, New York, Van Nostrand, 1954.
- [12] Wilson, E. B., Decius, J. C., and Cross, P. C.: Molecular Vibrations, New York, McGraw-Hill, 1955.
- [13] Richter, W., Springer Tracts in Modern Physics78, New York, Springer, 1976.

CITED LITERATURE (Continued)

- [14] D. Alexson: Device Implications of Phonons in III-V Nitride Bulk and Dimensionally Confined Semiconductors. PhD Thesis, University of Illinois at Chicago, 2006.
- [15] M. Schwöerer-Bohning, A.T. Macrander, M. Pabst, P. Pavone: Phonons in wurtzite aluminum nitride, Phys. Stat. Sol. B 215, 177-180, 1999.
- [16] I. Adesida, A. Mahajan, E. Andideh, M. A. Khan, D.T. Olsen, J. N. Kuznia: Reactive ion etching of gallium nitride in silicon tetrachloride plasmas, Appl. Phys. Lett., Vol. 63, pp. 2777-2779, 1993.
- [17] J.I. Pankove, Electrolytic etching of GaN, Journal of the Electrochemical Society, Vol. 119, pp. 1118-1119, 1972.
- [18] A. Ping, I. Adesida, M.A. Khan, J.N. Kuznia, Reactive ion etching of gallium nitride using hydrogen bromide plasmas, Electronics Letters, Vol. 30, pp. 1895-1897, 1994.
- [20] K. Suzuki, N. Itabashi: Future prospects for dry etching, Pure and Applied Chemistry, Vol. 68, No. 5, pp. 1011-1015, 1996.
- [21] J.W. Coburn, H.F. Winters: Ion and electron-assisted gas-surface chemistry- an important effect. J. Appl. Phys., Vol. 50, pp. 3189-3195, 1979.
- [22] D. L. Flamm, V. Donnelley, D. Ibbotson: Basic Chemistry and mechanisms of plasma etching. Journal of Vacuum Science Technology B, Vol. 1, pp. 23-30, 1983.
- [23] K. Suzuki, Radio frequency based microwave plasma etching technique: a method to increase SiO₂ etch rate. Journal of Vacuum Science Technology B, Vol. 3, pp. 1025-1934, 1985.
- [24] S. Pearton, J. Zolper, R. Shul, F. Ren: GaN: Processing, defects and devices: J. Appl. Phys., Vol. 86, pp. 1-77, 1999.
- [25] I. Adesida, A. Mahajan, E. Andideh, M. A. Khan, D.T. Olsen, J. N. Kuznia: Reactive ion etching of gallium nitride in silicon tetrachloride plasmas, Appl. Phys. Lett., Vol. 63, pp. 2777-2779, 1993.
- [26] V. Kuryatkov, B. Borisov, J. Saxena, S. Nikishin, H. Temkin, S. Patibandla, L. Menon, M. Holtz: Analysis of nonselective plasma etching of AlGa_N by CF₄/Ar/Cl₂: J. Appl. Phys. Vol. 97, pg. 073302, 2005.

CITED LITERATURE (Continued)

- [27] R.T. Green, I.J. Luxmoore, P.A. Houston, F. Ranalli, T. Wang, P.J. Parbrook, M.J. Uren, D.J. Wallis, T. Martin: Comparison of damage introduced into GaN/AlGa_n/GaN heterostructures using selective dry etch recipes: Semiconductor Science and Technology Vol. 24, 075020, 2009.
- [28] S.A. Smith, C. Wolden, M. Bremser, A. Hansen, R.F. Davis: high rate and selective etching of GaN, AlGa_n and AlN using an inductively coupled plasma: Appl. Phys. Lett., Vol. 71, pp. 3631-3633, 1997.
- [29] D. Buttari, A. Chini, T. Palacios, R. Coffee, L. Shen, H. Xing, S. Heikman, L. McCarthy, A. Chakraborty, S. Keller, U.K. Mishra: Appl. Phys. Lett., Vol. 83, pp. 4779-4781, 2003.
- [30] S. Salimian, C. Cooper, R. Norton, J. Bacon: Reactive ion etch process with highly controllable GaAs to AlGaAs selectivity using SF₈ and SiCl₄: Appl. Phys. Lett., 5, 1 pp. 1083 (1987).
- [31] L. Chen, H. Yimin, J. Chen, Y. Sun, L. T. Li, D. Zhao, H. Gong: International Symposium on Photoelectric Detection and Imaging 2007: Proceedings of SPIE, Vol. 6621, pg. 66211A, 2008.
- [32] R. Li, T. Dai, L. Zhu, H. Pan, K. Xu, B. Zhang, Z. Yang, G. Zhang, Z. Gan, X. Hu: the reactive ion etching characteristics of AlGa_n/GaN SLs and etch-induced damage study of n-GaN using Cl₂/SiCl₄/Ar plasma: Journal of Crystal Growth, Vol. 298, pp. 375-378, 2007.
- [33] W. S. Lau, B.P. Singh, Joy B.H. Tan, S. Gunwan, Y.Y. Jiang, R. Wynn, V. Lim, A.D. Trigg: dry etching of Al_xGa_{1-x}N/GaN by CCl₂F₂ chemistry for device isolation: Phys. Stat. Solid. C, No. 7, pp. 2544-2547, 2005.
- [34] L. Sun, J. Chen, J. Li, H. Jiang: AlGa_n solar-blind avalanche photodiodes with high multiplication gain: Appl. Phys. Lett., Vol. 97, 191103, 2010.
- [35] S. C. Hung, C.W. Chen, C.Y. Shieh, G.C. Chi, R. Fan, S.J. Pearton: High sensitivity carbon monoxide sensors made by zinc oxide modified gate GaN/AlGa_n high electron mobility transistors under room temperature. Appl. Phys. Lett., Vol. 98, 223504, 2011.
- [36] M-H Lo, Y.J. Cheng, H.C. Kuo, S.C. Wang: Enhanced electron-hole plasma stimulated emission in optically pumped gallium nitride nanopillars: Appl. Phys. Lett., Vol. 98, pg. 121101, 2011.

CITED LITERATURE (Continued)

- [37] N. Zainal, S.V. Novikov, C. J. Mellor, C.T. Foxon, A.J. Kent: Current-voltage characteristics of zinc-blende (cubic) $\text{Al}_{0.3}\text{Ga}_{0.7}\text{N}/\text{GaN}$ double barrier resonant tunneling diodes: Appl. Phys. Lett., Vol. 97, 112102, 2010.
- [38] W. Park, K. Whang, Y.G. Yoon, J. H. Kim, S. Rha, C.S. Hwang: High rate dry etching of InGaZnO by BCL_3/O_2 plasma: Applied Physics Letters, Vol. 99, pg. 062110, 2011.
- [39] J. S. Cabalu, A. Bhattacharyya, C. Tomidis, I. Friel, T. D. Moustakas: High power ultraviolet light emitting diodes based on GaN/AlGaIn quantum wells produced by molecular beam epitaxy: J. Appl. Phys., Vol. 100, 104506, 2006.
- [40] Evgeny Zhirnov, S. Stepanov, A. Gott, W.N. Wang, Y.G. Shreter, D.V. Tarkin, N.I. Bochkareva: ICP etching of III-nitride based laser structure with $\text{Cl}_2\text{-Ar}$ plasma assisted by Si coverplate material: Journal of Vacuum Science Technology A, Vol. 23(4), pp. 687-692 2005.
- [41] S.D. Roh, R.B. Swint, A.M Jones, T.S. Yeoh, A.E. Huber, J.S. Hughes, J.J. Coleman: Dual-wavelength asymmetric cladding InGaAs-GaAs ridge waveguide distributed Bragg reflector lasers: Photonics Technology Letters, Vol. 11, pp. 15-17, 1999.
- [42] R.M. Lammert, S.D. Roh, J.S. Hughes, M.L. Osowski, J.J. Coleman: MQW DBR lasers with monolithically integrated external-cavity electroabsorption modulators fabricated without modification of the active region: Photonics Technology Letters, IEEE, Vol. 9, pp. 566-568, 1997.
- [43] C. Lee, C. Wang, G. Matijasevic: Advances in Bonding Technology for Electronic Packaging, Journal of Electronic Packaging, Vol. 115, pp. 201-206, 1993.
- [44] Darveaux, R. and Banerji, K.: Constitutive relations for tin-based solder joints, IEEE Transactions on Components, Hybrids, and Manufacturing Technology, Vol. 15, No. 6, pp. 1013-1024, 1992.
- [45] G. Matijasevic, C. Wang, C. Lee, Void Free Bonding of Large Silicon Dice Using Gold-Tin Alloys, IEEE Transactions on Components, Hybrids, and Manufacturing Technology, Vol. 13, No. 4, 1990.
- [46] D. Olsen, H. Berg, Properties of Die Bond Alloys Relating to Thermal Fatigue, IEEE Transactions on Components, Hybrids and Manufacturing Technology, Vol. 2, No. 2, 1979.

CITED LITERATURE (Continued)

[47] L. Gomidzelovic, D. Zivkovic, N. Talijan, D. Manasijevic, V. Cosovic, A. Grujic: Phase Equilibria Investigation and Characterization of the Au-In-Sb System, Metalurgia- Journal of Metallurgy, Vol. 13, pg. 204, 2007.

[48] K. Fujiwara, T. Fujiwara, K. Hori, M. Takusagawa: Aging characteristics of Ga_{1-x}Al_xAs double-heterostructure lasers bonded with gold eutectic alloy solder. Appl. Phys. Lett., Vol. 34, pp. 668-670, 1979.

[49] C. H. Lee, Y. M. Wong, C. Doherty, K. L. Tai, E. Lane, D. D. Bacon, F. Baiocchi, A. Katz: Study of Ni as a barrier metal in AuSn soldering applications for laser chip/submount assembly. J. Appl. Phys., Vol. 72, pp. 3808-3815, 1992.

[50] S. Timoshenko, "Analysis of bi-metal thermostats," Journal of the Optical Society of America, Vol. 11, pp. 233-250, 1925.

[51] Military Standard: Test Methods and Procedures for Microelectronics, MIL-STD-883, US Department of Defense, Washington DC 1977.

[52] C.A. Arguello, D.L. Rousseau, S.P.S. Porto: First order Raman effect in wurtzite type crystals. Phys. Rev., Vol. 181, pp. 1351-1363, 1969.

[53] T. Suski, S. Ruminov, J. Kruger, G. Conti, E.R. Weber, N.D. Bremser, R.F. Davis, C. Kuo, Proceedings of MRS, Fall meeting, Boston, 1996.

[54] F. Bechstedt, H. Grille: Lattice dynamics of ternary alloys. Physica Status Solidi B, Vol. 216, pp. 761-768, 1999.

[55] H. Grille, Ch. Schnittler, F. Bechstedt: Phonons in ternary group-III nitride alloys. Physics Review B, Vol. 61, pp. 6091-6105, 2000.

[56] A. Cros, H. Angerer, R. Handschuh, O. Ambacher, M. Stutzman: Raman study of the optical phonons in Al_xGa_{1-x}N alloys, Solid State Communications, Vol. 104, pg. 35-39, 1997.

[57] A.V. Sampath, G.A. Garrett, C.J. Collins, W.L. Sarney, E.D. Readinger, P.G. Newman, H. Shen, M. Wraback: Growth of AlGa_N alloys exhibiting enhanced luminescence efficiency. Journal of Electronic Materials, Vol. 35, No. 4, pg. 641, 2006.

[58] A.V. Sampath, M.L. Reed, G.A. Garrett, E.D. Readinger, H. Shen, M. Wraback, C. Chua, N. Johnson, A. Usikov, O. Kovalenkov, L. Shapovalova, V. Dmitriev: Double heterostructure ultraviolet light emitting diodes with nanometer scale compositionally inhomogeneous active regions. Phys. Stat. Solid. C, Vol. 5, pg. 2303-2305, 2008.

CITED LITERATURE (Continued)

- [59] C.J. Collins, A.V. Sampath, G.A. Garrett, W.L. Sarney, H. Shen, M. Wraback, A.Yu. Nikiforov, G.S. Cargill III, V. Dierolf: Enhanced room-temperature luminescence efficiency through carrier localization in $\text{Al}_x\text{Ga}_{1-x}\text{N}$ alloys. Appl. Phys. Lett., Vol. 86, pg. 031916, 2005.
- [60] A. Smekel, Quantum dispersion, *Naturwissenschaften*, Vol. 11, pg. 873, 1923.
- [61] C.V. Raman: A new radiation. Indian Journal of Physics, Vol. 2, pg. 387, 1928.
- [62] G. Coli, K.K. Bajaj, J. Li, J.Y. Lin, H.X. Jiang: Linewidths of excitonic resonance, Appl. Phys. Lett., Vol. 78 pg. 1829, 2001.
- [63] V. Yu Davydov, I.N. Goncharuk, A.N. Smirnov, A.E. Nikolaev, W.V. Lundin, A. S. Usikov, A.A. Klochikin, J. Aderhold, J. Graul, O. Seminchova, H. Harima: Composition dependence of optical phonon energies and Raman line broadening in hexagonal $\text{Al}_x\text{Ga}_{1-x}\text{N}$ alloys, Phys. Rev. B, Vol. 65, pg. 125203 (2002).
- [64] K. Vedam: Spectroscopic ellipsometry: a historical overview: Thin Solid Films, Vol. 313, pp. 1-9, 1998.
- [65] D.E. Aspnes: Characterization of Materials, Thin Films and Interfaces by Optical Reflectance and Ellipsometric Techniques. Journal of Physics Colloquium. C10, 1983.
- [66] E.D. Palik (Editor), Handbook of Optical Constants Vol. 1 and 2, Academic Press, New York, 1991.
- [67] J.A. Woollam, B. Johs, C. Herzinger, J. Hilfiker, R. Synowicki, C. Bungay, Critical Reviews of Optical Science and Technology, Vol. CR72, Denver, 2000.
- [68] W.H. Press, B.P. Flannery, S.A. Teukolosky, W.T. Vettering, Numerical Recipes in C, Cambridge University Press, Cambridge, 1988.
- [69] U. Tisch, B. Meyler, O. Katz, E. Finkman, J. Salzman: Dependence of the refractive index of $\text{Al}_x\text{Ga}_{1-x}\text{N}$ on temperature and composition at elevated temperatures, Journal of Applied Physics, Vol. 89, No. 5, pp. 2676-2685, 2001.

CITED LITERATURE (Continued)

- [70] D. Brunner, H. Angerer, E. Bustarret, F. Freudenberg, R. Höppler, R. Dmitrov, O. Ambacher, M. Stutzman: Optical constants of epitaxial AlGa_xN films and their temperature dependence, Journal of Applied Physics, Vol. 82, no. 10, pg. 5090-5096, 1997.
- [71] "Quickstart Modeling," Applications Note, Horiba- Jobin Yvon, France, 2010.
- [72] M.H. Lee, K.J. Kim, E. Oh: Ellipsometric investigation of optical constant and band gap of Ga_{1-x}In_xN/GaN ($x \leq 0.12$) heterostructures. Solid State Communications, Vol. 114, pg. 325-328, 2000.
- [73] Collins, A.T, Lightowers, E.C., Dean, P.J.: Lattice vibration spectra of Aluminum Nitride. Phys. Rev., Vol. 158, No. 3, pp. 833-838, 1967.
- [74] Goldberg Yu. In: Properties of Advanced Semiconductor Materials GaN, AlN, InN, BN, SiC, SiGe. Eds. Levinstein M.E., Rumyantsev S.L., Shur M.S., John Wiley & Sons, Inc., New York, 2001, 31-47.
- [75] P.D. Paulson, X. Matthew: Spectroscopic ellipsometry investigation of optical and interface properties of CdTe films deposited on metal foils: Solar Energy Materials & Solar Cells, Vol. 82, Issue 1-2, pp. 279-290, 2004.
- [76] J. N. Hilfiker, C. Bungay, R. Synowicki, T. Tiwald, C. Herzinger, B. Johs, G. Pribil, J.A. Woollam: Progress in spectroscopic ellipsometry: applications from vacuum ultraviolet to infrared. Journal of Vacuum Science Technology A, Vol. 21, Iss. 4, pg. 1103-1108, 2003.
- [77] M.J. Bergman, U. Ozgur, H.C. Casey, H.O. Everitt, J.F. Muth: ordinary and extraordinary refractive indices for Al_xGa_{1-x}N epitaxial layers, App. Phys. Let., Vol. 75, No. 1, pg. 67-69, 1999.
- [78] N.A. Sanford, L.H. Robbins, A.V. Davydov, A. Shapiro, D. Tsvetkov, V. Dmitriev, S. Keler, U.K. Mishra, S.P. DenBaars: Refractive index study of Al_xGa_{1-x}N films grown on sapphire substrates, J. Appl. Phys., Vol. 94, No. 5, pg. 2980-2991, 2003.
- [79] M. Dutta and M. A. Stroschio, Quantum-Based Electronic Devices and Systems. World Scientific Publishing Company, 1998.
- [80] V. Mitin, V. Kochelap and M. A. Stroschio, Quantum Heterostructures: Microelectronics and Optoelectronics, Cambridge, Cambridge University Press, 1999.

CITED LITERATURE (Continued)

- [81] M. Dutta and M. A. Stroschio, Advances in Semiconductor Lasers and Application to Optoelectronics, World Scientific Publishing Company, 2000.
- [82] S. M. Komirenko, K. W. Kim, M. A. Stroschio and M. Dutta: Energy-dependent electron scattering via interaction with optical phonons in wurtzite crystals and quantum wells, Phys. Rev. B, vol. 61, pp. 2034-2040, 2000.
- [83] L. Bergman, M. Dutta, K. W. Kim, P. G. Klemens, S. M. Komirenko and M. A. Stroschio, Phonons, electron-phonon interactions, and phonon-phonon interactions in III-V nitrides, Ultrafast Phenomena in Semiconductors IV, Proceedings of SPIE, vol. 3940, pp. 100, 2000.
- [84] J. Gleize, M. A. Renucci, J. Frandon and F. Demangeot: Anisotropy effects on polar optical phonons in wurtzite GaN/AlN superlattices, Phys. Rev. B, vol. 60, pp. 15985-15992, 1999.
- [85] G.H.B. Thompson, Physics of Semiconductor Devices, Chichester, Wiley, 1980.
- [86] K.L. Shaklee, R.F. Leheny: Direct determination of optical gain in semiconductor crystals, Appl. Phys. Lett. Vol. 18, pg. 475, 1971.
- [87] F. Binet, J.Y. Duboz, N. Laurent, C. Bonnat, P. Collot, F. Hanauer, O. Briot, B. Gil, F. Scholz, J. Off, A. Sohmer: Optical pumping in nitride cavities with etched mirror facets, Materials Science and Engineering B, Vol. 50, pp. 183-187, 1997.
- [88] J.Y. Duboz, F. Binet, D. Dolfi, N. Laurent, F. Scholz, J. Off, A. Sohmer, O. Briot, B. Gil: Diffusion length of photoexcited carriers in GaN: Materials Science and Engineering B: Vol. 50, pp. 289-295, 1997.

VITA

RYAN RICHARD AHERN

EDUCATION

B.S. PHYSICS, University of Illinois at Urbana-Champaign, 1998.

M.S. Electrical and Computer Engineering, University of Illinois at Chicago, 2008.

Ph.D. Electrical and Computer Engineering, University of Illinois at Chicago, 2011.

WORK EXPERIENCE

US Army, Special Forces Operator, 1990-Present. Conduct operations in support of global war on terror.

Guest Graduate- Argonne National Laboratory, Aug 2010- Aug. 2011.

Conducted a number of experiments to include:

- Utilization of compressive imaging to increase acquisition time in a passive millimeter wave system.
- Utilization of millimeter wave system to detect nuclear radiation.
- BWO radiation detection of *bacillus subtilis* for use as a detection method for *bacillus anthracis*.
- ZnO nanowire detection of nuclear radiation.

Graduate Researcher- University of Illinois/ Army Research Lab 2005-Present.

Conducted a number of experiments to include:

- Processing of AlGaIn materials for laser diode fabrication.
- Characterization of AlGaIn NCI materials.
- Evaluated technologies for USSOCOM.

Staff Engineer- Videojet Technologies Inc. 2000-Present

Design and test new technologies for use in laser marking systems.